Department of Civil and Environmental Engineering
UNIVERSITY OF WISCONSIN–MADISON

5 November 2023

Civil Engineering
Purdue University
West Lafayette, IN

Re: Tenure-Track Faculty Positions in the Lyles School of Civil Engineering

To Whom It May Concern,

I am pleased to apply to the associate professor position in Structural Engineering. I am currently a 6th year assistant professor in Structural Engineering at UW-Madison with a focus on steel structures. My research experience includes infrastructure resilience, data-driven design methods, physical experiments, and computational modeling. Details on my research areas and teaching philosophy are presented in the included statements. Details on my service commitments are presented in the included CV. More details on my funded research projects and education initiatives are available on my website https://ssirl.cee.wisc.edu/. Please feel free to contact me with any questions.

Sincerely,

Hannah Blum
Email: hannah.blum@wisc.edu

Hannah Blum

Assistant Professor and Alain H. Peyrot Fellow in Structural Engineering
Department of Civil and Environmental Engineering
University of Wisconsin-Madison
hannah.blum@wisc.edu

Professional Preparation

University of Sydney	Civil Engineering	Ph.D., Jan 2017
Johns Hopkins University	Civil Engineering	M.S.E., Dec 2012
Johns Hopkins University	Civil Engineering	B.S., Dec 2010

Appointments

University of Wisconsin-Madison, WI, USA
Aug 2018 – present — Assistant Professor, Dept. Civil & Environmental Engineering

University of Sydney, NSW, Australia
Sep 2016 – Dec 2017 — Associate Lecturer, School of Civil Engineering

Professional Licenses, Affiliations, and Service

Professional Memberships

American Society of Civil Engineers (ASCE)	2009 –
American Institute of Steel Construction (AISC)	2011 –
Structural Stability Research Council (SSRC)	2012, 2015 –
Cold-Formed Steel Research Consortium (CFSRC) – Affiliated Investigator	2018 –
Cold-Formed Steel Engineers Institute (CFSEI)	2019 –
Australian Steel Institute (ASI)	2013 – 2018

Voting Committee Membership

AISC Technology Integration Committee	2022 –
AISC Committee on Structural Stainless Steel	2018 –
AISI Committee on Standards and Education Committee	2019 –
Subcommittee 22 – Stability and Combined Actions [Vice-Chair]	2023 –
ASCE/SEI Standards Committee *Stainless Steel Cold-Formed Sections Standards*	2019 –
SSRC Task Group 03: Stability of Steel Systems [Vice-Chair]	2021 –
SSRC Task Group 05: Thin-Walled Structures [Vice-Chair]	2017 – 2021

UW-Madison Service

Faculty Advisor, AISC Student Steel Bridge Club	2019 –
Women in Science and Engineering (WISE) dinner mentor	2019 –
CEE Senior Capstone Judge	2022 –
CEE alternate senator for the Faculty Senate	2019 – 2022

Journal Reviewer

Journal of Constructional Steel Research	2016 –
Structures	2018 –
Journal of Structural Engineering	2018 –
Thin-Walled Structures	2019 –
Engineering Structures	2020 –
Architecture, Structures and Construction	2021

Awards

Alain H. Peyrot Fellowship (2018 – present)	UW-Madison
Harvey Spangler Award for Innovative Teaching (2023)	College of Engineering, UW-Madison
Terry Peshia Early Career Faculty Award (2023)	American Institute of Steel Construction
McGuire Award for Junior Researchers – MAJR Medal (2022)	Structural Stability Research Council
Yoon Duk Kim Young Researcher Award (2021)	Structural Stability Research Council
Yoon Duk Kim Young Researcher Award Hon. Mention (2020)	Structural Stability Research Council
ASCE Exceed Fellow (2019)	American Society of Civil Engineers

Advancing Structural Steel Education Award (2018)	American Institute of Steel Construction
Vinnakota Award (2016)	Structural Stability Research Council
Wei-Wen Yu Student Scholar Award (2016)	Wei-Wen Yu Center for CFS Structures
William R. Kahl Scholarship Award (2010)	ACEC/MD

Research Interests

Steel, Cold-Formed Steel, Stainless-Steel Structures	Structural Stability and Reliability
Data-Driven Structural Design	Virtual and Augmented Reality
Finite Element Modeling & Experimental Methods	Historic Structures

Teaching

University of Wisconsin-Madison

Steel Structures 1 (2021 –); undergraduate course in the design and analysis of steel structures
Steel Structures 2 (2019 –): combined upper level undergraduate and graduate level course
Structures Seminar (2021, 2023): graduate seminar in the structural engineering focus area
Structural Reliability (2020): small graduate level course covering uncertainty in structural design

University of Sydney

Structural Mechanics (2017): undergraduate core course
Steel Structures 1 (2017): undergraduate core course in design and analysis of steel structures

Research Advisor

Postdoctoral Scholars:

2023 – current, Dr. Koh, UW-Madison, Various projects funded by the Steel Deck Institute

PhD Candidates:

2023 – current, Kim, UW-Madison, WN-Series Joist System Reliability
2023 – current, Wang, UW-Madison, Metal Buildings Subjected to Tornadoes
2022 – current, Cicek, UW-Madison, Steel Joist and Deck System Reliability
2018 – 2022, Koh, UW-Madison, Augmenting Steel Design with Data-Driven and Adv. Analysis Approaches
2019 – 2022, Sippel, UW-Madison, Structural Analysis with Non-Symmetric Cross Sections
2018 – 2022, Xia, UW-Madison, Analytical and Computation Modeling of Temperature Dependent Material Properties, Residual Stress, and Torsional Behavior for Cold-Formed Steel Members

Master (Research):

2023 – current, Mustaq, UW-Madison, ⅞ inch Studs Welded Through Steel Deck: Full Beam
2023 – current, Dutta, UW-Madison, Point Cloud Analysis of Historic Structures
2023 – current, Mehendale, UW-Madison, Augmented Reality in Structural Steel Applications
2022 – current, Alshammari, UW-Madison, Steel Joist and Deck System Reliability
2020 – 2022, Laracuente, UW-Madison, Behavior of Concentrically Loaded Austenitic Stainless-Steel Unequal-Leg Angles
2017, Univ. of Sydney, Parametric Study of Conn. Stiffness of Cold-Formed Steel Portal Frames

Undergraduate:

Fall 2023, UW-Madison, 1 student, Point-cloud analysis; 1 student, Vacuum box testing
Spring 2023, UW-Madison, 1 student, Steel joist system reliability; 3 students, Vacuum box development
Spring 2022, UW-Madison, 2 students, Stainless-steel compression members
Fall 2021, UW-Madison, 1 student, Augmented reality in steel fabrication; 1 student, Residual stress testing; 1 student, Stainless-steel compression members
Spring 2021, UW-Madison, 2 students, Pilot Study – Augmented reality in steel fabrication
2019-2020, UW-Madison, 1 student, Low temp properties of cold-formed steel
2018-2019, UW-Madison, 2-3 students, Virtual reality for steel structures education
2017 Honours Thesis, Univ. of Sydney, 2 students, Experimental Investigation of Apex Connection Stiffness in Cold-Formed Steel Portal Frames

Grants received

Department of Defense – Engineering Research and Development Center
$3,443,495 (50%), Monitoring, Modeling, and Visualization of Historic Structures

National Science Foundation
- $212,344, 2021-2024, Collaborative Research: Assessment of Building Resiliency in Tornadoes Considering Transient Internal Pressure Effects, Award #2053364

Steel Founders' Society of America (SFSA) (Prime: Department of Defense)
- $300,000, 2023-2025, Augmented Reality Implementation into Steel Foundry Applications

American Institute of Steel Construction
- $104,265, 2021-2023, Augmented Reality Technology in Structural Steel Fabrication
- $150,000, 2024-2026, Unequal Leg Stainless Steel Angles Under Compression

Steel Joist Institute
- $90,000, Jan 2024 – Dec 2024, Design of Shear Connectors Welded Through Steel Deck: Full Beam Testing to Validate ⅞ inch Studs
- $70,000, Nov 2023 – Oct 2024, Joist Bay system reliability
- $20,000, Sep 2022 – May 2023, Steel joist system reliability
- $7,000, Jan-Dec 2022, Modified slenderness ratio of joist chord members
- $23,153, Jan-Aug 2021, Analytical Study: Flexural-Torsional Buckling of Joist Chord Members

Steel Deck Institute
- $25,000, May-Dec 2023, System Reliability of Steel Roof Deck
- $24,350, Jan-Jun 2023, Design of Shear Connectors Welded Through Steel Deck: A Reanalysis of Existing Data
- $27,000, Jan-Sep 2023, Develop and Construct Prototype Vacuum Box
- $8,200, May-Oct 2023, Inelastic Analysis and Design of Bare Steel Deck Diaphragms using Instantaneous Center Method

New Millennium
- $70,000, Jan-Dec 2024, WN-Series Joist System Reliability – Phase 1

American Iron and Steel Institute, Small Projects
- $6,000, Summer 2023, System Reliability of Steel Roof Deck
- $6,000, Summer 2023, Inelastic Analysis and Design of Bare Steel Deck Diaphragms using Instantaneous Center Method
- $10,000, Summer 2021, CFS Strength Prediction for Bending & Torsion
- $10,000, Summer 2020, Tutorials for Analysis of Systems with Unsymmetrical Sections Using the Latest Version of MASTAN2
- $6,000, Summer 2020, Review of Int. CFS and Other Test Standards for Implementation Into AISI

College of Engineering, University of Wisconsin-Madison, Educational Innovation
- $48,831, 2019-2020, Virtual and Mixed Reality Teaching Lab for Engineering Education

Wisconsin Alumni Research Foundation
- $50,861, 2023-2024, Architected meta-structures for resilient structural steel framing
- $44,663, 2022-2023, Experimental and numerical dataset requirements for machine learning-based structural design
- $42,833, 2021-2022, Fragility analysis of metal roof system subject to extreme wind loading
- $42,878, 2020-2021, Residual stress quantification in currently produced structural steel sections
- $39,137, 2019-2020, Eval. of current design codes for structural systems with unsymm. sections

University of Wisconsin-Madison, Office of the Provost, Educational Innovation Small Grant
- $15,000, 2019-2020, Virtual Reality in Structural Engineering Education

Publications [Google Scholar Profile]

Journal Papers

Laracuente, M.E., Sippel, E.J., and Blum, H.B., (202x). "Experimental investigation of fixed-ended hot-rolled austenitic stainless-steel unequal-leg angles under compression", *Structures* (accepted).

Ding, C., Xia, Y., Blum, H.B., Li, Z., Schafer, B.W., (202x). "Strength of bolted lap shear connections with advanced high strength steel sheets", *Journal of Structural Engineering* (accepted, in press).

Akchurin, D., Ding, C., Xia, Y., Blum, H.B., Schafer, B.W., Li, Z., (2023). "Family optimization of cold-formed steel lipped-channel sections with strength and stiffness constraints due to cross-sectional instabilities", *Thin-Walled Structures*. https://doi.org/10.1016/j.tws.2023.111118

Koh, H., Rosson, B.T., and Blum, H.B., (2023). "Stability analysis of stiffness reduction models on rotary- and non-rotary straightened W-shapes", *Journal of Constructional Steel Research*.

https://doi.org/10.1016/j.jcsr.2023.108024

Xia, Y., & Blum, H. B. (2023). "Subzero Material Properties of Advanced High-Strength Cold-Formed Steel Alloys," *Buildings*, 13(2), 399. https://www.mdpi.com/2107188

Sippel, E. J., Ziemian, R. D., & Blum, H. B. (2023). "Experimental Verification of Eccentrically Loaded Steel Joist Analysis with Nonsymmetric Sections," *Journal of Structural Engineering*, 149(5), 04023027. https://doi.org/10.1061/JSENDH.STENG-11670

Sippel, E.J., Ziemian, R.D., Blum, H.B., (2022). "Influence of torsional stiffness in double-angle open-web joist and joist girder chords," *Journal of Constructional Steel Research*. https://doi.org/10.1016/j.jcsr.2022.107595

Koh, H., and Blum, H.B., (2022). "Machine Learning-Based Sensitivity of Steel Frames with Highly Imbalanced and High-Dimensional Data," *Engineering Structures*. https://doi.org/10.1016/j.engstruct.2022.114126

Koh, H., and Blum, H.B., (2022). "A review of current practice for testing by analysis of cold-formed steel structures," *Structures*. https://doi.org/10.1016/j.istruc.2022.01.017

Xia, Y., Yan, X., Gernay, T., and Blum, H.B., (2022). "Elevated temperature and post-fire stress-strain modeling of advanced high-strength cold-formed steel alloys," *Journal of Constructional Steel Research*. https://doi.org/10.1016/j.jcsr.2021.107116

Sippel, E.J., Ziemian, R.D., Blum, H.B., (2021). "Structural analysis using line elements to model members with non-symmetric cross sections," *Thin-Walled Structures*. https://doi.org/10.1016/j.tws.2021.108407

Sippel, E.J., Blum, H.B., (2021). "Structural analysis of steel structures with non-symmetric members," *Engineering Structures*. https://doi.org/10.1016/j.engstruct.2021.112739

Chen, X., Blum, H.B., Roy, K., Pouladi, P., Uzzaman, A., and Lim, J.B.P., (2021). "Moment-resisting apex bracket of cold-formed steel portal frames: behaviour, capacity, and design," *Journal of Constructional Steel Research*, 183, 106718. https://doi.org/10.1016/j.jcsr.2021.106718

Xia, Y., Ding, C., Li, Z., Schafer, B.W., Blum, H.B., (2021). "Numerical modeling of stress-strain relationships for advanced high strength steels," *Journal of Constructional Steel Research*, 182, 106687. https://doi.org/10.1016/j.jcsr.2021.106687

Yan, X., Xia, Y., Blum, H. B., & Gernay, T. (2021). Post-fire mechanical properties of advanced high-strength cold-formed steel alloys. *Thin-Walled Structures*, 107293. https://doi.org/10.1016/j.tws.2020.107293

Yan, X., Xia, Y., Blum, H. B., & Gernay, T. (2020). Elevated temperature material properties of advanced high strength steel alloys. *Journal of Constructional Steel Research*, *174*, 106299. https://doi.org/10.1016/j.jcsr.2020.106299

Blum, H. B., & Rasmussen, K. J. R. (2019). Experimental and numerical study of connection effects in long-span cold-formed steel double channel portal frames. *Journal of Constructional Steel Research*, *155*, 480-491. https://doi.org/10.1016/j.jcsr.2018.11.013

Blum, H. B., & Rasmussen, K. J. R. (2019). Experimental investigation of long-span cold-formed steel double channel portal frames. *Journal of Constructional Steel Research*, *155*, 316-330. https://doi.org/10.1016/j.jcsr.2018.11.020

Blum, H.B., Rasmussen, K.J.R. (2018). "Elastic Buckling of Columns with a Discrete Elastic Torsional Restraint." *Thin-Walled Structures*, 129(502-511). https://doi.org/10.1016/j.tws.2018.01.008

Blum, H. B., V. Z. Meimand, and B. W. Schafer (2014). "Flexural Bracing Requirements in Axially Loaded Cold-Formed Steel-Framed Walls." *Practice Periodical on Structural Design and Construction,* 20(4).

https://ascelibrary.org/doi/10.1061/%28ASCE%29SC.1943-5576.0000242

Conference Proceedings (* denotes presenting author)

Blum, H.B.*, and Kraus, W., "Structural Steel Fabrication with Mixed Reality", *Proceedings Tenth European Conference of Steel and Composite Structures*, Amsterdam, September 2023. https://onlinelibrary.wiley.com/doi/pdf/10.1002/cepa.2575

Koh, H., and Blum, H.B.*, "Shear connector design using data analytics approaches", *Proceedings Tenth European Conference of Steel and Composite Structures*, Amsterdam, September 2023. https://onlinelibrary.wiley.com/doi/pdf/10.1002/cepa.2561

Koh, H.*, and Blum, H.B., "Data-driven buckling capacity prediction of normal- and high-strength steel hollow structural section columns", *Proceedings of Structural Stability Research Council Annual Stability Conference*, Charlotte, NC, 2023.

Sippel, E.J.*, and Blum, H.B., "Stability of stainless steel unequal-leg angles with imperfect supports", *Proceedings of Structural Stability Research Council Annual Stability Conference*, Charlotte, NC, 2023.

Laracuente, M.E., Sippel, E.J.*, and Blum, H.B., "Stability Considerations of Laser Fused Unequal-Leg Angle Stainless Steel Columns", *Proceedings of Structural Stability Research Council Annual Stability Conference*, Charlotte, NC, 2023.

Xia, Y., Glauz, R.S., Schafer, B.W.*, Seek, M., and Blum, H.B., "Cold-formed steel strength predictions for combined bending and torsion", *Proceedings of Structural Stability Research Council Annual Stability Conference*, Charlotte, NC, 2023.

Koh, H., Rosson, B.T. *, and Blum, H.B., "Exploring machine learning for the stability analysis of rotary-straightened steel members with multiple stiffness reduction models", *Proceedings of The International Colloquium on Stability and Ductility of Steel Structures (SDSS)*, Aveiro, Portugal, September 2022. https://onlinelibrary.wiley.com/doi/10.1002/cepa.1843

Sippel, E.J.*, Blum, H.B., "Virtual Reality Field Trip of a Steel Building Under Construction", *Proceedings of American Society of Engineering Education*, Minneapolis, Minnesota, June 2022. https://peer.asee.org/40547

Zhang, L.*, Moen, C.D., Blum, H.B., and Marks, B., (2022). "Structural Analysis in Virtual Reality for Education with MBLY," *Proceedings CFSRC Colloquium*. http://jhir.library.jhu.edu/handle/1774.2/67719

Koh, H.*, and Blum, H.B., "Calibration and validation of the hole-drilling method to measure residual stresses in advanced high-strength cold-formed steel members." *Cold-Formed Steel Research Consortium (CFSRC) Colloquium*, 2022.

Xia, Y.*, Zhanjie L., and Blum, H.B., "Numerical study on residual stresses in press-braked advanced high-strength cold-formed steel angles by finite element simulation." *Cold-Formed Steel Research Consortium (CFSRC) Colloquium*, 2022.

Ding C.*, Xia Y., Akchurin D., Blum H.B., Li Z., Schafer B.W., "Structural Behavior of Advanced High Strength Steel: Ductility, Connections, Members." *Cold-Formed Steel Research Consortium (CFSRC) Colloquium*, 2022.

Laracuente, M.E.*, Sippel, E.J., and Blum, H.B., "Stability considerations of unequal-leg stainless steel columns", *Proceedings of Structural Stability Research Council Annual Stability Conference*, Denver, CO, 2022. https://www.aisc.org/education/continuingeducation/education-archives/stability-considerations-of-unequal-leg-angle-stainless-steel-columns/

Sippel, E.J.*, Ziemian, R.D., and Blum, H.B., "Buckling behavior of open web steel joists and joist girders",

Proceedings of Structural Stability Research Council Annual Stability Conference, Denver, CO, 2022.

Xia, Y.*, Schafer, B.W., and Blum, H.B., "Cold-formed steel strength predictions for torsion", *Proceedings of Structural Stability Research Council Annual Stability Conference*, Denver, CO, 2022.

Koh, H.*, Rosson, B.T., and Blum, H.B., "Stiffness reduction factor requirements for the stability analysis of rotary straightened W-shape members", *Proceedings of Structural Stability Research Council Annual Stability Conference*, Denver, CO, 2022.

Ding, C.*, Xia, Y., Akchurin, D., Li, Z., Blum, H.B., Schafer, B.W., "Simulation of Compressive Strength of Wall Studs Cold-Formed from Advanced High Strength Steels," *Proceedings of Structural Stability Research Council Annual Stability Conference*, Denver, CO, 2022.

Akchurin, D. *, Ding, C., Xia, Y., Blum, H.B., Schafer, B.W., Li, Z., "Optimization of cold-formed steel members considering reduced stiffness and strength due to cross-sectional instabilities," *Proceedings of Structural Stability Research Council Annual Stability Conference*, Denver, CO, 2022.

Xia, Y., Li, Z., Schafer, B.W., Blum, H.B.* (2021). "Experimental study on residual stresses in cold-formed advanced high-strength steel members", *Proceedings Ninth European Conference of Steel and Composite Structures*, Sheffield, UK.

Xia, Y.*, Yan, X., Gernay, T., Blum, H.B. (2021). "Experimental study of the behavior of HSLA and DP cold-formed high-strength steels at elevated temperature", *Proceedings Ninth European Conference of Steel and Composite Structures*, Sheffield, UK.

Friis, O. B., H. B. Blum, H. C. Yildirim. "Evaluation of post-weld treated steel welds subject to mechanical loading." In *Bridge Maintenance, Safety, Management, Life-Cycle Sustainability and Innovations, Proceedings of the Tenth International Conference on Bridge Maintenance, Safety and Management (IABMAS 2020)*, pp. 3708-3713. CRC Press, 2021.

Blum, H.B.*, and Moen, C.D. (2021). "Conducting a Column Buckling Test in 3D Virtual Reality", *Proc., SSRC Annual Stability Conference*, Louisville, KY [online]. https://www.aisc.org/education/continuingeducation/education-archives/stability-of-columns-s8/

Blum, H.B.*, and Li, Z. (2021). "Sensitivity of design parameters on the stability of apex connections in cold-formed steel portal frames", *Proc., SSRC Annual Stability Conference*, Louisville, KY [online].

Sippel, E.J.*, Ziemian, R.D., Blum, H.B. (2021). "Experimental verification of eccentrically loaded steel joists with non-symmetric sections", *Proc., SSRC Annual Stability Conference*, Louisville, KY [online].

Yan, X.*, Xia, Y., Blum, H.B., and Gernay, T. (2020). "Experimental investigation of the behavior of martensitic high-strength steels at elevated temperature," *Proceedings Eleventh International Conference on Structures in Fire*, Queensland, Australia [online].

Xia, Y., Sudhiwana, T., and Blum, H.B. (2020). "Experimental study on low temperature ductility of cold-formed steel," *Proceedings CFSRC Colloquium*. [no presentation]

Xia, Y.*, Yan, X., Gernay, T., and Blum, H.B. (2020). "Modeling of stress-strain relationship of advanced high-strength cold-formed steel at elevated temperature," *Proceedings CFSRC Colloquium*.

Ding, C.*, Li, Z., Blum, H.B., Xia, Y., Schafer, B.W. (2020). "Ductility Demands on CFS Structural Connections for Advanced High Strength Steel," *Proceedings CFSRC Colloquium*.

Yan, X.*, Xia, Y., Blum, H.B., and Gernay, T. (2020). "Experimental Study on the High Temperature Properties of Advanced High-Strength Cold-formed Steels," *Proceedings CFSRC Colloquium*.

Sippel, E.J.*, and Blum, H.B. (2020). "System analysis of non-symmetric cold-formed steel cross-section members," *Proceedings CFSRC Colloquium*.

Koh, H.*, and Blum, H.B. (2020). "A State-of-the-Art Review of Testing by Analysis in Cold-Formed Steel Design," *Proceedings CFSRC Colloquium*.

Sippel, E.J.*, Ziemian, R.D., Blum, H.B. (2020). "Analysis of non-symmetric cross-sections relative to the provisions of AISC 360-16." *Proc., SSRC Annual Stability Conference*, SSRC, Atlanta, GA. [presentation canceled due to COVID19]

Xia, Y.*, Blum, H.B. (2020). "Buckling mode characterization for high-strength cold-formed steel with in-situ 3D scanning." *Proc., SSRC Annual Stability Conference*, SSRC, Atlanta, GA. [presentation canceled due to COVID19]

Xia, Y., Li, Z., Schafer, B.W., Blum, H.B.* (2019). "Material Property Characterization of Advanced High Strength Cold-Formed Steel." *Proc., Seventh International Conference on Structural Engineering, Mechanics, and Computation*, Cape Town, South Africa.

Blum, H.B.*, Li, Z. (2019). "Stability of apex connections in cold-formed steel portal frames." *Proc., SSRC Annual Stability Conference*, SSRC, St. Louis, MO.

Peng, J., Bendit, J., and Blum, H.B.* (2018). "Experimental study of apex connection stiffness and strength of cold-formed steel double channel portal frames." *Proc., Twenty-fourth International Specialty Conference on Cold-Formed Steel Structures*, St. Louis, MO.

Rasmussen, K.J.R.*, Blum, H.B., and Rinchen (2018). "Behaviour and Design of Cold-Formed Steel Portal Frames." *Proc., Eighth International Conference on Thin-Walled Structures*, Lisbon, Portugal.

Blum, H.B.*, Rasmussen, K.J.R. (2017). "Design Method for Columns with Intermediate Elastic Torsional Restraint." *Proc., SSRC Annual Stability Conference*, SSRC, San Antonio, TX.

Blum, H.B.*, Rasmussen, K.J.R. (2016). "Buckling and design of column with intermediate elastic torsional restraint." *Proc., SSRC Annual Stability Conference*, SSRC, Orlando, FL.

Blum, H.B.*, Rasmussen, K.J.R. (2016). "Experiments on column base stiffness of long-span cold-formed steel portal frames composed of double channels." *Proc., Twenty-third International Specialty Conference on Cold-Formed Steel Structures*, Baltimore, MD.

Blum, H.B.*, Rasmussen, K.J.R. (2016). "Experiments on long-span cold-formed steel portal frames composed of double channels." *Proc., Seventh International Conference on Coupled Instabilities in Metal Structures*, Baltimore, MD.

Blum, H.B.*, Rasmussen, K.J.R. (2016). "Finite element modeling and parametric study of cold-formed steel portal frames." *Proc., Sixth International Conference on Structural Engineering, Mechanics, and Computation*, Cape Town, South Africa.

Blum, H. B., V. Z. Meimand, and B. W. Schafer* (2013). "Bracing for Flexural Buckling in Cold-Formed Steel-Framed Walls." *Proc., SSRC Annual Stability Conference,* SSRC, St. Louis, MO.

Conference Presentations without Proceedings (* denotes presenting author)

Koh, H.*, and Blum, H.B., "The impact of data-driven design approaches on shear connector reliability," *Engineering Mechanics Institute Conference*, Atlanta, GA, 2023.

Koh, H.*, Rosson, B.T., and Blum, H.B., "Comparison of stiffness reduction factors for rotary-straightened and hot-rolled W-shape members," *Engineering Mechanics Institute Conference*, Atlanta, GA, 2023.

Blum, H.B.* and Kraus, W.*, "Supplementing Steel Bridge Fabrication with Immersive Augmented Reality," *10th International Symposium on Visualization in Transportation*, Transportation Research Board,

Washington DC, 2022.

Blum, H.B.*, "Experimental evaluation of hot-rolled and laser-fused stainless-steel unequal-leg angle columns," *Stainless Steel in Structures 6th International Experts Seminar*, London, UK, 2022.

Koh, H.*, and Blum, H.B. (2022). "Stability Analysis of Rotary-Straightened Steel Members with Multiple Stiffness Reduction Models using Machine Learning," *Engineering Mechanics Institute Conference*, Baltimore, MD.

Koh, H.*, and Blum, H.B. (2022). "Design of Structural Steel Hollow Sections Using Machine Learning Techniques," *Engineering Mechanics Institute Conference*, Baltimore, MD.

Sippel, E.J.*, and Blum, H.B. (2022). "*Imperfection Analysis of In-Situ 3D Measurements of Stainless-Steel Unequal-Leg Angles for Computational Modeling*," *Engineering Mechanics Institute Conference*, Baltimore, MD.

Blum, H.B.* and Kraus, W.* (2022). "Applications for Smart Glasses and Augmented Reality in Structural Steel." *North American Steel Construction Conference*, Denver, CO.

Xia, Y., and Blum, H.B.* (2021), "Material properties of advanced high-strength cold-formed steel alloys subjected to subzero temperatures," *2021 Regional Conference on Permafrost and 19th International Conference on Cold Regions Engineering*, Virtual Conference.

Koh, H.*, and Blum, H.B. (2021). "Feature selection approach for sensitivity analysis of steel frames," *Engineering Mechanics Institute Conference*, Virtual Event.

Sippel, E.J.*, and Blum, H.B. (2021). "In-situ 3D deformation measurements and imperfection analysis of a steel joist," *Engineering Mechanics Institute Conference*, Virtual Event.

Yan, X.*, Xia, Y., Blum, H.B., and Gernay, T. (2021). "Characterization of advanced high-strength cold-formed steel at elevated temperature and after cooling down," *Engineering Mechanics Institute Conference*, Virtual Event.

Koh, H.*, and Blum, H.B. (2021). "Analysis of uncertainty correlation on system behavior in steel frames Using Machine Learning Platform," *Probabilistic Mechanics & Reliability Conference*, Virtual Event.

Research Reports

Blum, H.B. (2013). "Reliability-Based Design of Truss Structures by Advanced Analysis." *Research Report R936, Centre for Advanced Structural Engineering, School of Civil Engineering, The University of Sydney*, Sydney, New South Wales, Australia.

The main theme of my teaching philosophy is strengthening student engagement to improve positive attitudes towards learning. Harnessing modern technology, especially technology of interest to students, boosts students' engagement and involvement with the course content and increases their desire to participate and learn. Integrating technology in the form of immersive visualization, e.g., virtual and augmented reality, into the classroom changes how students interact with the teaching aids and interpret and analyze the lesson. This format of active learning has several benefits including the creation of more accessible lessons that reach students with diverse learning styles and the preparation of students for the technology they will encounter in their future careers. I structure my teaching to achieve the following four goals:

Goal 1: Equip students with problem-solving skills for addressing open-ended problems.

Often in the classroom we provide students with practice problems that have only one correct answer. The students may become accustomed to this binary methodology - they are either correct or incorrect. The real-world problems, especially for those in engineering fields, may have multiple workable solutions, and the engineer must decide which solution is optimal based on a variety of factors and constrains, and even so, there might not be a clear single best solution. As we educate students, we must train them to feel comfortable with making educated assumptions based on the data available and uncertainties, logically stepping through a solution, and communicating their process to others through technical writing. To achieve this objective, I employ three practices in my courses:

1. Scaffolding of practice problems. I scaffold my practice problems to guide students through the logical solution process. To help them get started on finding a solution, an outline is provided for the overall process. During problem solving, I pose questions in all steps in the outline to instill in them the need to use critical thinking at each step of the process. During class, I allow students to guide me through each step, without simply giving the answer. If a student provides an incorrect answer, I ask the class to explain why the proposed solution would not work. In this manner the students practice their problem solving and critical thinking skills. Overall, there is good participation from students in these discussions. In some instances, students find different paths to the same solution and can discuss amongst themselves which solution path was more efficient. I engage this practice in CEE 445 (Steel Structures 1), CEE 545 (Steel Structures 2), and CEE 649 (Special Topics: Structural Reliability).
2. Emphasis on technical writing. At the end of each major unit in Steel Structures I (CEE 445), students are tasked with writing a technical report based on an in-class analysis activity. The focus is on communicating their process and reasoning through appropriate plots, figures, and data tables to demonstrate how their solution is feasible. Students are provided feedback and those who received an unsatisfactory report can resubmit for an improved grade. This helps them with honing their writing skills and prepares them for their future where there may be multiple viable solutions, and therefore it is crucial that they can document and explain their solution process to others to enable informed decisions.
3. Collaboration with Professors of Practice. I strive to create end-of-semester open-ended design projects reflective of what graduates may encounter within their first few years in industry. For both CEE 445 and CEE 545 I have been working with Professors of Practice in the CEE department at UW-Madison, who offer interesting perspectives from their professional experiences. Student feedback indicated that the students felt it helped better prepare them for their careers.

Goal 2: Provide students with interactive 3D visualization tools.

We live in a three-dimensional world, yet often in education we teach in two-dimensions through printouts or slideshows. Some students are great at spatial visualization and can easily convert 2D images to 3D in their heads. This visualization skill is especially helpful in engineering fields; however, we should not limit engineering to only those with this innate skill set. Improved 3D visualization may help students achieve the lesson's learning objectives as they can see physical behaviors in a realistic manner and can make the content more accessible to those who struggle with 3D visualization. To achieve this objective, I

led the development of two interactive teaching aids based on 3D visualization. These visualizations are used in my CEE 445 course.

1. Virtual reality (VR) building plan matching game. This teaching aid helps students convert 2D building plans to a 3D realistic model of a building. The format is a virtual reality (VR) game, which many students are already comfortable and familiar with. Students are given immediate feedback during the game and helpful hints and tips to help them achieve the objective.
2. Augmented reality (AR) bolted steel connection. This module helps students visualize 3D connection fracture failure modes. Furthermore, they can interact with the model to pull the fractured connection apart. The aim of this teaching aid is to improve identification of fracture patterns and identify areas in shear and tension through 3D visualization and interaction.

I continue to develop interactive teaching aids, including a virtual reality tour of a metal building as part of the educational outreach aims of an NSF funded project. Additionally, I solicit feedback on the interactive teaching aids from students and other educators with the aim to revise and improve the teaching aids.

Goal 3: Improve the availability of out-of-classroom activities.

Students spend most of their educational career in the classroom and occasionally in hands-on labs or activities. One important feedback provided in graduation surveys is that they struggle to see the connections between classroom activities and the real world. Therefore, I aim to take my students on field trips directly related to our course content, which includes a steel fabricator visit for CEE 445 and a trip to a metal building manufacturer for CEE 545. For those who are unable to attend the scheduled physical field trip visit, I provide them with access to a virtual fabrication shop tour. The virtual tour is in 360° and can be viewed in a VR headset or on a screen and is fully narrated. Furthermore, field trips to construction sites are not always an option for a variety of reasons including safety, finances, availability, timing, disability access, etc. To ameliorate this, I led the development of a virtual reality field trip of a steel skyscraper under construction. The format of this teaching aid is a narrated 360° virtual reality tour. At each stop on the tour, the narrator explains a concept, and images pop up to show the students where to look or show supplemental graphics. I plan on continuing to integrate these virtual tours into Steel Structures Design courses as students have shown excitement with the tours.

Goal 4: Incorporate modern tools, software, and technology to prepare students for their future careers.

An important goal in the way I approach teaching is to provide students with a foundation to accurately use the tools of the trade based on their understanding of fundamentals. Structural engineers frequently use structural analysis software to analyze and design a structural system, however, the output is only as accurate as the user input and the user understanding of structural behavior. To achieve a balance, I use modern design tools in class, but emphasize the importance of understanding the input and checking and critiquing the results. Students in CEE 445 and CEE 545 use multiple structural analysis software packages so that they do not learn to use a single tool, but rather know how to apply their knowledge to use whichever tool is more appropriate for the job. Additionally, I have employed computational notebooks as a tool so students can dynamically analyze and interpret their results. A computational notebook combines code, equations, and narratives, etc., in one tool where the user can interact with the notebook by changing the input and directly noting the change in output. The teaching environment created with the use of computational notebooks helps them easily gauge how specific input parameters have a more significant effect on the system. This practice increases their understanding of structural system behavior and how uncertainties influence a structural analysis. This active learning approach is more effective than passive lectures and allows the student to take onus of their studies.

Dr. Benjamin Schafer
Willard and Lillian Hackerman Professor of Civil and Systems Engineering
Johns Hopkins University

Website: https://engineering.jhu.edu/faculty/benjamin-schafer/
Phone: 410-516-6265
Email: schafer@jhu.edu

Dr. Ronald Ziemian
Presidential Professor of Civil & Environmental Engineering
Bucknell University

Website: https://www.bucknell.edu/fac-staff/ronald-ziemian
Phone: 570-577-1784
Email: ziemian@bucknell.edu

Dr. Kim Rasmussen
Challis Professor of Civil Engineering
Chairman, Centre for Advanced Structural Engineering
The University of Sydney

Website: https://www.sydney.edu.au/engineering/about/our-people/academic-staff/kim-rasmussen.html
Phone: +61 2 9351 2125
Email: kim.rasmussen@sydney.edu.au

Dr. Barry Rosson
Professor, Department of Civil, Environmental and Geomatics Engineering
Florida Atlantic University

Website: https://www.fau.edu/engineering/directory/faculty/rosson/
Phone: 561-297-4554
Email: rosson@fau.edu

Dr. Tom Sputo
Technical Director, Steel Deck Institute
Master Lecturer Emeritus, University of Florida
Consulting Structural Engineer, Sputo and Lammert Engineering, LLC, Gainesville, Florida

Website: https://www.essie.ufl.edu/people/name/thomas-sputo/
Phone: 352-317-3086
Email: sputo@ufl.edu; tsputo50@gmail.com

It is my long-term career goal to develop the next generation of structural design methods for steel structures which will use data-driven approaches to account for uncertainty and safety and will optimize for performance objectives in the structural steel and cold-formed steel industries. This approach will enable engineers to create unique and efficient infrastructure, and most importantly, to advance the development of infrastructure that is resilient to extreme loads and natural hazards. My previous and current research focuses on the design and analysis of steel, cold-formed steel, and stainless-steel structures, structural stability, and structural reliability through computational modeling and experimental methods. My research portfolio encompasses both conventional structural engineering research and collaborative, multi-disciplinary projects. To improve the structural design, analysis, and construction processes, I have begun to integrate new technology, including augmented reality and data-driven approaches. My research presents a novel combination of computational models, advanced system analysis, experimental work, and technology integration along with strong academia-industry partnerships. My four main research foci are described below.

Resilient infrastructure subjected to hazards in a changing environment

Natural hazard events, such as high wind events, are becoming more prevalent due to the changing environment. Furthermore, infrastructure may be prone to larger temperature variations under normal operating conditions. We need to prepare the next generation of infrastructure to withstand these increasing demands. My research group is currently investigating the resiliency of metal buildings, a common building system typically composed of steel members, subjected to transient internal pressure from tornadoes (NSF Award #2053364). This is a collaborative project in which my research team provides expertise in finite element modeling and steel structures and collaborates with a wind engineering team at Texas Tech University. Our aim is to determine how to make the structural system more resilient and reduce damage after tornadoes. We do this through advanced system modeling of steel structures accounting for uncertainty and interactions among the structural elements, incorporating the wind tunnel results from the wind research team. This collaborative project will benefit society by improving metal building designs, which are often used as critical infrastructure in rural areas. In addition to hazards from tornadoes, my group has also researched the material properties of advanced high strength cold-formed steel at both subzero and elevated temperatures to determine predictive equations which can be employed in advanced structural modeling. Subzero performance is important if infrastructure is to be built in high latitude regions, which are becoming more habitable as the earth warms. Elevated temperature characterization is critical in performance-based design when considering potential fire hazards. This research will help to advance the next generation of building materials.

Historic structures must also be resilient in our changing climate. My group is part of multidisciplinary project with collaborations among structural engineering, geological engineering, and computer engineering researchers to develop a method for monitoring and assessing historic structures subjected to changing climate conditions. The project will focus on monitoring the sites using non-destructive methods, robust finite element modeling of the infrastructure subjected to adverse climate conditions, and augmented reality visualization to assist with inspections. We are working with the Construction Engineering Research Lab, which is part of the Department of Defense.

Comprehensive structural system analysis

Structural system analysis, a type of analysis where the entire structural system including all members and connections is analyzed together to account for member interactions, can lead to improved performance over the conventional single-member analysis approach. Structural system analysis can lead to structures that are more cost competitive, predictable, and efficient. With the improvement in technology, robust computational modeling of structural systems is becoming easier and computationally cheaper. Accurate input, analysis capabilities, and confidence must be obtained to ensure acute computational model output. My group has worked on quantifying critical input required for advanced computational modeling and analysis and advanced modeling techniques required to advance the field through system analysis.

With regards to input, my team has worked on quantifying residual stresses in press-braked advanced high-strength cold-formed steel (AHSS) through sectioning, hole-drilling, and modeling approaches. Obtaining accurate residual stress measurements through experiments is often considered challenging but necessary for accurate design using a systems level analysis as residual stresses affect yielding and loss of member stiffness, which influences the behavior of the structural system. The residual stress values and distributions acquired during the project can be used for future robust finite element modeling of AHSS members and systems to help bring structural members composed of advanced high-strength steels to the construction industry. High strength steels have a high strength-to-weight ratio and may be beneficial in lowering construction costs by reducing materials needs and transportation costs.

With regards to analysis capabilities, my research group has evaluated the performance of a new line element to accurately model nonsymmetric behavior in steel members and systems, including steel joists with nonsymmetric loading conditions. A line element is the most widely used method of structural analysis for most structural design companies, however, the standard line element does not account for nonsymmetric behavior. This work was funded by the American Iron and Steel Institute and the Steel Joist Institute. To ensure confidence in the results, an experimental study was conducted to validate the finite element output on the steel joist system. The validated modeling approach has enabled industry to analyze their non-symmetric structural systems more accurately.

With regards to structural reliability, my research group is working on a novel specification-driven effort to implement system reliability across steel joist and deck systems. Funded by the Steel Joist Institute and the Steel Deck Institute, we are investigating steel joist subsystem reliability to help uncover potential benefits of a reliability-driven design approach to open-web steel joist systems, beginning with the reliability of single joists. This will then be followed with system reliability of steel deck. Afterwards, the research will progress to joist roof systems. The system reliability approach considers measured uncertainties in the input parameters, and the robust computational models required for the analysis are validated and calibrated with experimental data. The results of this study will help improve both safety and efficiency of these steel-based structural systems.

Integrating technology innovations in the structural steel industry

My group implements new technologies and data-driven approaches into the structural design and construction processes. With regards to new technologies, we are evaluating the use of mixed reality to improve the efficiency and quality control of structural steel fabrication through interactive holograms that integrate key information from design files through a project funded by the American Institute of Steel Construction. The aim of the project is to augment the existing steel fabrication method by creating faster and more efficient quality control processes and proposing step-by-step guides for steel fabricators for complex connections and training of a rapidly changing workforce. Interest in this area is growing in the steel community, which resulted in a recently funded project by the Steel Founders' Society of America (Prime: Department of Defense) to develop and implement this technology in a local steel foundry.

Data-driven design approaches and big data can benefit the steel design industry if used appropriately. The Steel Deck Institute has funded my team to investigate data-driven approaches to parse a large shear connector database into groupings which may permit larger resistance factors in the design process, thereby improving the design efficiency. My team also investigated using machine learning to identify important features in a dataset considering the effects of highly imbalanced and high dimensional data commonly present in structures. Furthermore, we also investigated the comparison of conventional interpolation methods to machine learning methods to accurately predict the strength and failure modes of steel hollow section compression members from a large database grouped into experimental only, computational only, or combined. This information is crucial to advancing data-driven design approaches for a faster design process while ensuring adequate safety.

We are also examining how to scan structural steel components with a combined structured light and infrared laser scanner and measure geometric imperfections from the resulting 3D point clouds. Determining and quantifying specific geometric imperfections from dense 3D point clouds is nontrivial. Eventually, the geometric information can be used as input in finite element analyses.

Advancing the steel industry through academia-industry partnerships

My research group is active in several industry-funded projects that are updating design provisions to ensure adequate safety in newly designed structures. One project, funded by the American Iron and Steel Institute (AISI), involved a computational-based parametric study on commonly produced cold-formed C and Z cross-sections subjected to torsion and combined bending and torsion at various interaction levels. The parametric study results were shared with the relevant AISI subcommittee to update design provisions in the AISI Specification. Another project, supported by the American Institute of Steel Construction (AISC), evaluated the strength of stainless-steel unequal leg angle compression members. The project included imperfection analysis, member testing, residual stress measurement, and computational modeling to expand the test database. The collected data will be shared with AISC professional committees to produce updated design recommendations for the AISC Specification. A third project, funded by the Steel Joist Institute (SJI), investigated the interactions of back-to-back angles in steel joist and joist girder chord members relative to flexural-torsional buckling behavior, with the aim of determining appropriate design guidance for the failure mode of built-up joist chord members under compression for the SJI Specification. AISI also funded my group to conduct a comprehensive literature review of testing by analysis provisions across multiple fields and standards from a variety of countries with the aim to determine how to best implement testing by analysis into the AISI standards. These projects all aim to improve accurate modeling of non-symmetric members which is vital to advance data-driven design approaches and innovative design considerations.

Future directions

My future research directions with focus on three main areas: (1) infrastructure resilience to changing climates, (2) advanced visualization and extended reality in structural engineering, and (3) next generation structural design. Over the next few years, I would like to expand into investigating non-structural energy-dissipating building elements to improve building resistance to high lateral loads (e.g., wind and earthquake) and additionally freeze/thaw effects on infrastructure. Later, I look forward to collaborating with multidisciplinary teams to solve big-picture infrastructure challenges regarding holistic system performance to meet the needs of a growing population.

I am currently working on creating a new research center, R^3: Holistic Steel Systems – Reliable, Robust, Responsible. The R^3 initiative is a new industry-academia partnership to study steel design as a holistic system – including the impact of sustainability and resilience. The Center will focus its efforts on the integration of all of the three R's into a holistic system, where the aspects of Responsibility are not considered separately as a Yes-No decision, but as a functional aspect of structural design. The Center will seek industry sponsors from both trade associations and individual manufacturers of steel and steel construction products. Funding from sponsors will be used to support pilot projects that will help gain external funding sources from government agencies. Later, the Center will expand and pursue non-industry funding sources to extend industry resources. There is currently interest among several industry groups, and I will be recruiting additional members over the next year.

Journal of Constructional Steel Research 190 (2022) 107116

Contents lists available at ScienceDirect

Journal of Constructional Steel Research

journal homepage: www.elsevier.com/locate/jcsr

Elevated temperature and post-fire stress-strain modeling of advanced high-strength cold-formed steel alloys

Yu Xia [a], Xia Yan [b], Thomas Gernay [b], Hannah B. Blum [a,*]

[a] Department of Civil and Environmental Engineering, University of Wisconsin, Madison, USA
[b] Department of Civil and Systems Engineering, Johns Hopkins University, USA

ARTICLE INFO

Keywords:
Cold-formed steel
Stress-strain modeling
Fire safety engineering
Advanced high-strength steel
Ramberg-Osgood model

ABSTRACT

Advanced high-strength cold-formed steels (AHSS) have been developed with yield strengths up to 1250 MPa and ultimate strengths up to 1900 MPa. Accurate stress-strain modeling of these new steel alloys are required for eventual application of AHSS into the building construction industry, including the material behavior of AHSS subjected to elevated temperatures. A series of new constitutive material models are proposed based on the experimental AHSS stress-strain database at elevated temperatures (i.e., steady-state and transient-state test methods) and post-fire scenario (i.e., residual test method). The stress-strain curves from experiments on two families of AHSS, including dual phase steel with nominal yield strengths of 340 MPa and 700 MPa, and martensitic steel with nominal yield strengths of 1030 MPa and 1200 MPa, reported in a previous study are considered. Existing stress-strain models are investigated and fit to the AHSS database, in addition to the development of new material models. The required input parameters of the proposed stress-strain models are determined, and their corresponding predictive expressions are proposed. It is shown the stress-strain behaviors of AHSS could be accurately described by the proposed models. The data generated by this research addresses fire safety design and will be essential in supporting the adoption of these next-generation steels in future infrastructure.

1. Introduction

Recent advances in steel manufacturing processes have led to materials with significantly enhanced capabilities at a competitive cost. New grades of steel, referred to as Advanced High-Strength Steels (AHSS), have been recently developed. AHSS are steels with unique microstructures utilizing complex deformation and phase transformation processes to achieve unprecedented strength and ductility combinations. The design and manufacture of AHSS require a careful selection of chemical compositions and precisely controlled heating and cooling processes. Subsequently, AHSS exhibit a multiphase microstructure containing one or more phases different from ferrite, pearlite, or cementite. Instead, these phases, for example, include martensite, bainite, austenite, and/or retained austenite that are sufficient in quantities to produce unique mechanical properties [1]. AHSS include new grades of steels with yield strengths up to 1250 MPa, ultimate strengths up to 1900 MPa, and tensile elongations upwards of 20% to 30% [1]. In addition, different from conventional steels, the terminology AHSS is classified by its metallurgical designation rather than the steel grades. As a result, AHSS can have a broader range of grades (e.g., with ultimate strength as low as 440 MPa and yield strength as low as 210 MPa) than the conventional high strength steels [1].

Although AHSS have not yet been adopted as a structural material in the construction industry, AHSS have been utilized widely in the automobile industry [1]. However, the past two decades have shown an increase in the use of conventional high strength structural steel (HSSS) in infrastructure. For example, Beijing National Stadium (2008) and China Central Television Headquarters (2012) in Beijing adopted Q460 steel as the main structural material, 1 Manhattan West (2019) in New York adopted steel with $\sigma_y = 485$ MPa in its perimeter steel moment frame, and Friends Arena (2012) in Stockholm used S460, S690, and S900 steel members for the chords [2–4]. These cases show that the quantity and quality demands for high strength steel as structural material have rapidly developed around the world [2,5], indicating a promising prospect. Adopting AHSS in the construction industry can provide many unique advantages, notably with cold-formed steel (CFS) structures, which provide efficient, lightweight, and resilient solutions for a range of building applications. Nevertheless, these novel materials'

* Corresponding author.
E-mail address: hannah.blum@wisc.edu (H.B. Blum).

https://doi.org/10.1016/j.jcsr.2021.107116
Received 1 June 2021; Received in revised form 14 December 2021; Accepted 21 December 2021
Available online 10 January 2022

behavior must be understood and characterized under extreme environments that may arise in structural applications, including high temperatures scenarios resulting from fire. In the current design codes [6–9], the deterioration of critical mechanical properties, including elastic modulus and yield strength at elevated temperature are recommended based on researches primarily focused on hot-rolled steels (HRS). Furthermore, the design guidance of the structural steel performance after the cooling down from the elevated temperature is limited, and research on the mechanical property deterioration of cold-formed high strength steel subjected to fire loads is extremely limited or non-existent. At ambient, the yield strength and tensile strength of CFS members increase due to the cold-forming process. However, these strength increases quickly deteriorate when the steel is exposed to fire, and this phenomenon is even more severe on high strength steels [10].

In this study, thorough discussions on the development of the constitutive relationship of AHSS at elevated temperature and after cooling down are carried out. Two dual phase steel sheets (with nominal yield strengths of 340 MPa and 700 MPa) and two martensitic steel sheets (with nominal yield strengths of 1030 MPa and 1200 MPa) were recently studied experimentally by the authors [11,12]. The mechanical and geometric characteristics of the AHSS experimental stress-strain curves are summarized. The modeling of the AHSS stress-strain relationship in different fire-related scenarios is discussed to provide accurate descriptions for advanced numerical simulation. Firstly, existing stress-strain models for steel at elevated temperature and after cooling down are reviewed and calibrated to best fit the AHSS experimental stress-strain data, however, it was determined that updated models are necessary to accurately fit the AHSS data. Secondly, based on the characteristics of the AHSS experimental stress-strain curves, two stress-strain models are developed for two different strain hardening behaviors. The fit accuracy for both proposed models is verified with the AHSS data in addition to other steel grades with similar stress-strain behaviors. Thirdly, a discussion on the prediction of model parameters as functions of test temperature is carried out, so that the stress-strain curve can be predicted at any given temperature within the temperature range. Finally, three examples for applying the proposed models corresponding to three different elevated temperature test methods are presented to help readers better understanding the application of the models.

2. Review on high temperature studies and existing steel stress-strain models

The behavior of materials exposed to fire is generally characterized using either the steady-state test method or the transient-state test method. For the steady-state test, the specimen is heated to the assigned elevated temperature until the specimen temperature is stabilized and then uniaxially pulled till fracture. The steady-state test's output is directly the stress-strain curve. For the transient-state test, the specimen is loaded to and stabilized at the assigned stress level and then gradually heated until fracture. The transient-state test output is the strain-temperature relationship, which can be transferred to the stress-strain relationship. The steady-state test method is widely employed in existing literature [10,13–24] to investigate the material properties of conventional CFS, stainless steel, and high-strength CFS at elevated temperature, for this test method is easy to implement, and the test result is straightforward. Many researchers also employ the transient-state test method [14–16,18,21,25] because it can accurately mimic the actual situation when steel is exposed to fire. However, the transient-state test has several drawbacks. Specifically, it is more complex to conduct and post-process. The generated stress-strain curve typically includes sparse data points and only covers a relatively small strain range.

The steel post-fire material behavior is commonly simulated by the residual test method. Data has been reported by several authors for CFS [17,26–33]. For the residual test, the specimen is heated to the assigned high temperature until the specimen temperature is stabilized, then cooled down to the ambient temperature, and finally pulled uniaxially until fracture. The residual test method directly outputs the stress-strain curve, and the residual stress-strain curve consists of a large number of data points covering the whole strain range from the origin to the fracture point.

2.1. Steady-state tests

From the existing steady-state test results for CFS, most stress-strain curves at elevated temperature show a nonlinear rounded curve shape, where the Ramberg-Osgood (R-O) equation [34], as shown in Eq. 1, is the most widely used model to describe the stress-strain relationship:

$$\varepsilon = \frac{\sigma}{E} + p\left(\frac{\sigma}{\sigma_p}\right)^n \quad \text{for} \quad 0 \le \sigma \le \sigma_u \tag{1}$$

where σ is stress, which is the model input, E is elastic modulus, p is the predefined plastic strain, σ_p is the proof stress when the plastic strain equals p, and n is the exponential coefficient determining model curvature.

Previous research has made various updates on the original R-O model (Eq. 1) to fit the experimental stress-strain curves from studies on different types and grades of CFS for both ambient and elevated temperature cases. The R-O model updates for CFS at elevated temperatures can be generally classified into two categories.

The first category includes the addition of a β factor. Although some minor differences might exist in the forms adopted by different studies, one representative expression is shown in Eq. 2 and is referred to as the *one-stage R-O model* hereinafter:

$$\varepsilon_T = \frac{\sigma_T}{E_T} + \beta\left(\frac{\sigma_{yT}}{E_T}\right)\left(\frac{\sigma_T}{\sigma_{yT}}\right)^n \quad \text{for} \quad 0 \le \sigma_T \le \sigma_{uT} \tag{2}$$

where β is a numerical parameter, and σ_y is the yield strength. The subscript T for any material property stands for this property at temperature T from the test.

Two different methods were developed in adopting the one-stage R-O model. For the first method, β is fixed as a constant and n is given as a function of T. For example, various β and n were determined in [10,14,20–22,35] for a variety of CFS and stainless steel by adopting this method. For the second method, n is fixed, while β varies at different test temperatures, for example, which was adopted in [13].

The second category of updates includes the transformation from the original one stage R-O model to a two-stage model. This model type will be referred to as the *two-stage R-O model* and is derived from the two-stage R-O models at ambient (e.g., [36]). Chen and Young [16,18] studied the material properties of cold-rolled EN 1.4462 and EN 1.4301 stainless steels up to 960°C as well as G450 and G550 CFS up to 970 °C. They adopted and updated the two-stage models for stainless steel at ambient [36,37] to describe their experimental stress-strain curves. The expressions of the two-stage model are shown in Eq. 3 for the first stage and Eq. 4 for the second stage:

$$\varepsilon_T = \frac{\sigma_T}{E_T} + 0.002\left(\frac{\sigma_T}{\sigma_{yT}}\right)^n \quad \text{for} \quad 0 \le \sigma_T \le \sigma_{yT} \tag{3}$$

$$\varepsilon_T = \frac{\sigma_T - \sigma_{yT}}{E_{yT}} + \varepsilon_{uT}\left(\frac{\sigma_T - \sigma_{yT}}{\sigma_{uT} - \sigma_{yT}}\right)^m + \varepsilon_{yT} \quad \text{for} \quad \sigma_{yT} < \sigma_T \le \sigma_{uT} \tag{4}$$

where n and m are the exponential coefficients for the first and second stage respectively, ε_{uT} is the ultimate strain, σ_{uT} is the ultimate strength, and E_{yT} is the tangential modulus at the yield strength which is calculated by Eq. 5.

$$\frac{1}{E_{yT}}=\frac{\partial\varepsilon_T(\sigma_T)}{\partial\sigma_T}\bigg|_{\sigma_T=\sigma_{0.2T}}=\frac{1+0.002n\frac{\sigma_T^{n-1}}{\sigma_{0.2T}^{n}}E_T}{E_T}\bigg|_{\sigma_T=\sigma_{0.2T}}=\frac{1+0.002n\frac{E_T}{\sigma_{0.2T}}}{E_T}\Rightarrow E_{yT}=\frac{E_T}{1+0.002n\frac{E_T}{\sigma_{0.2T}}} \tag{5}$$

Imran et al. [23] studied the mechanical properties of tensile coupons cut from Grade 350 CFS square hollow section up to 800 °C. They used Eq. 3 for the first stage and proposed a different expression for the second stage as shown in Eq. 6,

$$\varepsilon_T=\frac{\sigma_T-\sigma_{0.2T}}{E_{0.2T}}+\alpha\left(\frac{\sigma_T-\sigma_{0.2T}}{\sigma_{uT}-\sigma_{0.2T}}\right)^m+\varepsilon_{0.2T}\quad\text{for}\quad\sigma_{0.2T}<\sigma_T\le\sigma_{uT} \tag{6}$$

where α is a numerical parameter that is predicted as a linear function of T, n is predicted as piece-wise linear functions of T, and m is given as 3.

Gardner et al. [19] analyzed the performance of stainless steel alloys at elevated temperatures from existing resources and updated the second stage expression based on an updated two-stage R-O model at ambient [38]. The updated expression is shown in Eq. 7. The exponential coefficients n and m were given based on T and steel grade.

$$\varepsilon_T=\frac{\sigma_T-\sigma_{0.2T}}{E_{0.2T}}+\left(0.02-\varepsilon_{0.2T}-\frac{\sigma_{t2.0T}-\sigma_{0.2T}}{E_{0.2T}}\right)\left(\frac{\sigma_T-\sigma_{0.2T}}{\sigma_{t2.0T}-\sigma_{0.2T}}\right)^m+\varepsilon_{0.2T}\quad\text{for}\quad\sigma_{0.2T}<\sigma_T\le\sigma_{uT} \tag{7}$$

For both one-stage and two-stage R-O models, σ_T is the model input, and ε_T is the model output. Also, the derivatives of the model expressions indicate the model expressions are monotonic-increasing. Therefore, the models can depict the stress-strain relationship up to the ultimate point. The strain-softening after the ultimate point cannot be predicted by R-O models.

In addition to the numerical parameters (e.g. β, p, n, m, etc.), some material-property parameters are also required by these models (e.g. E_T and σ_y of Eq. 2). Temperature-dependent predictive equations for the material properties are needed in the stress-strain model to enable transient structural fire analyses. These equations are developed from statistical analysis of the experimental data. As different material properties of CFS can exhibit different performance depending on the test temperatures, predictive equations are often formulated as piecewise functions. Two different approaches are found in the literature. For the first approach, a unified equation with several numerical coefficients to be determined is used as the predictive equations for all required material properties. For example, Eq. 8 is adopted by [15,16,18], Eq. 9 is adopted by [14,21], Eq. 10 is adopted by [29], and Eq. 11 is adopted by [23]:

$$R_{X_T}=a-\frac{(T-b)^c}{d} \tag{8}$$

$$R_{X_T}=a(T-b)^c+d \tag{9}$$

$$R_{X_T}=a+\frac{c}{T}(T-d)^b \tag{10}$$

$$R_{X_T}=\frac{1}{a+be^{cT}} \tag{11}$$

where R_{X_T} is the retention factor for material property X at temperature T, which is defined as the ratio between a parameter X_T at T and this parameter X_0 at ambient, and a, b, c, and d are the numerical coefficients to be calibrated.

The other approach uses a combination of several basic functions (e.g., linear, power, and exponential) to provide the piecewise function of T as the predictive equations for the material-property parameters required by the stress-strain models. For example, the elastic modulus, strengths, and strains of the steels being studied in [10,20] are predicted by piecewise linear or power functions of T.

2.2. Transient-state tests

The transient-state test method was adopted in the following studies. Outinen and Mäkeläinen [25] investigated the material properties of S350GC + Z CFS at elevated temperature. The strain-temperature relationships were converted to stress-strain curves from ambient to 1000 °C. Chen and Young [16,18] studied the material properties of EN 1.4462 and EN 1.4301 cold-formed stainless steels at elevated temperature up to 760 °C as well as G450 CFS at elevated temperature up to 660 °C. Huang and Young [15] examined the material properties of a cold-formed lean duplex stainless steel (EN 1.4162) and reported stress-strain curves up to 750 °C. However, no stress-strain model designed for the transient-state test results was proposed in the above studies. Chen and Ye [14,21] studied the material properties of G550 CFS and Q345 CFS up to 550 °C. The converted stress-strain relationship was modeled by the one-stage R-O model (Eq. (2)), where $A=\beta\cdot(\sigma_{yT}/E_T)$ was given as different constants based on different steel types and different test temperature ranges and n was given as polynomials for different T.

2.3. Residual tests

Tao et al. [39] analyzed the post-fire behavior of structural and reinforcing steels from eight different studies. The experimental stress-strain curves from these studies show a distinct yield point and yield plateau, followed by the nonlinear strain hardening and softening process. Inspired by Mander's model for steel at ambient [40], a four-stage stress-strain model was proposed to simulate the post-fire constitutive relationship for the investigated steels accurately, and the expressions for the model are given in Eq. 12 to Eq. 15 respectively:

$$\sigma_T=E_T\varepsilon_T\quad\text{for}\quad0\le\varepsilon_T\le\varepsilon_{yT} \tag{12}$$

$$\sigma_T=\sigma_{yT}\quad\text{for}\quad\varepsilon_{yT}<\varepsilon_T\le\varepsilon_{shT} \tag{13}$$

$$\sigma_T=\sigma_{uT}-(\sigma_{uT}-\sigma_{yT})\left(\frac{\varepsilon_{uT}-\varepsilon_T}{\varepsilon_{uT}-\varepsilon_{shT}}\right)^\rho\quad\text{for}\quad\varepsilon_{shT}<\varepsilon_T\le\varepsilon_{uT} \tag{14}$$

$$\sigma_T=\sigma_{uT}\quad\text{for}\quad\varepsilon_{uT}<\varepsilon_T \tag{15}$$

where subscript T represents the target temperature for the residual test, ε_{shT} is the strain at the end of the yield plateau and the onset of the nonlinear strain hardening, and ρ is the exponential coefficient determining the nonlinearity of the strain hardening process and it is calculated by Eq. 16.

$$\rho = E_{shT}\left(\frac{\varepsilon_{uT} - \varepsilon_{shT}}{\sigma_{uT} - \sigma_{yT}}\right) \quad \text{for} \quad \varepsilon_{shT} < \varepsilon_T \leq \varepsilon_{uT} \tag{16}$$

Gunalan and Mahendran [26] studied the post-fire mechanical properties of G300, G500, and G550 CFS alloys cooling down from up to 800 °C. A distinct yield point and yield plateau were observed in both the post-fire and the ambient results. More significant strength deterioration was observed for G500 and G550 than G300. The experimental stress-strain curves were simulated by the model proposed by Tao et al. [39].

Huang and Young [29] studied the post-fire behaviors of ferritic stainless steel alloys (EN 1.4003) after exposure to high temperatures up to 1000 °C. The experimental results show different stress-strain curve shapes after cooling down from various elevated temperature ranges. For the cases with rounded nonlinear stress-strain curve shape, a two-stage R-O model (Eq. 3 and Eq. 4) is adopted. For the cases with a distinct yield point followed by yield plateau and nonlinear strain hardening, an updated inverse form of the model proposed by Tao et al. [39] is adopted.

Kesawan and Mahendran [31] studied the post-fire material properties of G350 and G450 CFS alloys. A distinct yield point and yield plateau followed by nonlinear strain hardening and softening process were observed from all postfire tests, regardless of the stress-strain curve shape at ambient. An elastic-perfectly-plastic model is recommended for the modeling of post-fire stress-strain curves.

Li and Young [32] investigated the post-fire material properties of high strength CFS alloys after exposure to high temperature up to 1000 °C. The test specimens were cut from three hollow sections. From the results, nonlinear rounded stress-strain behaviors are observed for all ambient cases. For G700 specimens, a distinct yield point and yield plateau were observed when T was between 300 °C and 1000 °C. For G900 specimens, a distinct yield point and yield plateau were observed when T is between 300 °C and 600 °C, and the nonlinear rounded stress-strain curve was observed when T is between 700 °C and 1000 °C. No constitutive model was proposed in their study.

Singh and Singh [33] studied the residual mechanical properties of YSt-310 CFS alloys exposed to target temperatures between 300 °C to 800 °C. The specimens were cut from three hollow sections with different dimensions. At ambient, the stress-strain curves show gradual yielding with a moderate degree of strain hardening. For the high-temperature cases, a distinct yield point and yield plateau followed by prominent strain hardening were observed. The two-stage R-O model [36] was recommended for the ambient test, while the model proposed by Tao et al. [39] was recommended for the residual tests.

From existing residual tests, some CFS alloys [29,31–33] show nonlinear rounded stress-strain behaviors (referred to as Mode 1 behavior hereinafter) at ambient and after cooling down from relatively lower temperatures, but show linear elastic stress-strain behaviors ending at a distinct yield point followed by a yield plateau (referred to as Mode 2 behavior hereinafter) after cooling down from relatively higher temperatures.

Mode 2 behavior is frequently observed in the ambient tensile tests for HRS. Therefore, existing stress-strain models at ambient proposed for HRS might be able to describe Mode 2 residual stress-strain behaviors for CFS. In engineering practice, several multiphase linear models have been widely adopted, for example, the elastic-perfectly-plastic model [41] and the elastic-linearly hardening model [42]. These models require a few parameters, but the model accuracy is sacrificed at various levels depending on the specific model under consideration. These models are feasible for engineering practice because they provide a less accurate but conservative steel behavior simulation. However, for advanced numerical simulation that requires a high accuracy level, these simple linear models may not be sufficient.

Based on the existing ambient tensile tests of HRS, Yun and Gardner [43] collected over 500 stress-strain curves covering nominal yield strengths from 235 MPa to 960 MPa, and proposed a bilinear plus nonlinear hardening model inspired by Mander's model [40]. The model uses strain as input and stress as model output. The linear elastic portion is modeled as $\sigma(\varepsilon) = E\varepsilon$ up to ε_y and the yield plateau is modeled as $\sigma(\varepsilon) = \sigma_y$ for $\varepsilon_y < \varepsilon \leq \varepsilon_{sh}$. For $\varepsilon_{sh} < \varepsilon \leq \varepsilon_u$, the nonlinear strain hardening portion is normalized and modeled by Eq. 17:

$$\sigma(\varepsilon) = \sigma_y + (\sigma_u - \sigma_y)\left(K_1\varepsilon_n + \frac{K_2\varepsilon_n}{\left(1 + K_3\varepsilon_n^{K_4}\right)^{\frac{1}{K_4}}}\right) \quad \text{for} \quad 0 \leq \varepsilon_n \leq 1 \tag{17}$$

where ε_{sh} is the strain at the end of the yield plateau and the onset of the nonlinear strain hardening, and ε_n is the normalized strain calculated by Eq. 18.

$$\varepsilon_n = \frac{\varepsilon - \varepsilon_{sh}}{\varepsilon_u - \varepsilon_{sh}} \quad \text{for} \quad \varepsilon_{sh} \leq \varepsilon \leq \varepsilon_u \tag{18}$$

The model parameters for the residual test are predicted as a function of T based on the statistical study on the experimental data. Two types of predictive equations exist. The first type uses basic functions (e.g. polynomial, power function, etc.) to predict the required parameters, for example, which was adopted in [26,28,31–33]. The second type uses an unified function of T (e.g. Eq. 8 to 11) and the numerical coefficients of the function are calibrated for each parameter, for example, which was adopted in [29].

3. Experimental stress-strain curves

An experimental study [11,12] was carried out in the Multi-Hazard Resilient Structures Lab at Johns Hopkins University to understand the stress-strain behaviors and the material properties of AHSS under various elevated temperature scenarios and provide an experimental benchmark for modeling. The study includes both AHSS properties at elevated temperatures (steady-state and transient-state test protocols) and after cooling down (residual test protocol), representing the post-fire scenario.

Specimens for the tensile coupon test were cut from two dual phase steel (DP) sheets and two martensitic steel (MS) sheets. In addition, specimens cut from a high-strength low-alloy steel (HSLA) sheet were also studied for the steady-state tests for comparison purpose. The nominal properties for the AHSS sheets are shown in Table 1. The steel sheets were labeled by their steel family and the nominal yield strength. Details of the experimental test series and results are explained in the

Table 1
Nominal properties of AHSS sheets.

Steel	t (mm)	σ_y (MPa)	σ_u (MPa)
DP-340	1.4	340	590
DP-700	1.4	700	980
MS-1030	1.0	1030	1300
MS-1200	1.0	1200	1500
HSLA-700	0.6	700	980

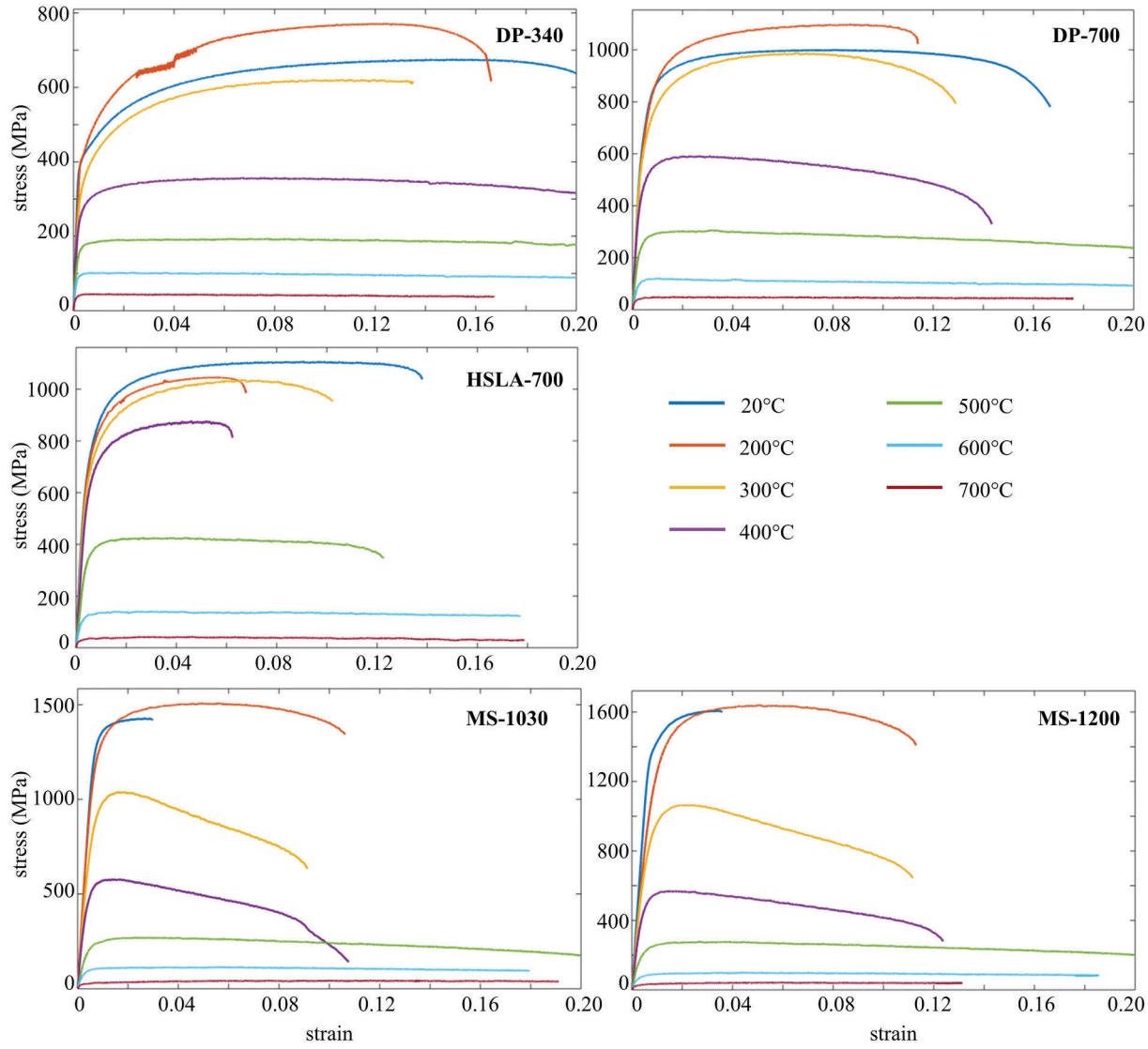

Fig. 1. Representative stress-strain relationships for steels at elevated temperatures from steady-state tests as reported in [11].

related published work [11,12]. Only the resulting stress-strain curves reported in [11,12] are shown herein as they are necessary to develop the models and derive the modeling parameters.

For steady-state test, DP-340, DP-700, MS-1030, MS-1200, and HSLA-700 were tested at each elevated temperature, which includes 20°C (ambient), 200 °C, 300 °C, 400 °C, 500 °C, 600 °C, and 700 °C. The experimental stress-strain curves are shown in Fig. 1. For all tests, no distinct yield point or yield plateau is observed; instead, the strain hardening process was gradually developed. Overall trends are visible regarding the change in key material properties, including yield and ultimate strengths, total elongation, and overall stress-strain behaviors at various temperatures. In general, the stress-strain curve's shape varies with the test temperature, and one material may show changes in the stress-strain relationship across temperature ranges. It should be noted that some strain hardening regions are very gradual and therefore may appear as a plateau. Overall, the strength decreases as the temperature increases after an initial strength increase at 200 °C, except for HSLA.

For the transient-state test, DP-700 and MS-1200 were studied to compare and supplement corresponding steady-state test results. The converted stress-strain curves are shown in Fig. 2. Each transient-state test can provide only one data point for each preselected temperature. Due to the limited number of tests, the transient-state test's stress-strain curves comprise limited data points.

For the residual test, the postfire material properties for DP-340, DP-700, MS-1030, and MS-1200 cooling down from up to 700 °C were studied. The experimental stress-strain relationships for the residual tests are shown in Fig. 3. Both Mode 1 and Mode 2 stress-strain behaviors are observed. For example, for DP-700, the ambient and 200 °C cases show Mode 1 behavior, while cases from 300 °C to 600 °C show Mode 2 behavior; interestingly, the case at 700 °C reverts to Mode 1 behavior. The intense strain hardening process for DP-340 at all test temperatures is observed, which can be evaluated by its high σ_u/σ_y ratio (from 1.17 to 1.26 after cooling down from different test temperatures). All high-temperature tests have a larger elongation at fracture than the case at ambient.

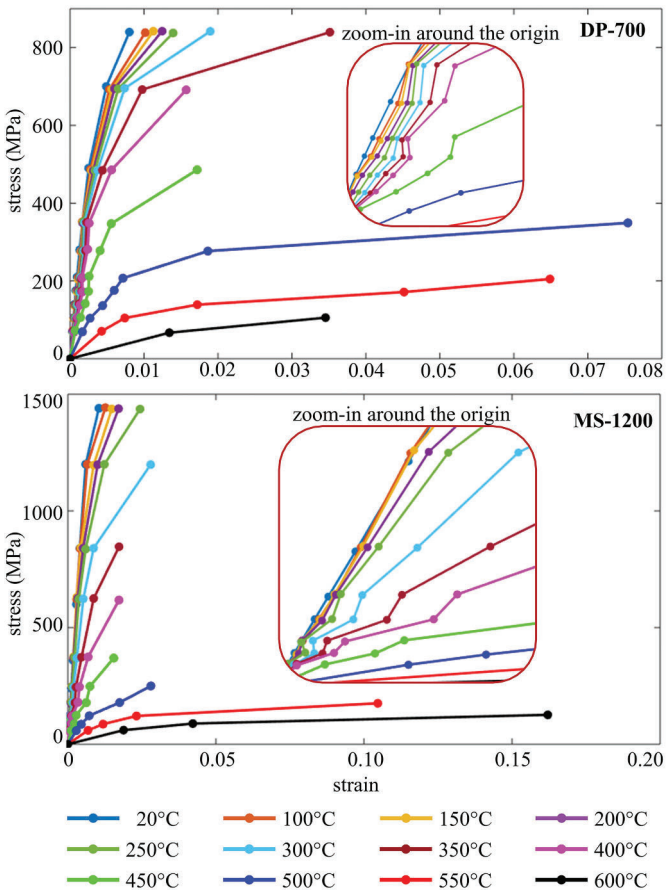

Fig. 2. Stress-strain relationships for DP-700 and MS-1200 at elevated temperatures from transient-state tests as reported in [11].

4. Optimal fit between AHSS stress-strain curves and existing models

Existing models are adopted to fit the AHSS experimental stress-strain curves. From the discussion on the experimental stress-strain relationships of AHSS at elevated temperature and after cooling down (Section 3), two different yielding modes of stress-strain behaviors are observed. R-O models are adopted to fit stress-strain curves with Mode 1 behavior. The four-stage model [39] and the bilinear plus nonlinear hardening model [43] are adopted to fit stress-strain curves with Mode 2 behavior, even if the bilinear plus nonlinear hardening model is not originally designed for high-temperature tests.

The material-property parameters are directly captured from the experimental curves to obtain the mathematically optimal fit between the existing models and the AHSS test data, instead of using predictive equations in literature. The numerical parameters (e.g., n, m, and K_1 to K_4) are calculated using the error minimization method to search the maximum R^2 by iterating the parameters. Error minimization is a form of mathematical regression analysis aiming for determining the optimal fit for specific data by searching for the parameters with minimum error of selected indicator. Common fit error indicator includes R^2, residual sum of squares (RSS), etc. RSS has intrinsic limitations [44], for example, its scale is largely dependent on the data scale. Oppositely, R^2 is a generalized parameter, and it is independent of the data scale, therefore it is appropriate in evaluating model fit for multiple groups of data [45–48]. For the stress-input models (e.g. R-O models), R^2 is calculated by Eq. 19; while for the strain-input models (e.g. the four-stage model [39] and the bilinear plus nonlinear hardening model [43]), R^2 is calculated by Eq. 20:

$$R^2 = 1 - \frac{SS_{res}}{SS_{tot}} = 1 - \frac{\sum_i (\varepsilon_{Ti} - \varepsilon_T(\sigma_{Ti}))^2}{\sum_i (\varepsilon_{Ti} - \bar{\varepsilon}_{Ti})^2} \tag{19}$$

$$R^2 = 1 - \frac{SS_{res}}{SS_{tot}} = 1 - \frac{\sum_i (\sigma_{Ti} - \sigma_T(\varepsilon_{Ti}))^2}{\sum_i (\sigma_{Ti} - \bar{\sigma}_{Ti})^2} \tag{20}$$

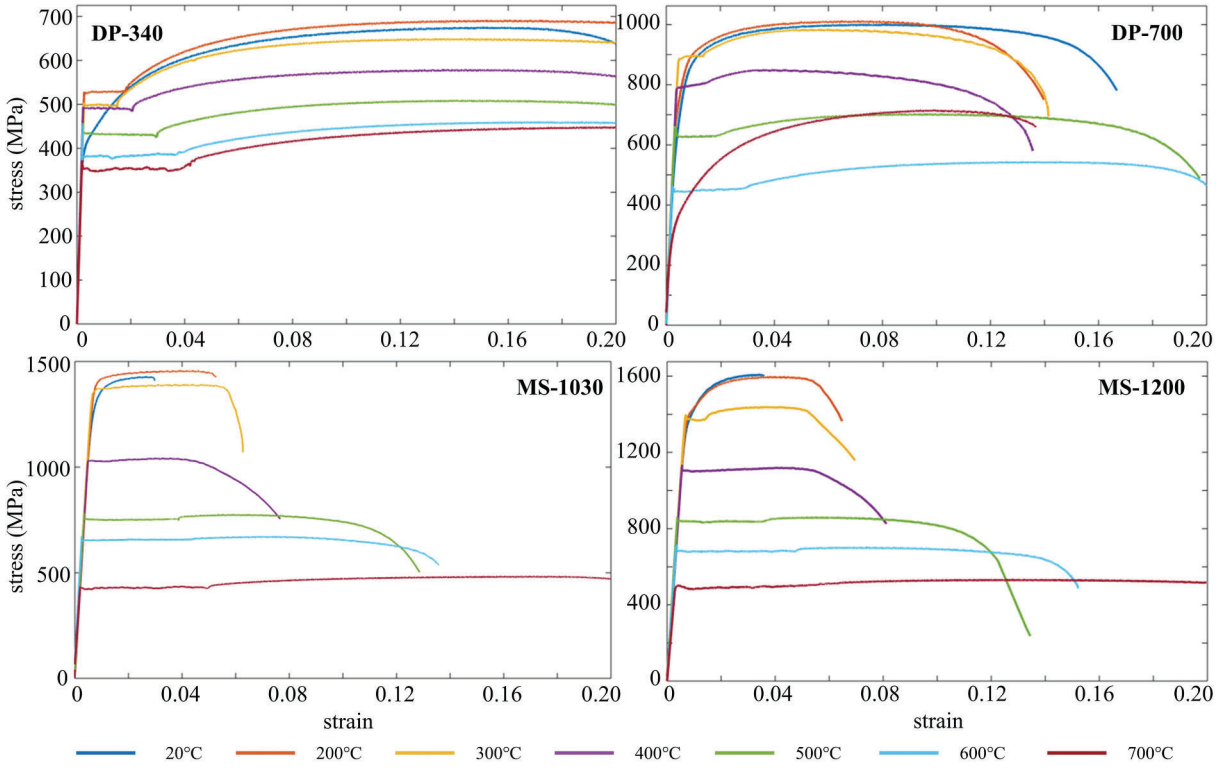

Fig. 3. Stress-strain relationships from residual tests for steels after cooling down from elevated temperature as reported in [12].

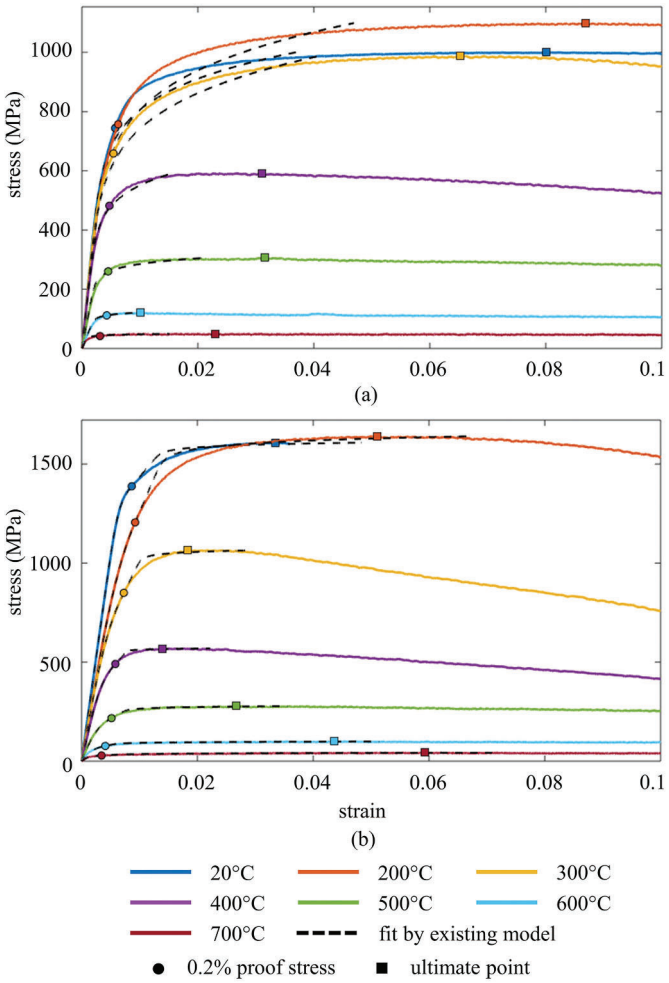

Fig. 4. Optimal fit examples for (a) DP-700 using representative one-stage R-O model [10] and (b) MS-1200 using representative two-stage model [18].

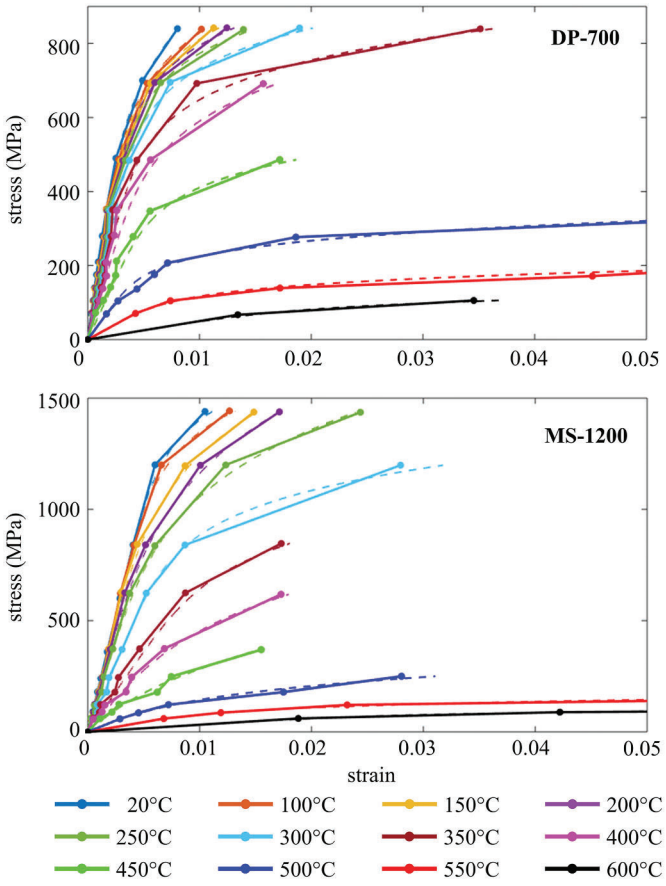

Fig. 5. Comparison between experimental stress-strain curves (solid lines) from transient-state tests and fit (dashed line) by one-stage R-O model [14] built by parameters from the tests.

where σ_{Ti} and ε_{Ti} are the stress and strain of data point i of the experimental curve of temperature T, $\varepsilon_T(\sigma_{Ti})$ is the model strain output calculated by σ_{Ti}, $\sigma_T(\varepsilon_{Ti})$ is the model stress output calculated by ε_{Ti}, $\bar{\varepsilon}_{Ti}$ is the average of the experimental strains, $\bar{\sigma}_{Ti}$ is the average of the experimental stresses.

For the stress-input models, R^2 is calculated from the difference between the test strain and the model strain, not the stress difference. Therefore, for R-O models at a high strain range, R^2 can be small (i.e., poor fit) even if the difference between the test curve and the model is not obvious visually. This illusion's key reason is that the horizontal axis parameter is typically the independent variable, and the vertical axis parameter is typically the dependent variable. While for the R-O models, the inverse situation occurs.

For steady-state tests, the optimal fit using the existing one-stage (DP-700) and two-stage (MS-1200) R-O models are shown in Fig. 4 as a sample of results. All R-O models depict the σ-ε relationship between the origin and the ultimate strength. Discrepancies in the shape of the stress-strain curves between existing models and test data are observed across temperatures. The average R^2 varies from 0.91 to 0.93 for one-stage R-O models and from 0.94 to 0.96 for two-stage R-O models, respectively. From the fit results, the existing one-stage and two-stage R-O models might not accurately predict the AHSS σ-ε behavior from steady-state tests. Similar levels of agreement are found when adopting the existing R-O models on the AHSS σ-ε curves from residual tests with Mode 1 behavior. Therefore, a new constitutive model must be proposed.

The σ-ε curves in transient-state tests are fitted using one-stage R-O models only. The reason is the test curves do not pass through the ultimate point and terminate at a relatively small strain level; thus, some parameters (e.g., ε_u, σ_u, and m) are not applicable for the two-stage models. By comparing the fits using existing one-stage R-O models, Chen and Ye's model [14] can provide accurate fits for both DP-700 and MS-1200 at all test temperatures, Olawale's model [35] generally provides accurate fits for both AHSS with a few exceptions at various temperatures. Other one-stage R-O models might not fit either DP-700 or MS-1200. Based on the fit results, Chen and Ye's model [14] (Eq. 21) is recommended and adopted in this paper for fits of the transient-state results, and the optimal fits are shown in Fig. 5.

$$\varepsilon_T = \frac{\sigma_T}{E_T} + 0.002\left(\frac{\sigma_T}{\sigma_{yT}}\right)^n \quad \text{for} \quad 0 \le \sigma_T \le \sigma_{uT} \tag{21}$$

The σ-ε curves from residual tests with Mode 2 behavior are fitted using the four-stage model [39] and the bilinear plus nonlinear hardening model [43]. The four-stage model [39] can accurately fit all DP-700 and MS-1200 σ-ε curves, and a few MS-1030 σ-ε curves. However, the fits with all DP-340 σ-ε curves and MS-1030 σ-ε curves up to 500 °C are inaccurate. The average R^2 is 0.76, and the minimum R^2 is 0.69. For the bilinear plus nonlinear hardening model, the four coefficients K_1 to K_4 are recommended as 0.4, 2, 400, and 5 respectively based on the statistical study of the HRS database [43]. The fits are inaccurate by adopting these recommended coefficients for the AHSS residual test data, particularly the MS steel. The average R^2 is 0.71, and the minimum R^2 is 0.32. However, by iterating the four coefficients K_1 to K_4 for each residual test σ-ε curve using the error minimization method, the average R^2 can be as high as 0.99, and the minimum R^2 is 0.97, which

significantly increases the fit accuracy. Unfortunately, the calibrated coefficients do not show any clear trend along with temperature change. Therefore it is difficult to provide continuous prediction on these coefficients as a function of T. The improvement indicates the bilinear plus nonlinear hardening model can accurately fit the AHSS residual test σ-ε curves, but the coefficient recommendation must be updated.

5. Proposed stress-strain models

The discussion in Section 4 revealed that existing models cannot accurately fit the AHSS test curves from the steady-state tests and the residual tests, while one existing one-stage R-O model [14] can fit the AHSS test curves from the transient-state tests. Observed post-yield inaccuracies might have consequences for predictions of structural behavior, for example, in scenarios of blast crushing, collapse, and other cases where the relationship between local strain and engineering strain is crucial [49]. Therefore, in this section, a new model, updated from existing two-stage R-O models and initially designed for the modeling of AHSS stress-strain relationship at ambient [50], is proposed for the steady-state tests and residual tests with Mode 1 behavior. Besides, an updated model with calibrated numerical coefficients based on the bilinear plus nonlinear hardening model [43] is proposed for the residual tests with Mode 2 behavior.

5.1. Updated model for mode 1 stress-strain behavior

As shown in Fig. 6, a two-stage plus linear model is proposed to fit high-temperature tests with Mode 1 behavior. Like other R-O models, the proposed model uses stress at elevated temperature, σ_T, as the model input, and the model output is the corresponding strain prediction, ε_T. The model describes the AHSS stress-strain behavior in high-temperature tests from the origin to the ultimate point. The model consists of two nonlinear stages plus a linear part. The first stage ranges from the origin to the *offset point*, which is defined as the point with a plastic strain, p. Its strain is ε_{pT} and its stress is σ_{pT}. The second stage ranges from the *offset point* to the *equivalent ultimate point*. The *equivalent ultimate point* is defined as the point with a stress equal to 99% of σ_{uT} ($\sigma_{euT} = 0.99\sigma_{uT}$) and a strain of ε_{euT} within the strain hardening region (i.e. $\varepsilon_{euT} < \varepsilon_{uT}$). The final part is proposed as a line between the equivalent ultimate point and the ultimate point. The model expression is given by Eq. 22.

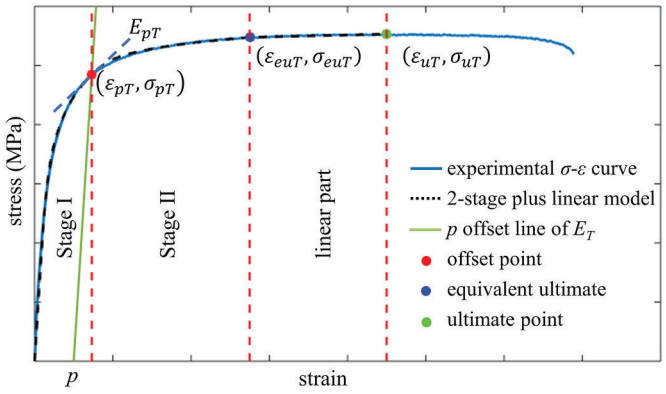

Fig. 6. Schematic diagram for the proposed two-stage plus linear model.

Table 2
Recommendation of p value in percentage for the proposed two-stage plus linear model based on steel strength and test temperature.

Steel	DP-340	DP-700	HSLA-700	MS-1030	MS-1200
$T < 400$°C	2.0%	1.0%	1.0%	0.5%	0.5%
$T \geq 400$°C	0.2%	0.2%	0.2%	0.2%	0.2%

contains three updates. Firstly, the model mathematically passes through the origin (0,0), the offset point (σ_{pT}, ε_{pT}), and the equivalent ultimate point (σ_{euT}, ε_{euT}), regardless the specific values of the required parameters of the model. This characteristic guarantees that the model has continuous transitions between every adjacent stage.

Secondly, the plastic strain of the offset point changes from 0.002 to a new value p. The offset point in existing two-stage R-O models was defined as the point with a plastic strain of 0.002. However, this practice does not provide an accurate fit between the model and the AHSS experimental stress-strain curves across all elevated temperatures, because AHSS stress-strain curves show significant nonlinearity. The fit was optimized by varying p from 0.002 to 0.020 at 0.001 increments and iterating n and m to search for the maximum R^2 between the test curve and the model. From the optimization results, the recommendations of p for the various AHSS at different elevated temperature ranges are listed in Table 2, where a clear decreasing trend of p with increasing grade strength is observed.

$$\varepsilon_T = \begin{cases} \dfrac{\sigma_T}{E_T} + p\left(\dfrac{\sigma_T}{\sigma_{pT}}\right)^n & \text{for } 0 \leq \sigma_T \leq \sigma_{pT} \\ \dfrac{\sigma_T - \sigma_{pT}}{E_{pT}} + \left(\varepsilon_{euT} - \varepsilon_{pT} - \dfrac{\sigma_{euT} - \sigma_{pT}}{E_{pT}}\right)\left(\dfrac{\sigma_T - \sigma_{pT}}{\sigma_{euT} - \sigma_{pT}}\right)^m + \varepsilon_{pT} & \text{for } \sigma_{pT} < \sigma_T \leq \sigma_{euT} \\ \dfrac{\varepsilon_{uT} - \varepsilon_{euT}}{\sigma_{uT} - \sigma_{euT}}\cdot(\sigma_T - \sigma_{euT}) + \varepsilon_{euT} & \text{for } \sigma_{euT} < \sigma_T \leq \sigma_{uT} \end{cases} \tag{22}$$

where n and m are the exponential coefficients determining the fit's degree of curvature for the first stage and the second stage respectively, E_{pT} is the tangent modulus at σ_{pT} and it is calculated by Eq. 23.

$$\frac{1}{E_{pT}} = \frac{\partial \varepsilon_T(\sigma_T)}{\partial \sigma_T}\bigg|_{\sigma_T=\sigma_{pT}} = \frac{1 + pn\frac{\sigma_T^{n-1}}{\sigma_{pT}^n}E_T}{E_T}\bigg|_{\sigma_T=\sigma_{pT}} = \frac{1 + pn\frac{E_T}{\sigma_{pT}}}{E_T} \Rightarrow E_{pT} = \frac{E_T}{1 + pn\frac{E_T}{\sigma_{pT}}} \tag{23}$$

Compared with existing two-stage models designed for the high-temperature scenario, the proposed two-stage plus linear model

The third update is the change of the end of the second stage from the ultimate point to the equivalent ultimate point, while the remainder of the stress-strain curve (from the equivalent ultimate point to the ultimate point) is described as a line. Compared with other steels with a gradual yielding process (for example, stainless steel), AHSS σ-ε curves have a relatively long strain hardening process with a small stress increase. For example, when σ_T increases from the equivalent ultimate stress σ_{euT} to the ultimate strength σ_{uT}, where stress only increases 1%, ε_T increases on average 100% for DP-340, 51% for DP-700, 67% for HSLA-700, 52% for MS-1030, and 25% for MS-1200. Including this long, flat strain hardening part in the second stage model distorts the curve with an excessively large exponential coefficient m. Therefore, in the

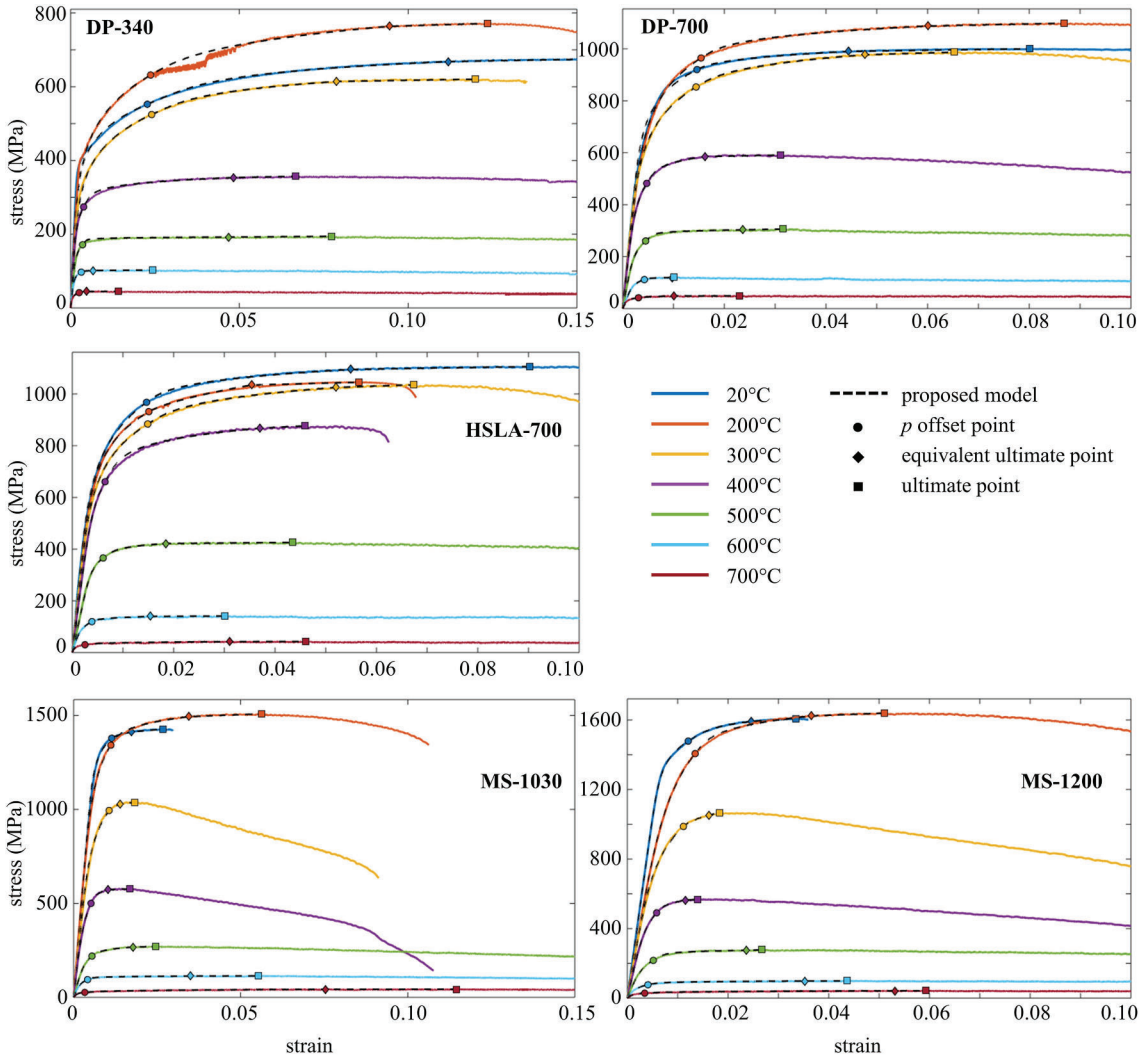

Fig. 7. Comparison between the stress-strain curves from steady-state tests and fit by the proposed two-stage plus linear model built by test results.

proposed model, the second stage ends at the equivalent ultimate point, and a line represents the remainder of the curve to the ultimate point.

The fit of AHSS σ-ε curves at different temperatures from steady-state tests using the proposed model (Eq. 22) and the recommended p value (Table 2) is shown in Fig. 7. The average and minimum R^2 for each AHSS specimen is no less than 0.995 and 0.983, respectively. From the observation on model fit results, the discrepancy between the test data and the stress-input model fit (e.g., R-O models) is negligible when $R^2 \geq$ 0.96 Compared with the fit of AHSS curves using existing models (Section 4), the proposed model significantly increases the fit accuracy.

5.2. Updated model for mode 2 stress-strain behavior

An updated model based on the bilinear plus nonlinear hardening model [43] is proposed for AHSS σ-ε curves from Mode 2 residual tests as shown in Eq. 24. The bilinear regions (elastic and yield plateau) are the same as presented in [43]; the expression for the nonlinear hardening is updated.

$$\sigma_T = \begin{cases} E_T \varepsilon_T & \text{for } 0 \leq \varepsilon_T \leq \varepsilon_{yT} \\ \sigma_{yT} & \text{for } \varepsilon_{yT} < \varepsilon_T \leq \varepsilon_{shT} \\ \sigma_{yT} + (\sigma_{uT} - \sigma_{yT}) \left[K_1 \varepsilon_{nT} + \dfrac{K_2 \varepsilon_{nT}}{(1 + K_3 \varepsilon_{nT})} \right] & \text{for } 0 \leq \varepsilon_{nT} \leq 1 \end{cases} \tag{24}$$

where ε_{nT} is normalized strain calculated by Eq. 25.

$$\varepsilon_{nT} = \frac{\varepsilon_T - \varepsilon_{shT}}{\varepsilon_{uT} - \varepsilon_{shT}} \quad \text{for } \varepsilon_{shT} \leq \varepsilon_T \leq \varepsilon_{uT} \tag{25}$$

The nonlinear hardening part of Eq. 24 is a nonlinear interpolation between ε_{yT} and ε_{uT} based on the input strain ε_T. The curve nonlinearity degree is defined by four coefficients (K_1 to K_4) in [43], while it is defined by three coefficients (K_1 to K_3) in the proposed expression by adopting $K_4 = 1$. By iterating K_1 to K_3 using error minimization to search for the maximum average R^2 of the fit between the updated model and the test curves, it is recommended to adopt $K_1 = 0.029$, $K_2 = 4.713$, and $K_3 = 3.855$ for AHSS residual test stress-strain curves with Mode 2 behavior, which provides an average R^2 of 0.983. For Mode 2 behavior

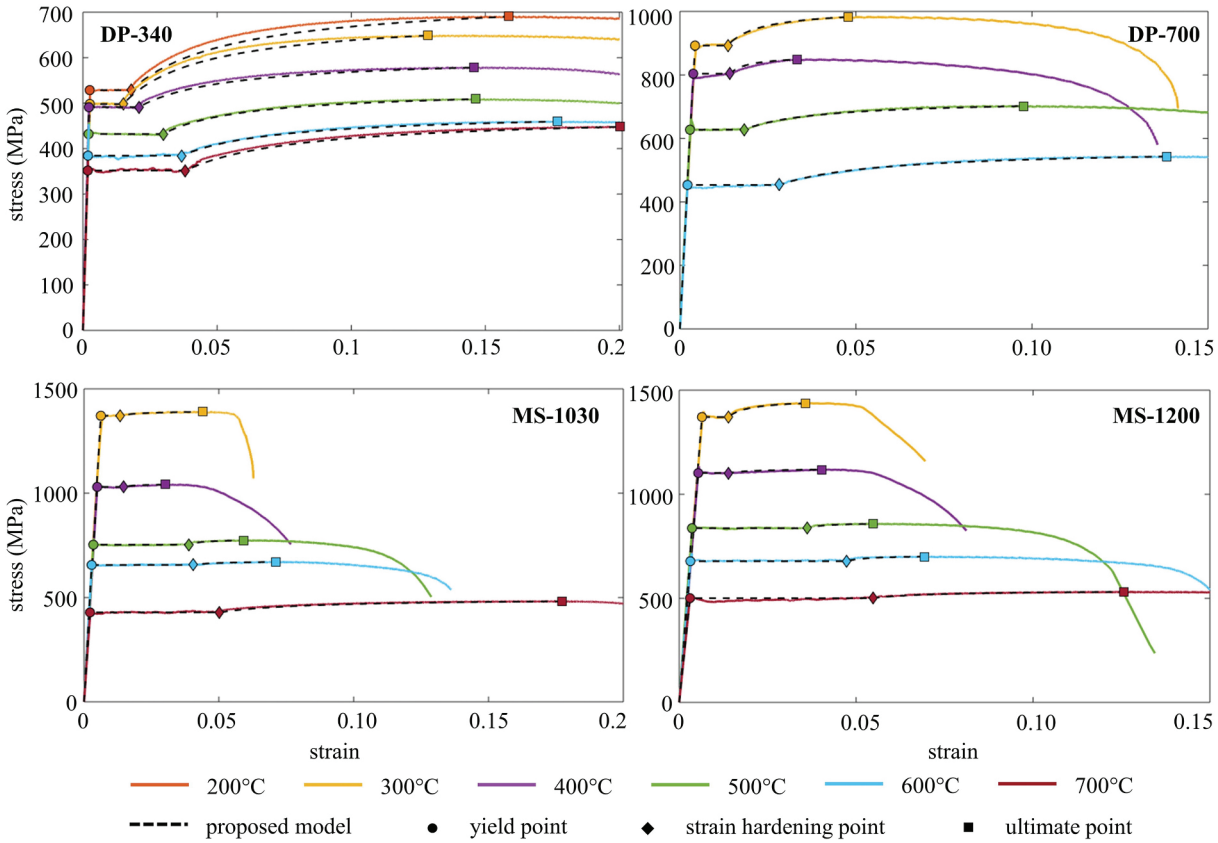

Fig. 8. Comparison between the sharp mode stress–strain curves from residual tests and fit by the modified three-parameter bilinear plus nonlinear hardening model built by test results and recommended model coefficients.

cases using strain-input model (e.g., the bilinear plus nonlinear hardening model), it is found that an excellent agreement is achieved for the curve fit when $R^2 \geq 0.95$. The fits between the test curves and the updated model built by the recommended coefficients are shown in Fig. 8.

5.3. Fit between proposed stress-strain models and existing data

The proposed models show excellent fit between AHSS stress-strain data captured from both elevated temperature and post-fire experiments as discussed in Section 5.1 and 5.2. It is investigated whether the proposed models will accurately capture the stress-strain behavior of other steel grades with similar stress-strain behaviors.

Stress-strain curves from [51] were selected where the post-fire material properties of very high strength steel S960 was studied. The stress-strain curves show Mode 2 behavior between ambient (20 °C) and 750 °C and Mode 1 behavior from 800 °C to 1000 °C. Therefore, both proposed models can be verified by using a group of data from the same experiment campaign.

A few representative curves were selected for the fit following the identical procedures as described in Section 5.1 and 5.2. For Mode 1, stress-strain curves cooling down from 800 °C, 900 °C, and 1000 °C were selected. Noticeably, the selected Mode 1 postfire curves do not show as significant strength deterioration as the AHSS elevated temperature curves at 400 °C or above. Therefore, $p = 0.005$, which is recommended for very high strength steel (e.g., MS-1030 and MS-1200) at lower temperature range, was adopted in the Mode 1 curve fit. For Mode 2, stress-strain curves cooling down from 500 °C and 700 °C were selected. The numerical coefficients recommended for AHSS post-fire Mode 2 curves in Section 5.2 were applied, where $K_1 = 0.029$, $K_2 = 4.713$, and $K_3 = 3.855$. The optimal fits between the selected experimental curves and corresponding models are shown in Fig 9.

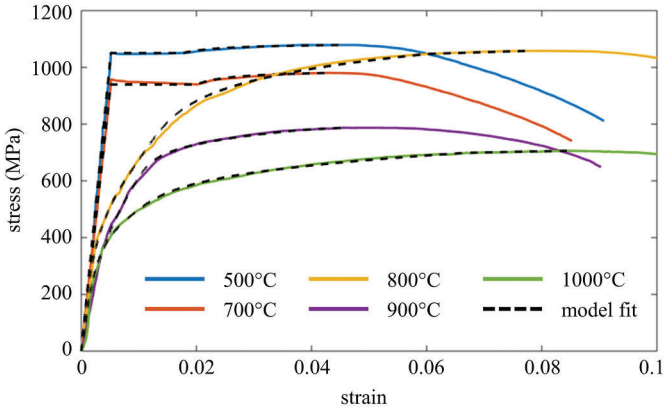

Fig. 9. Comparison between the representative experimental stress-strain curves from [51] and the corresponding fit by the proposed models.

The fit results show excellent agreement with the test data selected from [5]. Specifically, R^2 for the 800 °C, 900 °C, and 1000 °C postfire curve fits using the updated two-stage plus linear model is above 0.995 with an average of 0.997; R^2 for the 500 °C and 700 °C postfire curve fits using the updated bilinear plus nonlinear hardening model is above 0.96 with an average of 0.965. The excellent fit agreement illustrates the potential for the adoption of the proposed models for other grades with similar stress-strain behaviors.

6. Predictive equations and recommendations for model parameters

The proposed stress-strain models for steady-state tests, transient-state tests, and residual tests are discussed in Section 5. To define the constitutive relationships using the proposed models, accurate prediction of the required parameters is necessary.

A unified equation proposed by the authors [52], as shown in Eq. 26, is adopted in this study to fit the retention factors for the required material-property parameters:

$$R_{X_{Tnor}} = c + (1-c)\frac{1 - T_{nor}^{b}}{1 + aT_{nor}^{b}} \tag{26}$$

where T_{nor} is the normalized temperature normalized by T_{max} and T_{min} as defined in Eq. 27, T_{max} is the maximum temperature of the test series, T_{min} is the minimum temperature of the test series. The derivative of $R_{X_{Tnor}}$ in Eq. 26 is calculated in Eq. 28.

$$T_{nor} = \frac{T - T_{min}}{T_{max} - T_{min}} \tag{27}$$

$$\frac{\partial R_{X_{Tnor}}}{\partial T_{nor}} = (1-c)\frac{-bT_{nor}^{b-1}(a+1)}{\left(1 + aT_{nor}^{b}\right)^{2}} \tag{28}$$

From Eq. 28, $R_{X_{Tnor}}$ is always monotonic regardless of the values of a, b, and c; $R_{X_{Tnor}}$ is monotonic decreasing when $a > -1$, b is positive, and $c < 1$. This characteristic makes Eq. 26 suitable in describing the deterioration of steel material properties, particularly for elastic modulus, proof stresses, and ultimate strength, with temperature increase as observed in experiments.

6.1. Steady-state tests

For modeling of the stress-strain curves from the steady-state tests, the proposed two-stage plus linear model (Eq. 22) passes through the p offset point (values in Table 2), the equivalent ultimate point, and the ultimate point. The following parameters are required to define the model: the elastic modulus E_T, the p proof stress σ_{pT} and its strain ε_{pT}, the stress and strain of the equivalent ultimate point σ_{euT} and ε_{euT}, the ultimate strength σ_{uT}, and the ultimate strain ε_{uT}. Among these parameters, two pairs are related by definition: $\varepsilon_{pT} = \sigma_{pT}/E_T + p$ and $\sigma_{euT} = 0.99\sigma_{uT}$. In addition, two exponential coefficients n and m are also required to describe the nonlinearity of the first and the second stage model respectively.

In general, the elastic modulus is determined from the stress-strain curve as the slope of its initial linear portion. For Mode 1 behavior (rounded curve without a distinct yield point), the linear portion is less obvious. The method from Huang and Young [53] is adopted where the slope of the linear regression for all data between 20% and 45% of nominal yield strength is regarded as the elastic modulus. An update is made to adopt this method for high-temperature tests to include the deterioration from a high-temperature environment. The update is to proportion the nominal yield strength at ambient, σ_{ny0}, by the deterioration of the experimental ultimate strength as calculated by Eq. 29:

$$\sigma_{nyT} = \sigma_{ny0} \times \frac{\sigma_{uT}}{\sigma_{u0}} \tag{29}$$

where σ_{ny} is the nominal yield strength, subscript 0 represents ambient, and subscript T represents an elevated temperature.

Parameters for the steady-state tests are shown in Table 3, including E_T, σ_{pT}, σ_{uT}, ε_{euT}, ε_{uT}, n and m. The test data is used as benchmark to develop the predictive equations for the retention factor of the parameters required by the proposed model. The calibrated coefficients of the unified equation for these parameters are shown in Table 4.

Table 3
Properties required by the proposed two-stage plus linear model (Eq. 22) from AHSS steady-state test results.

T (°C)	DP-340	DP-700	HSLA-700	MS-1030	MS-1200	DP-340	DP-700	HSLA-700	MS-1030	MS-1200
	E_T (GPa)									
20	202.2	203.3	208.1	216.0	207.9					
200	170.0	177.9	182.4	218.2	166.3					
300	131.1	192.5	181.9	177.1	167.5					
400	146.4	160.3	151.2	156.5	129.0					
500	110.6	103.0	89.3	62.8	68.6					
600	82.6	48.6	63.7	43.1	36.5					
700	76.0	38.0	55.4	18.5	19.7					
	σ_{pT} (MPa)					σ_{uT} (MPa)				
20	552.5	944.4	967.9	1379.3	1466.5	675.0	1025.6	1106.3	1427.6	1594.8
200	631.7	964.8	931.8	1342.4	1406.5	771.7	1099.0	1045.4	1509.3	1639.8
300	524.5	838.0	895.4	994.5	997.5	620.4	972.1	1053.0	1038.4	1073.9
400	274.0	483.1	634.8	499.9	490.5	357.2	590.8	835.1	577.7	565.9
500	171.4	260.3	365.7	219.6	217.0	194.3	306.2	425.9	270.6	277.8
600	97.1	111.7	119.5	94.3	76.5	102.9	120.7	141.3	114.5	99.5
700	41.6	41.7	30.1	26.2	28.5	45.2	49.2	42.9	43.2	42.5
	ε_{euT}					ε_{uT}				
20	0.112	0.045	0.055	0.017	0.026	0.154	0.075	0.090	0.027	0.036
200	0.094	0.060	0.035	0.035	0.036	0.123	0.087	0.056	0.056	0.051
300	0.079	0.047	0.056	0.014	0.016	0.120	0.063	0.073	0.018	0.020
400	0.048	0.017	0.034	0.010	0.012	0.067	0.026	0.045	0.017	0.015
500	0.047	0.024	0.018	0.018	0.024	0.077	0.032	0.044	0.025	0.027
600	0.007	0.010	0.015	0.035	0.035	0.024	0.010	0.030	0.055	0.044
700	0.005	0.010	0.031	0.075	0.053	0.014	0.023	0.046	0.115	0.059
	n					m				
20	7.1	8.8	6.2	15.2	15.8	4.2	2.9	3.2	1.9	4.5
200	5.8	7.0	7.4	7.8	5.8	3.0	3.3	1.8	3.4	3.7
300	6.0	6.7	6.7	6.7	5.6	3.7	3.1	3.3	2.3	2.2
400	7.2	6.3	7.0	4.6	5.3	5.1	4.3	4.4	3.9	3.2
500	7.1	6.3	10.5	5.5	4.9	11.1	8.2	4.5	3.3	7.9
600	9.0	7.6	4.9	5.1	5.0	4.0	5.7	3.2	6.4	5.4
700	5.6	7.6	4.2	7.6	7.6	4.0	3.3	3.4	3.4	3.8

Table 4
Proposed coefficients for the unified predictive equation (Eq. 26) of material property parameters required by the two-stage plus linear model for the steady-state tests.

steel	T (°C)	a	b	c	T (°C)	a	b	c
	E_T							
DP-340	[20, 700]	0.53	1.16	0.37				
DP-700	[20, 700]	3.50	4.08	0.15				
HSLA-700	[20, 700]	6.51	4.11	0.24				
MS-1030	[20, 700]	10.00	4.99	0.08				
MS-1200	[20, 700]	1.17	2.15	0.06				
	σ_{pT}				σ_{uT}			
DP-340	[20, 700]	48.00	6.64	0.12	[20, 700]	30.85	6.12	0.09
DP-700	[20, 700]	22.45	5.58	0.06	[20, 700]	25.53	6.25	0.06
HSLA-700	[20, 700]	8.22	5.07	0.02	[20, 700]	14.12	6.50	0.03
MS-1030	[20, 700]	30.26	4.94	0.03	[20, 700]	23.48	4.76	0.04
MS-1200	[20, 700]	29.91	4.73	0.02	[20, 700]	29.27	4.74	0.04
	ε_{euT}				ε_{uT}			
DP-340	[20, 700]	1.26	1.97	0.01	[20, 700]	0.91	1.76	0.07
DP-700	[20, 700]	5.72E+05	19.77	0.27	[20, 700]	215.39	7.50	0.17
HSLA-700	[20, 700]	0.00	0.72	0.25	[20, 700]	0.00	0.53	0.33
MS-1030	[20, 400]	5.08E+05	14.88	0.58	[20, 400]	3.57E+08	20.23	0.63
MS-1200	[20, 400]	1.10E+06	14.84	0.46	[20, 400]	1.96E+06	14.95	0.41

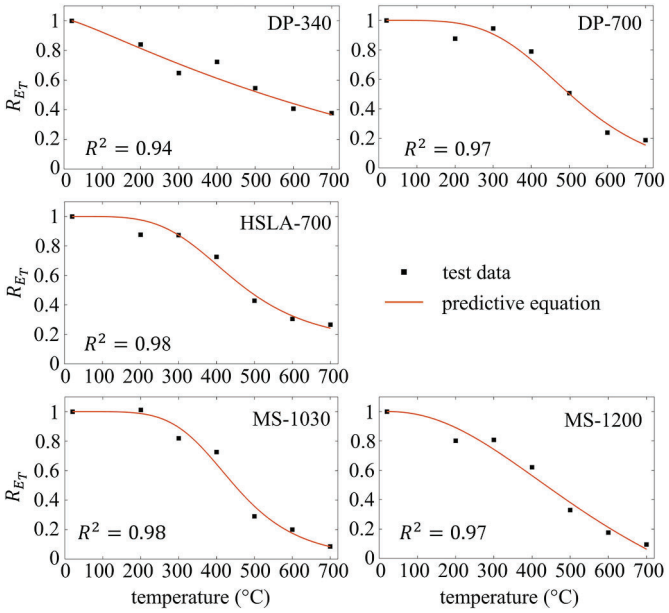

Fig. 10. Prediction of AHSS elastic modulus for steady-state tests by Eq. 26 using proposed coefficients.

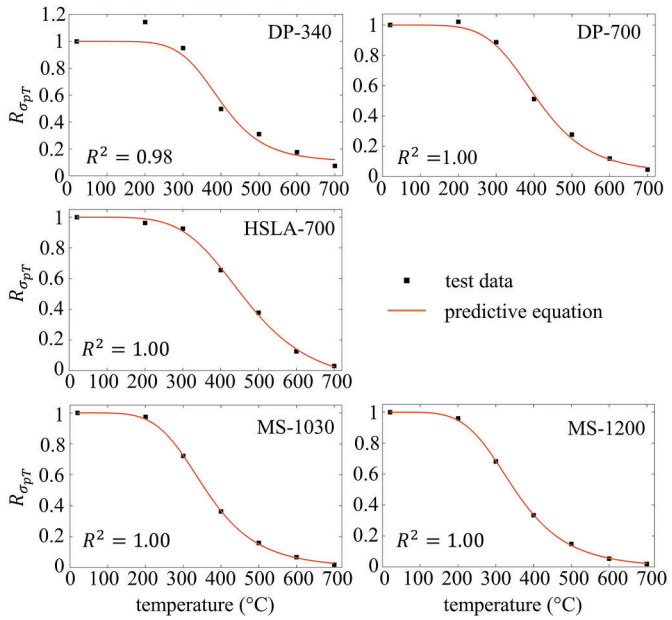

Fig. 11. Prediction of AHSS p proof stress for steady-state tests by Eq. 26 using proposed coefficients.

Relationships between the parameter retention factors and T are shown in Figs. 10 to 14.

For the strain parameters, ε_{euT} and ε_{uT} for MS steels above 400 °C show apparent increasing trends. Therefore, for these cases, it is difficult to predict the strains using the unified equation (Eq. 26) only. Instead, a combination of the unified equation and one basic function is used to build piecewise predictive equations if necessary. To lower the equation's complexity while guaranteeing the prediction accuracy, the basic functions to fit the aforementioned strain cases include exponential function (Eq. 30) and linear function (Eq. 31). The calibrated coefficients of the unified predictive equation (Eq. 26) for the strains are shown in Table 4. The calibrated coefficients of the basic functions (Eq. 30 and 31) are shown in Table 5. The fits of ε_{euT} and ε_{uT} between the predictive equation and experimental data are shown in Fig. 13 and Fig. 14.

$$R_{X_T} = ae^{bT} \tag{30}$$

$$R_{X_T} = aT + b \tag{31}$$

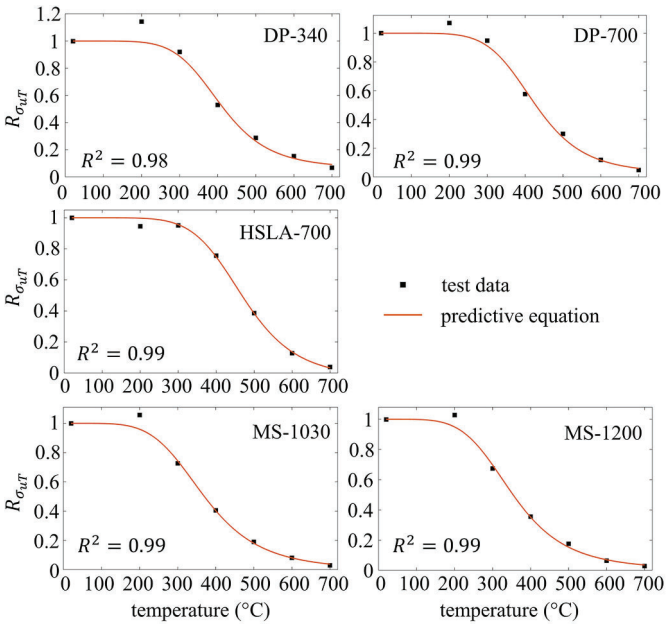

Fig. 12. Prediction of AHSS ultimate strength for steady-state tests by Eq. 26 using proposed coefficients.

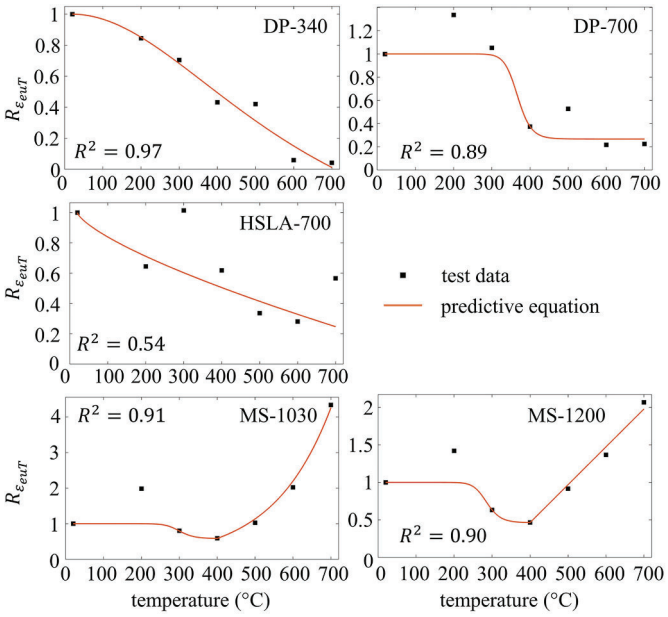

Fig. 13. Prediction for the strain of the equivalent ultimate point for steady-state tests.

6.2. Transient-state tests

For modeling the transient-state test results, Chen and Ye's model [14] is adopted. E_T, the 0.2% proof stress $\sigma_{0.2T}$, and the exponential coefficient n at the elevated temperature T are required to define the model. As discussed in Section 3, for the experimental stress-strain curves generated from the AHSS transient-state tests, the curves do not approach the ultimate point. Therefore σ_{uT} is not available, and Eq. 29 can not be adopted to calculate σ_{nyT} and E_T. Thus, a modification is made on Eq. 29 for transient-state tests. The ratio between $\sigma_{t0.5T}$ (the stress at $\varepsilon_T = 0.005$ at T) and $\sigma_{t0.5,0}$ (the stress at $\varepsilon = 0.005$ at ambient) is used to account for the deterioration of the nominal yield strength at T, as shown in Eq. 32.

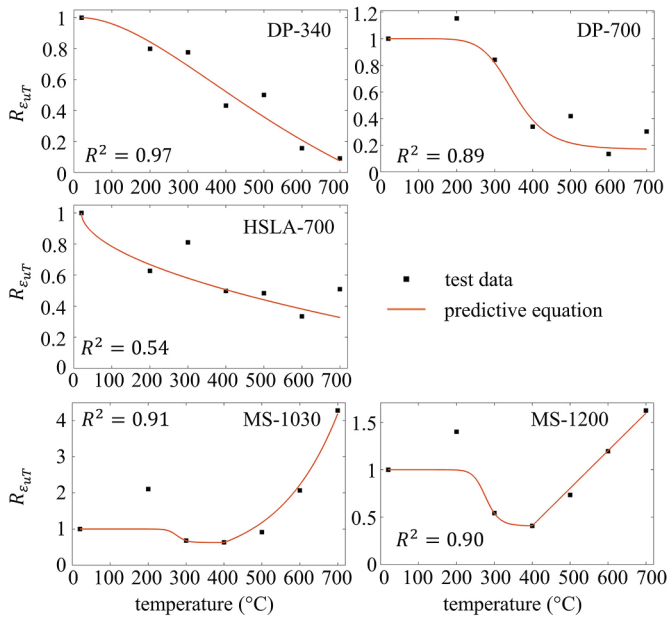

Fig. 14. Prediction for the ultimate strain for steady-state tests.

Table 5
Proposed coefficients for the basic equations of required strains for AHSS steady-state tests.

	T (°C)	form	a	b
Strain at equivalent ultimate point ε_{euT}				
MS-1030	(400, 700]	exp.	0.04	6.61E-03
MS-1200	(400, 700]	linear	5.05E-03	−1.56
ultimate strain ε_{uT}				
MS-1030	(400, 700]	exp.	0.05	6.34E-03
MS-1200	(400, 700]	linear	3.96E-03	−1.18

$$\sigma_{nyT} = \sigma_{ny0} \times \frac{\sigma_{t0.5T}}{\sigma_{t0.5,0}} \tag{32}$$

The parameters of the model for transient tests are listed in Table 6, including E_T, $\sigma_{0.2T}$, and n. The calibrated coefficients of the unified predictive equation (Eq. 26) for E_T and $\sigma_{0.2T}$ required by Chen and Ye's model [14] are shown in Table 7. The fits of the parameters between the proposed predictive equation and experimental values are shown in Fig 15 and Fig. 16.

Table 6
Properties required by the recommended one-stage model [14] from AHSS transient-state test results.

T (°C)	DP-700	MS-1200	DP-700	MS-1200	DP-700	MS-1200
	E_T (GPa)		$\sigma_{0.2T}$ (MPa)		n	
20	214.0	207.9	721.0	1327.2	4.8	9.1
100	190.4	206.9	703.8	1259.7	6.4	8.3
150	180.4	200.0	699.1	1095.2	6.8	5.1
200	164.9	185.7	700.2	1004.1	7.5	4.3
250	155.9	165.4	686.2	929.4	7.8	4.7
300	140.1	121.6	654.3	844.7	7.8	6.8
350	121.7	72.5	574.8	701.1	7.1	6.2
400	104.1	60.5	512.2	425.4	5.5	3.6
450	66.0	44.5	371.9	222.2	6.5	2.5
500	41.4	20.4	196.3	128.2	6.2	3.4
550	16.5	8.8	108.9	85.4	5.5	5.4
600	5.0	3.2	72.7	64.3	5.5	6.4

Table 7
Proposed coefficients for the predictive equation (Eq. 26) of elastic modulus and 0.2% proof stress required by the recommended one-stage R-O model ([14]) for transient-state test.

Steel	T (°C)	a	b	c
	E_T			
DP-700	[20, 600]	0.00	1.47	0.01
MS-1200	[20, 600]	13.14	4.12	0.01
	$\sigma_{0.2T}$			
DP-700	[20, 600]	6.13	6.51	0.07
MS-1200	[20, 600]	2.31	2.46	0.00

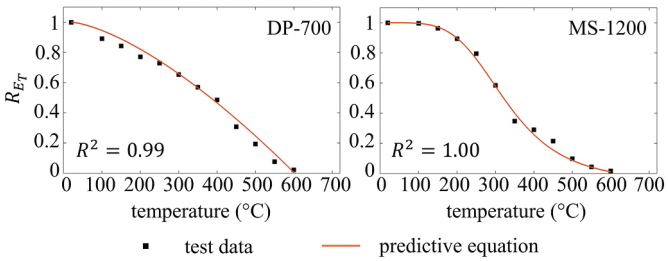

Fig. 15. Prediction of AHSS elastic modulus for transient-state tests by Eq. 26 using proposed coefficients.

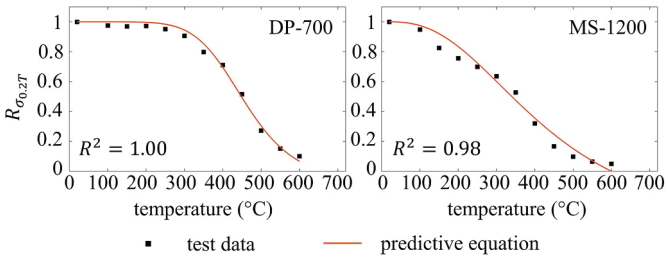

Fig. 16. Prediction of AHSS 0.2% proof stress for transient-state tests by Eq. 26 using proposed coefficients.

6.3. Residual tests

For the residual test, a small number of tests show Mode 1 (i.e. gradual yielding with a nonlinear curve shape) stress-strain behavior, and they are modeled by the two-stage plus linear model (Eq. 22). Mode 1 behavior is generally observed when the test temperature is lower than 200 °C. The only exception is DP-700 from the 700 °C test, which also shows Mode 1 behavior. Parameters E_T, σ_{pT}, σ_{uT}, ε_{euT}, ε_{uT}, n, and m are needed to adopt the proposed two-stage plus linear model (Eq. 22). The values of these parameters as shown in Table 8 are determined by following the same procedures as the steady-state tests described in Section 5.1. Note that E_T, σ_{uT}, and ε_{uT} are also required by the updated bilinear plus nonlinear hardening model for the residual tests with Mode 2 behavior. Therefore, they are discussed together next and are given in Table 9. Due to the limited number of tests observed with Mode 1 behavior, it is difficult to conclude any credible trend for the material properties.

Most post-fire stress-strain curves show Mode 2 behavior. They are modeled by the updated bilinear plus nonlinear hardening model (Eq. 12, 13, and 17). The model requires elastic modulus E_T, yield strength σ_{yT}, yield strain ε_{yT}, ε_{shT} (the strain at the end of the yield plateau and the onset of the nonlinear strain hardening), ultimate strength σ_{uT}, ultimate strain ε_{uT}, and three coefficients ($K1$ to $K3$ describing the nonlinearity of the strain hardening process). Among these parameters, E_T, σ_{yT}, and ε_{yT} are related as $\varepsilon_{yT} = \sigma_{yT}/E_T$, therefore when any two of the three parameters are known, the other parameter can be calculated. Considering both simplicity and accuracy, $K1$ to $K3$ are recommended as 0.029, 4.713, and 3.855 respectively by statistical study on the test curves using error minimization method as discussed in Section 5.2.

For Mode 1 post-fire stress-strain behaviors, E_T is calculated using the same method as the steady-state tests described in Section 6.1. For Mode 2 post-fire stress-strain behaviors, clear linear elastic behavior is observed up to the yield point. Therefore E_T is calculated as the slope of the linear portion. E_T for the residual tests is shown in Table 9, and the relationship between its retention factor R_{E_T} and T is shown in Fig. 17.

For residual tests showing Mode 2 behavior, σ_{yT} is the stress at the yield point, where the linear elastic region ends and the yield plateau begins. σ_{yT} is shown in Table 9, and the relationship between its retention factor $R_{\sigma_{yT}}$ and T is shown in Fig. 18. σ_{yT} shows a clear gradual decreasing trend when T increases; σ_{yT} of DP-700, MS-1030, and MS-1200 have similar deterioration rates, while σ_{yT} of DP-340 deteriorates at a slower rate.

The ultimate strength σ_{uT} is defined as the peak stress of the nonlinear strain hardening region. Note that σ_{uT} is not necessarily the peak stress of the curve, because the upper yield strength of several cases with Mode 2 behavior is larger than the ultimate strength (e.g., the 600°C test for MS-1200). σ_{uT} is shown in Table 9, and the relationship between its retention factor $R_{\sigma uT}$ and T is shown in Fig. 19. No significant decrease is observed up to 200 °C or 300 °C. Above 300 °C, clear decreasing trends are observed, and the MS steel shows a more rapid deterioration rate than the DP steel.

By definition, ε_{yT} can be calculated by $\varepsilon_{yT} = \sigma_{yT}/E_T$, where the predictions of σ_{yT} and E_T are given in this section. ε_{shT} for residual tests with Mode 2 behavior is shown in Table 9, and the relationship between its retention factor $R_{\varepsilon shT}$ and T is shown in Fig. 20. ε_{shT} is stable up to 400 °C and then increases rapidly when T increases. ε_{shT} of MS steel increases more rapidly than DP steel.

Table 8
Required parameters of the proposed two-stage plus linear model from residual test with Mode 1 behavior.

T (°C)	DP-340	DP-700	MS-1030	MS-1200	DP-340	DP-700	MS-1030	MS-1200
	σ_{pT} (MPa)				ε_{euT}			
20	552.5	944.4	1379.3	1466.5	0.112	0.045	0.017	0.026
200	–	935.0	1424.7	1472.9	–	0.042	0.018	0.026
700	–	378.7	–	–	–	0.081	–	–
	n				m			
20	7.1	8.8	15.2	15.8	4.2	2.9	1.9	4.5
200	–	12.4	42.1	21.8	–	3.0	1.7	6.9
700	–	12.3	–	–	–	5.8	–	–

Table 9
Properties required by the proposed models from AHSS residual test results.

T (°C	DP-340	DP-700	MS-1030	MS-1200	DP-340	DP-700	MS-1030	MS-1200
	E_T (GPa)							
20	202.2	203.3	216.0	207.9				
200	210.4	208.1	212.9	207.4				
300	195.9	208.0	216.2	209.3				
400	218.2	213.3	211.8	204.5				
500	208.2	220.9	217.5	229.6				
600	205.3	217.7	231.8	215.0				
700	196.5	117.3	195.7	161.7				
	σ_{yT} (Mode 2) (MPa)				σ_{uT} (MPa)			
20	–	–	–	–	675.0	1025.6	1427.6	1594.8
200	528.6	–	–	–	690.6	1011.4	1455.7	1595.8
300	498.1	892.4	1371.0	1371.0	649.1	982.7	1389.8	1437.6
400	491.0	803.9	1030.0	1102.0	578.6	848.9	1041.2	1118.7
500	432.1	627.4	753.0	836.9	509.0	702.0	774.1	858.1
600	384.4	453.7	656.1	678.5	459.6	543.2	670.5	700.7
700	351.7	–	428.7	501.1	448.0	714.9	482.0	531.4
	ε_{shT} (Mode 2)				ε_{uT}			
20	–	–	–	–	0.154	0.075	0.027	0.036
200	0.018	–	–	–	0.159	0.072	0.039	0.040
300	0.015	0.014	0.013	0.014	0.129	0.048	0.044	0.036
400	0.021	0.014	0.015	0.014	0.146	0.033	0.030	0.040
500	0.030	0.018	0.039	0.036	0.146	0.098	0.059	0.055
600	0.037	0.028	0.041	0.047	0.177	0.138	0.071	0.069
700	0.038	–	0.050	0.055	0.200	0.099	0.177	0.126

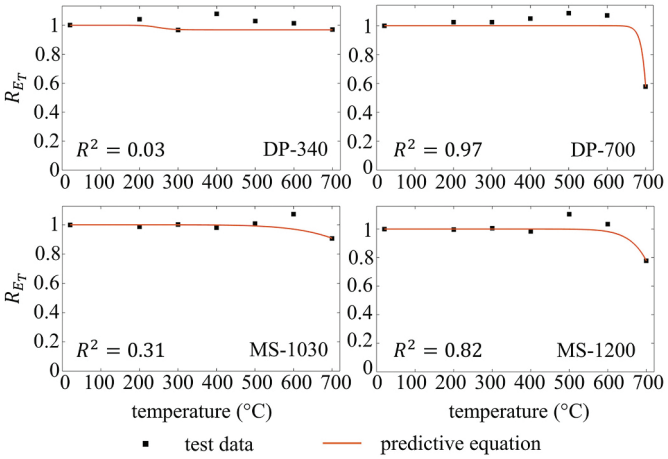

Fig. 17. Prediction of AHSS elastic modulus for residual tests by Eq. 26 using proposed coefficients.

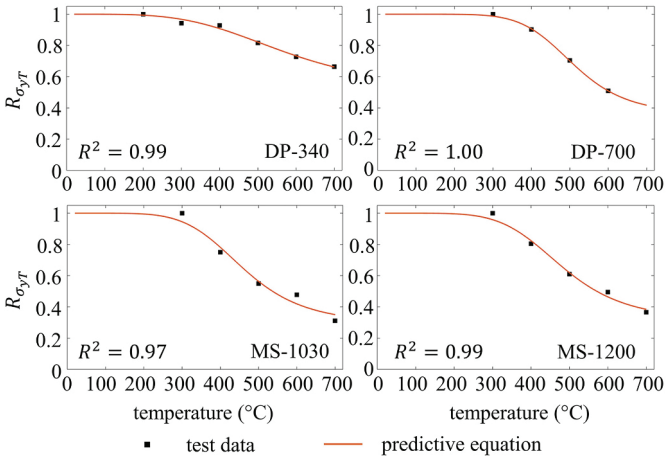

Fig. 18. Prediction of AHSS yield strength for Mode 2 residual tests by Eq. 26 using proposed coefficients.

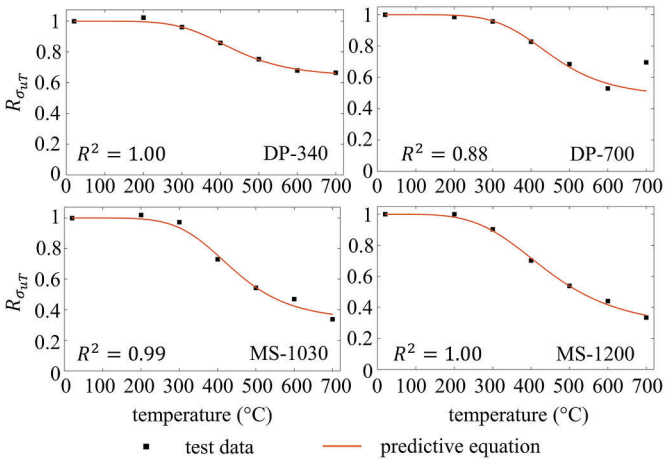

Fig. 19. Prediction of AHSS ultimate strength for residual tests by Eq. 26 using proposed coefficients.

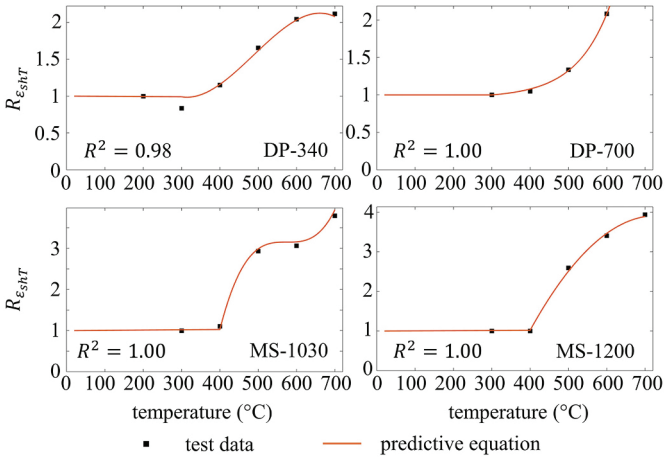

Fig. 20. Prediction of ε_{shT} for Mode 2 residual tests.

Table 10
Proposed coefficients for the unified predictive equation (Eq. 26) of material property parameters required by the updated bilinear plus nonlinear hardening model for the residual tests.

Steel	T (°C)	a	b	c	T (°C)	a	b	c
	E_T							
DP-340	[20, 700]	7.47E+05	12.47	0.97				
DP-700	[20, 700]	0.00	59.53	0.58				
MS-1030	[20, 700]	0.00	7.10	0.91				
MS-1200	[20, 700]	1.30E-05	15.80	0.78				
	σ_{yT} (Mode 2)				σ_{uT}			
DP-340	[200, 700]	2.14	3.85	0.66	[20, 700]	15.18	5.46	0.66
DP-700	[300, 600]	9.91	6.97	0.42	[20, 700]	12.56	5.66	0.51
MS-1030	[300, 700]	10.74	5.47	0.35	[20, 700]	14.04	5.51	0.37
MS-1200	[300, 700]	8.37	5.49	0.38	[20, 700]	7.30	4.24	0.35
	ε_{shT} (Mode 2)				ε_{uT}			
DP-340	[200,300]	0.00	0.00	1.00	[20, 500]	0.00	0.00	1.00
DP-700	–	–	–	–	[20, 400]	798.69	7.01	0.40
MS-1030	[300, 400]	0.00	0.00	1.00	–	–	–	–
MS-1200	[300, 400]	0.00	0.00	1.00	[20,300]	0.00	0.00	1.00

ε_{uT} is shown in Table 9, and the relationship between its retention factor $R_{\varepsilon_{uT}}$ and T is shown in Fig. 1.

The test data is used as benchmark to develop the predictive equations for the retention factor of the parameters required by the proposed model. The calibrated coefficients of the unified predictive equation (Eq. 26) for E_T, σ_{yT} (Mode 2), and σ_{uT} are shown in Table 10. The fits of these properties between the experimental values and the predicted values are shown from Fig 17 to Fig. 19.

For the required strain parameters, several cases captured from the test curves show an increasing trend at a higher temperature range (e.g., above 400 °C). Therefore, it is difficult to accurately predict these strains using the unified equation (Eq. 26) only. A combination of the unified equation and a polynomial function up to a cubic (Eq. 33) is used to develop the piecewise predictive equations for strains. These equations best fit the existing experimental data. A simpler function could be proposed if less accuracy to the current data is acceptable, especially considering the variability in strain.

$$R_{X_T} = aT^3 + bT^2 + cT + d \tag{33}$$

The calibrated coefficients of the unified predictive equation (Eq. 26) for the strains are shown in Table 10. The calibrated coefficients of the polynomial are shown in Table 11, where the required strains show a clear increasing trend when T increases. The fits of the strains between the proposed predictive equation and experimental value are shown in Fig 20 and Fig. 21.

$$\varepsilon_{450} = \begin{cases} \dfrac{\sigma_{450}}{98015} + 0.002\left(\dfrac{\sigma_{450}}{318.7}\right)^{5.13} & \text{for } 0 \text{ MPa} \le \sigma_{450} \le 318.7 \text{ MPa} \\ \dfrac{\sigma_{450} - 318.7}{23576} + 0.011\left(\dfrac{\sigma_{450} - 318.7}{48.6}\right)^{5.56} + 5.25E-03 & \text{for } 318.7 \text{ MPa} < \sigma_{450} \le 367.3 \text{ MPa} \\ 1.01E-03\,(\sigma_{450} - 367.3) + 0.018 & \text{for } 367.3 \text{ MPa} < \sigma_{450} \le 371.0 \text{ MPa} \end{cases} \tag{34}$$

Table 11
Proposed coefficients for the polynomial equation of required strains from AHSS residual tests.

	T (°C)	a	b	c	d
	ε_{shT} (Mode 2)				
DP-340	(300, 700]	−5.49E-08	8.03E-05	−0.034	5.51
DP-700	[300, 600]	0.00	1.70E-05	−0.012	3.03
MS-1030	(400, 700]	4.00E-07	−6.89E-04	0.40	−72.70
MS-1200	(400, 700]	0.00	−2.67E-05	0.04	−10.29
	ε_{uT}				
DP − 340	(500, 700]	0.00	0.00	1.47E-03	0.26
DP-700	(400, 700]	0.00	-3.33E-05	0.04	−10.11
MS-1030	[20, 700]	8.24E-08	−6.83E-05	1.56E-02	0.66
MS − 1200	(300, 700]	0.00	1.91E-05	-1.32E-02	3.25

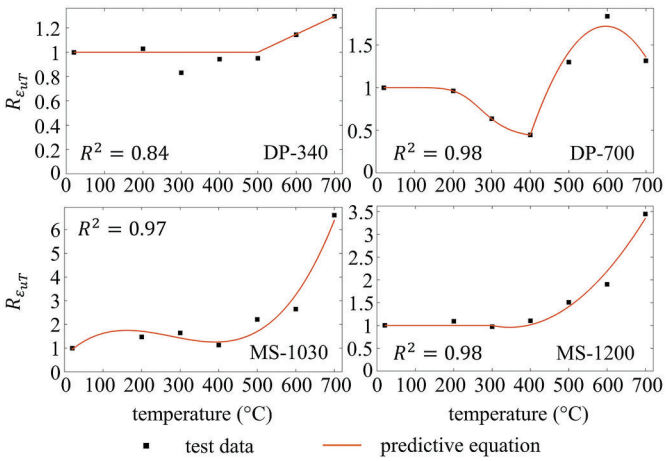

Fig. 21. Prediction for the ultimate strain for residual tests.

(Example 2) σ-ε modeling for DP-700 at 320°C from the transient-state test:

$$\varepsilon_{320} = \frac{\sigma_{320}}{133227} + 0.002\left(\frac{\sigma_{320}}{660.3}\right)^{7.49} \quad \text{for} \quad 0 \text{ MPa} \le \sigma_{320} \le 732.15 \text{ MPa} \tag{35}$$

(Example 3) σ-ε modeling for DP-340 after cooling down from 680 °C from the residual test:

$$\sigma_{680} = \begin{cases} 195814\varepsilon_{680} & \text{for} \quad 0 \le \varepsilon_{680} \le 1.82E-03 \\ 356.4 & \text{for} \quad 1.82E-03 < \varepsilon_{680} \le 0.039 \\ 356.4 + 92.0\left(0.029\varepsilon_{n680} + \dfrac{4.713\varepsilon_{n680}}{1 + 3.855\varepsilon_{n680}}\right) & \text{for} \quad 0 < \varepsilon_{n680} \le 1 \end{cases} \tag{36}$$

where σ_{680} in Eq. 36 is in MPa, $\varepsilon_{n680} = \frac{\varepsilon_{680} - 0.039}{0.156}$ for $0.039 < \varepsilon_{680} \le 0.195$.

7. Examples of AHSS stress-strain relationship modeling

In this study, models for AHSS stress-strain relationships in steady-state test, transient-state test, and residual test protocols based on experimental data are developed. The models can be used for material property definition in a numerical simulation for AHSS in various high-temperature scenarios. In this section a stress-strain modeling example for each type of test method following the procedures discussed in Sections 5 and 6 is provided.

The proposed models and model parameter prediction for each test method is summarized in Table 12. For models designed for Mode 1 stress-strain behavior, n and m at any desired temperature are calculated by linear interpolation between its two adjacent test temperatures given in Table 3. For the transient-state test modeling, the expression range is up to the ultimate strength, which is unavailable from the experiment. Therefore, the ultimate strength from the steady-state test is adopted as both test protocols are designed at elevated temperature, and the ultimate strength is only used to define the model range and has no influence on the model shape. The stress-strain modeling examples are shown in Table 13 and Eq. 34 for the steady-state test, Table 14 and Eq. 35 for the transient-state test, and Table 15 and Eq. 36 for the residual test.

Table 12
Summary of model expressions and model parameter predictive equations for each test method.

Test protocol	Model expression	Parameter prediction		
		predictive equation	parameter at ambient	equation coefficients
Steady-state test	Eq. 22	Eq. 26, 30, 31	Table 3	Table 4, 5
Transient-state test	Eq. 21	Eq. 26	Table 6	Table 7
Residual test	Eq. 24	Eq. 26, 33	Table 9	Table 10, 11

(Example 1) σ-ε modeling for MS-1200 at 450 °C from the steady-state test:

Table 13
Calculation of the required parameters of the proposed model for the steady-state test example.

Parameter	Calculation	Required parameters	Parameter value
Determination of intermediate parameters			
p	Table 2	–	0.002
T_{nor}	Eq. 27	$T = 450$°C, $T_{max} = 700$°C, $T_{min} = 20$°C	0.632
Calculation of independent parameters			
E_{450}	Eq. 26, Table 3 and 4	$E_0 = 207920$ MPa, $a = 1.17$, $b = 2.15$, $c = 0.06$	98,015 MPa
σ_{p450}	Eq. 26, Table 3 and 4	$\sigma_{p0} = 1466.5$ MPa, $a = 29.91$, $b = 4.73$, $c = 0.02$	318.7 MPa
σ_{u450}	Eq. 26, Table 3 and 4	$\sigma_{u0} = 1594.8$ MPa, $a = 29.27$, $b = 4.74$, $c = 0.04$	371.0 MPa
ε_{eu450}	Eq. 31, Table 3 and 5	$\varepsilon_{eu0} = 0.026$, $a = 5.05$E-3, $b = -1.56$	0.018
ε_{u450}	Eq. 31, Table 3 and 5	$\varepsilon_{u0} = 0.036$, $a = 3.96$E-3, $b = -1.18$	0.022
n_{450}	linear interpolation, Table 3	$n_{400} = 5.3$, $n_{500} = 4.9$	5.13
m_{450}	linear interpolation, Table 3	$m_{400} = 3.2$, $m_{500} = 7.9$	5.56
Calculation of dependent parameters			
ε_{p450}	$0.002 + \sigma_{p450}/E_{450}$	$\sigma_{p450} = 318.7$ MPa, $E_{450} = 98015$ MPa	5.25E-3
σ_{eu450}	$0.99\sigma_{u450}$	$\sigma_{u450} = 371.0$ MPa	367.3 MPa
E_{p450}	Eq. 23	$\sigma_{p450} = 318.7$ MPa, $E_{450} = 98015$ MPa, $n_{450} = 5.13$	23,576 MPa

Table 14
Calculation of the required parameters of the recommended model for the transient-state test example.

Parameter	Calculation	Required parameters	Parameter value
Determination of intermediate parameters			
T_{nor}	Eq. 27	$T = 320$°C, $T_{max} = 600$°C, $T_{min} = 20$°C	0.517
Calculation of parameters			
E_{320}	Eq. 26, Table 6 and 7	$E_0 = 214017$ MPa, $a = 0.00$, $b = 1.47$, $c = 0.01$	133,227 MPa
$\sigma_{0.2,320}$	Eq. 26, Table 6 and 7	$\sigma_{0.2,0} = 721.0$ MPa, $a = 6.13$, $b = 6.51$, $c = 0.07$	660.3 MPa
σ_{u320}	Eq. 26, Table 6 and 7	$\sigma_{u0} = 1025.6$ MPa, $a = 25.53$, $b = 6.25$, $c = 0.06$	732.15 MPa
n_{320}	linear interpolation, Table 6	$n_{300} = 7.8$, $n_{350} = 7.1$	7.49

Table 15
Calculation of the required parameters of the proposed model for the residual test example.

Parameter	Calculation	Required parameters	Parameter value
Determination of intermediate parameters			
T_{nor}	Eq. 27	$T = 680^{\circ}C$, $T_{max} = 700^{\circ}C$, $T_{min} = 20^{\circ}C$	0.971
Calculation of independent parameters			
E_{680}	Eq. 26, Table 9 and 10	$E_0 = 202232$ MPa, $a = 7.47E+5$, $b = 12.47$, $c = 0.97$	195,814 MPa
σ_{y680}	Eq. 26, Table 9 and 10	$\sigma_{y200} = 528.6$ MPa, $a = 2.14$, $b = 3.85$, $c = 0.66$	356.4 MPa
σ_{u680}	Eq. 26, Table 9 and 10	$\sigma_{u0} = 675.0$ MPa, $a = 15.18$, $b = 5.46$, $c = 0.66$	448.4 MPa
ε_{u680}	Eq. 33, Table 9 and 11	$\varepsilon_{u0} = 0.154$, $a = b = 0$, $c = 1.47E-3$, $d = 0.26$	0.195
ε_{sh680}	Eq. 33, Table 9 and 11	$\varepsilon_{sh200} = 0.018$, $a = -5.49E-8$, $b = 8.03E-5$, $c = -0.034$, $d = 5.51$	0.039
Calculation of dependent parameters			
ε_{y680}	σ_{y680}/E_{680}	$\sigma_{y680} = 356.4$ MPa, $E_{680} = 195814$ MPa	1.82E-03

8. Conclusions

This paper presents a detailed numerical study on the stress-strain relationships for two dual-phase (DP) and two martensitic (MS) advanced high strength steels (AHSS) at elevated temperatures and after cooling down. Test data recently collected by the authors from a series of steady-state, transient-state, and residual tests ranging from ambient to 700 °C are used as the modeling benchmarks. It was found that the stress-strain behaviors are affected by the composition of AHSS (DP or MS), the strength of the steel, the testing protocol, and the maximum temperature. Overall, two stress-strain modes were observed from steady-state and residual test protocols: a gradual strain hardening process with no well-defined yield point (Mode 1), and a sharp strain hardening process with a distinct yield point and yield plateau (Mode 2). In general, AHSS from the steady-state tests show Mode 1 while with a few exceptions for the residual tests, Mode 1 is observed when the test temperature is at or below 200 °C and Mode 2 is observed when the test temperature is 300 °C or higher. Therefore, no single material model could be defined to represent all AHSS subjected to elevated temperatures.

Existing stress-strain models were reviewed and fitted to the AHSS experimental data. It was found that existing models based on the Ramberg-Osgood equation do not accurately capture the Mode 1 stress-strain curves. Therefore, an updated two-stage plus linear model based on the Ramberg-Osgood equation is proposed to describe the stress-strain relationship of AHSS with Mode 1 behavior. An existing material model was found to fit Mode 2 stress-strain curves, but is updated to improve simplicity by reducing the number of required modeling parameters. The fit between the experimental AHSS stress-strain curves and the corresponding proposed models is excellent. Predictive temperature-dependent equations for the parameters required by the proposed models are developed using a unified equation based on the statistical analysis of the experiment data, and calibrated coefficients for the predictive equations are provided. In addition, the methodology developed in this paper could be helpful for future research on characterization of sophisticated material stress-strain behaviors.

Acronyms

AHSS	advanced high-strength steel
CFS	cold-formed steel
DP	dual phase steel
HSLA	high-strength low-alloy steel
MS	martensitic steel
R-O	Ramberg-Osgood model

Glossary

For the symbols of material properties, the subscript T represents the material property at elevated temperature T (for steady-state test and transient-state test) or cooling down from elevated temperature T (for residual test).

a, b, c, d: coefficients for the predictive equations of retention factors.
$E_{0.2T}$: tangent modulus at 0.2% proof stress; E_{pT} when $p = 0.002$.
E_T: elastic modulus.
E_{pT}: tangent modulus at p proof stress.
K_1, K_2, K_3, K_4: coefficients of the bilinear plus nonlinear hardening model.
m: the second strain-hardening exponent of two-stage or multi-stage Ramberg-Osgood model.
n: strain-hardening exponent of one-stage Ramberg-Osgood model; the first strain-hardening exponent of two-stage or multi-stage Ramberg-Osgood model.
p: plastic strain.
R_{XT}: retention factor for material property X.
T: test temperature.
$\varepsilon_{0.2T}$: strain of 0.2% proof stress.
ε_{euT}: strain of the equivalent ultimate point.
ε_{pT}: strain of the offset point.
ε_{shT}: (for Mode 2 stress-strain behavior) strain at the end of the yield plateau and the onset of the nonlinear strain hardening.
ε_T: strain.
ε_{uT}: ultimate strain.
ε_{yT}: strain of the yield point.
$\sigma_{0.2T}$: 0.2% proof stress; σ_{pT} when $p = 0.002$.
σ_{euT}: stress of the equivalent ultimate point.
σ_{nyT}: nominal yield strength.
σ_{pT}: proof stress with a plastic strain of p; stress of the offset point.
σ_T: stress.
$\sigma_{t0.5T}$: stress at $\varepsilon_T = 0.005$.
$\sigma_{t2.0T}$: stress at $\varepsilon_T = 0.020$.
σ_{uT}: ultimate strength.
σ_{yT}: yield strength.

Funding statement

Support for this research was provided to the first author by the University of Wisconsin - Madison Office of the Vice Chancellor for Research and Graduate Education with funding from the Wisconsin Alumni Research Foundation.

Declaration of Competing Interest

The authors declare that they have no known competing financial interests or personal relationships that could have appeared to influence the work reported in this paper.

References

[1] S. Keeler, M. Kimchi, P. Mooney, Advanced High-Strength Steels Application Guidelines, WorldAutoSteel, Brussels, Belgium, 6.0 edition, 2017.
[2] R. Kanno, Advances in steel structures and steel materials in Japan, ce/papers 1 (2017) 394–404.
[3] G. Shi, X. Chen, Research advances in HSS structures at Tsinghua University and codification of the design specification, Steel Construction 11 (2018) 286–293.
[4] Steel Construction Institute, High Strength Steel Design and Execution Guide, Technical Report, Steel Construction Institute, Berkshire, U.K., 2019.
[5] AISC, Committee on Specifications Task Group on High Strength Steel, Ad Hoc Task Group Report on High Strength Steel, Technical Report, American Institute of Steel Construction, Chicago, IL, U.S.A., 2019.
[6] American Institute of Steel Construction (AISC), ANSI/AISC 360–16: Specification for Structural Steel Buildings, Chicago, IL, U.S.A, 2016.
[7] American Iron and Steel Institute (AISI), S100–16: North American Specification for the Design of Cold-Formed Steel Structural Members, Washington, DC, U.S.A, 2016.
[8] European Committee for Standardization (CEN), Eurocode 3: Design of steel structures, part 1-2: General rules - Structural Fire Design, Brussels, Belgium, 2005.
[9] Standards Australia, AS 4100–1998 (R2016) Steel Structures, Sydney, Australia, 2016.
[10] T. Ranawaka, M. Mahendran, Experimental study of the mechanical properties of light gauge cold-formed steels at elevated temperatures, Fire Saf. J. 44 (2009) 219–229.
[11] X. Yan, Y. Xia, H.B. Blum, T. Gernay, Elevated temperature material properties of advanced high strength steel alloys, J. Constr. Steel Res. 174 (2020), 106299.
[12] X. Yan, Y. Xia, H.B. Blum, T. Gernay, Post-fire mechanical properties of advanced high-strength cold-formed steel alloys, Thin-Walled Struct. 159 (2021), 107293.
[13] J.H. Lee, M. Mahendran, P. Makelainen, Prediction of mechanical properties of light gauge steels at elevated temperatures, J. Constr. Steel Res. 59 (2003) 1517–1532.
[14] W. Chen, J. Ye, Mechanical properties of G550 cold-formed steel under transient and steady state conditions, J. Constr. Steel Res. 73 (2012) 1–11.
[15] Y. Huang, B. Young, Stress-strain relationship of cold-formed lean duplex stainless steel at elevated temperatures, J. Constr. Steel Res. 92 (2014) 103–113.
[16] J. Chen, B. Young, Stress-strain curves for stainless steel at elevated temperatures, Eng. Struct. 28 (2006) 229–239.
[17] J. Outinen, P. Mäkeläinen, Mechanical properties of structural steel at elevated temperatures and after cooling down, Fire and Materials 28 (2004) 237–251.
[18] J. Chen, B. Young, Experimental investigation of cold-formed steel material at elevated temperatures, Thin-Walled Struct. 45 (2007) 96–110.
[19] L. Gardner, A. Insausti, K.T. Ng, M. Ashraf, Elevated temperature material properties of stainless steel alloys, J. Constr. Steel Res. 66 (2010) 634–647.
[20] N.D. Kankanamge, M. Mahendran, Mechanical properties of cold-formed steels at elevated temperatures, Thin-Walled Struct. 49 (2011) 26–44.
[21] J. Ye, W. Chen, Elevated temperature material degradation of cold-formed steels under steady- and transient-state conditions, J. Mater. Civ. Eng. 25 (2013) 947–957.
[22] A. Landesmann, F.C.M. Da Silva, E. De Miranda Batista, Experimental investigation of the mechanical properties of ZAR-345 cold-formed steel at elevated temperatures, Mater. Res. 17 (2014) 1082–1091.
[23] M. Imran, M. Mahendran, P. Keerthan, Mechanical properties of cold-formed steel tubular sections at elevated temperatures, J. Constr. Steel Res. 143 (2018) 131–147.
[24] T.G. Singh, K.D. Singh, Mechanical properties of YSt-310 cold-formed steel hollow sections at elevated temperatures, J. Constr. Steel Res. 158 (2019) 53–70.
[25] J. Outinen, P. Mäkeläinen, Mechanical properties of structural steel at elevated temperatures, in: (Eds.), Advances in Steel Structures (ICASS'02), Elsevier, 2002, p. 1103.
[26] S. Gunalan, M. Mahendran, Experimental investigation of post-fire mechanical properties of cold-formed steels, Thin-Walled Struct. 84 (2014) 241–254.
[27] F. Azhari, A. Heidarpour, X. Zhao, C.R. Hutchinson, Mechanical properties of ultra-high strength (grade 1200) steel tubes under cooling phase of a fire: an experimental investigation, Constr. Build. Mater. 93 (2015) 841–850.
[28] J. Lu, H. Liu, Z. Chen, X. Liao, Experimental investigation into the post-fire mechanical properties of hot-rolled and cold-formed steels, J. Constr. Steel Res. 121 (2016) 291–310.
[29] Y. Huang, B. Young, Post-fire behaviour of ferritic stainless steel material, Constr. Build. Mater. 157 (2017) 654–667.
[30] C. Maraveas, Z.C. Fasoulakis, K.D. Tsavdaridis, Mechanical properties of high and very high steel at elevated temperatures and after cooling down, Fire Science Reviews 6 (2017).
[31] S. Kesawan, M. Mahendran, Post-fire mechanical properties of cold-formed steel hollow sections, Constr. Build. Mater. 161 (2018) 26–36.
[32] H.T. Li, B. Young, Residual mechanical properties of high strength steels after exposure to fire, J. Constr. Steel Res. 148 (2018) 562–571.
[33] T.G. Singh, K.D. Singh, Post-fire mechanical properties of YSt-310 cold-formed steel tubular sections, J. Constr. Steel Res. 153 (2019) 654–666.
[34] W. Ramberg, W.R. Osgood, Description of stress-strain curves by three parameters, technical report 902, in: National Advisory Committee For Aeronautics (NACA), 1943.
[35] A.O. Olawale, R.J. Plank, The collapse analysis of steel columns in fire using a finite strip method, Int. J. Numer. Methods Eng. 26 (1988) 2755–2764.
[36] E. Mirambell, E. Real, On the calculation of deflections in structural stainless steel beams: an experimental and numerical investigation, J. Constr. Steel Res. 54 (2000) 109–133.
[37] K.J. Rasmussen, Full-range stress-strain curves for stainless steel alloys, J. Constr. Steel Res. 59 (2003) 47–61.
[38] L. Gardner, M. Ashraf, Structural design for non-linear metallic materials, Eng. Struct. 28 (2006) 926–934.
[39] Z. Tao, X. Wang, B. Uy, Stress-strain curves of structural and reinforcing steels after exposure to elevated temperatures, J. Mater. Civ. Eng. 25 (2013) 1306–1316.
[40] J.B. Mander, Seismic Design of Bridge Piers, Ph.D. thesis, University of Canterbury, 1983.
[41] European Committee for Standardization (CEN), Eurocode 3: Design of Steel Structures, Part 1–1: General Rules and Rules for Buildings, Brussels, Belgium, 2016.
[42] European Committee for Standardization (CEN), Eurocode 3: Design of Steel Structures, Part 1–5: Plated Structural Elements, Brussels, Belgium, 2006.
[43] X. Yun, L. Gardner, Stress-strain curves for hot-rolled steels, J. Constr. Steel Res. 133 (2017) 36–46.
[44] S. Afshan, B. Rossi, L. Gardner, Strength enhancements in cold-formed structural sections - part I: material testing, J. Constr. Steel Res. 83 (2013) 177–188.
[45] L. Gardner, D. Nethercot, Numerical modeling of stainless steel structural somponents - a consistent approach, J. Struct. Eng. 130 (2004) 1586–1601.
[46] A.J. Sadowski, J.M. Rotter, T. Reinke, T. Ummenhofer, Statistical analysis of the material properties of selected structural carbon steels, Struct. Saf. 53 (2015) 26–35.
[47] L. Gardner, X. Yun, Description of stress-strain curves for cold-formed steels, Constr. Build. Mater. 189 (2018) 527–538.
[48] L. Gardner, X. Yun, Deformation characteristics of aluminium alloys, Gradjevinar 68 (2016) 179–190.
[49] C. Ding, Z. Li, H. Blum, Y. Xia, B.W. Schafer, Ductility demands on cfs structural connections of advanced high strength steel, in: Proceedings of the Cold-Formed Steel Research Consortium Colloquium, CFSRC, 2020.
[50] Y. Xia, C. Ding, Z. Li, B.W. Schafer, H.B. Blum, Numerical modeling of stress-strain relationships for advanced high strength steels, J. Constr. Steel Res. 182 (2021), 106687.
[51] X. Qiang, F.S. Bijlaard, H. Kolstein, Post-fire performance of very high strength steel S960, J. Constr. Steel Res. 80 (2013) 235–242.
[52] X. Yan, J.C. Batista Abreu, R.S. Glauz, B.W. Schafer, T. Gernay, Simple three-coefficient equation for temperature dependent mechanical properties of cold-formed steels, J. Struct. Eng. 147 (2021) 04021035.
[53] Y. Huang, B. Young, The art of coupon tests, J. Constr. Steel Res. 96 (2014) 159–175.

Engineering Structures 245 (2021) 112739

Contents lists available at ScienceDirect

Engineering Structures

journal homepage: www.elsevier.com/locate/engstruct

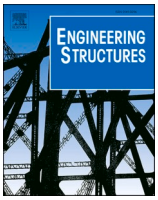

Structural analysis of steel structures with non-symmetric members

Edward J. Sippel, Hannah B. Blum

Department of Civil and Environmental Engineering, University of Wisconsin-Madison, Madison, WI 53706, USA

ARTICLE INFO

Keywords:
Finite element method
Second-order analysis
Non-symmetric sections
Open sections
Warping

ABSTRACT

Cold-formed steel components exist in a variety of structural systems including wall, floor, and roofing systems. A common feature of these cross sections is that they are often open and singly symmetric or point symmetric. While design requirements for these cross-sections account for the relevant effects resulting from their lack of symmetry, structural analysis programs do not always consider these effects. Engineers will use structural analysis programs to calculate the appropriate load sharing among members in the structural system. Accounting for the appropriate stiffness of each member and the related deformations is a vital component to determining the final distribution of bending moment, forces, and displacements. Many common structural analysis programs treat all sections as doubly symmetric without warping. Removing this assumption causes non-symmetric cross sections to exhibit nonplanar displacements and complicates the stability limits. The analysis of two structural systems composed of non-symmetric members was completed with varying member modeling assumptions utilizing multiple finite element software programs. A single channel portal frame was investigated that was subjected to simulated gravity load and wind loading with varying bracing support. Additionally, a roofing system with Z-section or channel purlins and channel bracing was investigated. The finite element analysis results were compared among the various modeling assumptions and existing experiments where available. It was observed that good agreement between the doubly symmetric and the more complex analyses was obtained in some instances, particularly when the members were loaded to low levels and highly constrained. However when loading is closer to the elastic limits and members can more freely move out-of-plane, the inclusion of non-symmetric section properties becomes a critical factor in determining an accurate response for both internal forces and displacements. The variations between these different analysis methods were found to be difficult to predict due to the cumulative effect of the competing mechanical behaviors that could result in either conservative or unconservative responses when ignoring non-symmetric behavior.

1. Introduction

Thin-walled cold-formed steel sections are often not doubly symmetric which results in complex structural behavior that cannot be fully defined by the base behavior introduced in a Mechanics of Materials course. The AISI Specification [1] identifies some of the complex behavior through the required design capacity provisions. These provisions include accounting for warping and the associated additional normal stresses, the effects of a nonconcentric shear center and centroid for a column buckling under axial load, and Wagner coefficients when defining the lateral torsional buckling capacity of a beam in bending. Other behaviors such as local and distortional buckling effects are also covered.

In contrast, the requirements for an elastic structural analysis for demand and serviceability detailed in the AISI Specification [1] do not cover the same scope of behaviors. The requirements related to behavior are primarily focused on a two-dimensional evaluation of cold-formed steel structures. The minimum required behavior includes (1) flexural, shear, and axial member deformations as well as effects of connection deformations with (2) second-order effects highlighting the inclusion of P-δ (member) and P-Δ (system) effects. The consideration of twist, warping, or non-symmetric section properties is left to the discretion of the engineer. In the design phase, the impact of twist including warping effects and second-order twist effects is highlighted in a user note and commentary for the Direct Strength Method which indicates that ignoring these effects may underestimate elastic buckling capacities. Ziemian et al. [2] showed how the twisting of doubly symmetric sections can result in significantly different displacements and internal forces when ignoring warping effects. This response is amplified in non-symmetric sections as they are often either not loaded in alignment with a single principal axis or not loaded through the shear center which introduces an initial out-of-plane deformation including twist.

In addition to engineering judgement for determining which modeling assumptions to utilize, an engineer is often limited by the abilities of the structural analysis software available to them. Many structural analysis programs utilize a line (beam) element that assumes a

https://doi.org/10.1016/j.engstruct.2021.112739
Received 16 December 2020; Received in revised form 16 May 2021; Accepted 15 June 2021
Available online 6 August 2021

doubly symmetric cross section with six degrees of freedom per end of the element [3,4] which results in linear torsion and the exclusion of warping effects [1]. Non-doubly symmetric cross sections employed in these programs commonly assume the member to behave as a doubly symmetric section in the principal orientation. Any specific non-symmetric section behavior is left to the user to attempt to model with some direction from design guides, help forums, and experience. Recent work by various researchers [5–9] has resulted in new line element formulations that remove the doubly symmetric assumption and related approximations and instead, directly account for the twisting effect associated with members with non-symmetric (singly symmetric, point symmetric, and asymmetric) sections. The work by Liu et al. [8] has been implemented into the structural analysis algorithms within MASTAN2 [10], along with additional tools to readily model these sections, and in part, provides a basis for this paper.

Another important facet of the evaluation of structures is the connection behavior. Recent work has sought new ways to capture this response as even a simple rigid connection with thin-walled members provide challenging interactions at connection due to warping effects [11]. Shayan and Rasmussen [12] modeled connection behavior in doubly symmetric I-beams using line elements by adding springs to the fixed connection to simulate warping effects. Sapountzakis and Dikaros [13] modeled connection behavior directly using line elements by introducing a number of additional degrees of freedom to capture distortion. Hansen and Jönsson [14] isolated the connection behavior by using a hybrid modeling approach with shell elements to create the connection which was then transitioned to a less demanding line element for the remainder of the span. In non-symmetric sections, Hancock [15] and Rinchen et al. [16] noted the connection behavior was complicated further due to all internal forces not acting at a single concentric location which complicated the bimoment.

The primary objective of this paper is to report on a study that compared results determined from analyses using different modeling approaches of structural systems with members comprised of non-symmetric sections. Solutions of a shell element model, a doubly symmetric line element model, and a non-symmetric line element model are presented. This paper builds on the previous evaluation of single members including an angle, channel, and Z-section and a simple I-beam portal frame presented in Sippel et al. [17]. The systems presented in this paper include a single channel portal frame with connection discontinuities and a roof system containing discretely braced cold-formed Z-section or channel purlins.

2. Structural Analysis Methodology

Many different options and methods are available to engineers to complete their structural analysis. A common approach for practicing engineers is to use a commercially available structural analysis program that implements a conventional line element that assumes a doubly symmetric cross section. If the engineer wants to avoid this assumption, an alternative would be to utilize finite element models created with shell or solid elements. However, even a small structure modeled this way would become unwieldy quite quickly. A preferable alternative would be to implement a line element evaluation that can readily account for both symmetric and non-symmetric section within existing modeling procedures.

Table 1
Analysis results labels.

Program	Analysis Element	Label
SAP2000	**D**oubly **S**ymmetric line element without warping	DS-1
RFEM	**D**oubly **S**ymmetric line element without warping	DS-2
MASTAN2	**N**on-**S**ymmetric line element with **W**arping	NSW-1
Abaqus	**N**on-**S**ymmetric line element with **W**arping	NSW-2
Abaqus	Shell element	Shell

The main focus of this study was to compare the analysis results of a structural system and not a program specific algorithm. Table 1 provides abbreviations of the analysis models employed based on the underlying model behavior. SAP2000 [18] and RFEM [19] were used represent an analysis in which members are assumed to have a doubly symmetric cross section and ignore warping effects. The default line (beam) element within each program, that utilize 12 degrees of freedom per element, were used. The use of both programs allowed for cross validation of the results as there are possible variations in the underlying formulations. The analysis of non-symmetric cross sections was completed with the use of MASTAN2 [10] and Abaqus [20]. Within MASTAN2, the analysis models were completed with the default line element which permits the modeling of symmetric and non-symmetric section with its 14 degree of freedom line element. Of the multiple line elements in Abaqus, the B31OS line element [21] was utilized. Similar to MASTAN2, this element is a two node, three-dimensional open section element that includes warping effects. It differs from MASTAN2 in that integration is employed within each load increment to obtain the element stiffness matrices. Similar to the doubly symmetric analyzes, the use of both non-symmetric programs allowed for cross validation of a line element response while also allowing for verification of the results from the novel MASTAN2 approach. These line element models were also compared with SR4 shell element models that were created in Abaqus.

With this study focused on the system behavior of non-symmetric sections, each of the structural analysis programs was first assessed for the ability to model minimum behavioral requirements. The verification started with two-dimensional, geometrically nonlinear analysis identified through the commentary in the AISC Specification for Structural Steel Building [3] as AISC and AISI have similar base analysis requirements. It was noted that all of the structural analysis methods considered are capable of capturing consistent flexural, shear, and axial member deformations with consideration of P-δ and P-Δ effects with a summary provided in [17]. The next level of validation evaluated the three-dimensional analysis with twisting effects based on the advanced analysis example presented in the commentary of the AISC Specification. Each set of analysis results were in agreement with the reference solutions, which provided different results based on whether nonuniform torsion (warping) was included in the evaluation. Ignoring the effects of warping is often considered conservative for the analysis of hot-rolled steel sections as discussed in Ziemian et al. [2] due to the softer twisting response. The exclusion of warping will cause increase initial rotations; however, it becomes difficult to predict the overall response as the increased rotation can cause unexpected changes to the expected load path [17]. After establishing a baseline behavior, a study of individual non-symmetric members was completed as discussed in [17]. Three example problems were introduced that identified specific non-symmetric section responses. The more sophisticated analyses were able to capture behaviors that were missed by the doubly symmetric evaluations. These behaviors included the translation of a non-symmetric section due to twist, buckling interactions with shear center offsets, and bi-axial bending responses. In these individual members, a primary factor driving the observed differences could often be noted; however, in a slightly more complex system, such as a mono-symmetric I-beam portal frame, the combined interactions quickly made it difficult to assign a cause to variations in displacement and moment reactions.

The comparison of the structural systems in this study was primarily focused on the forces and displacements determined using each analysis method. This comparison also included consideration of stability while observing the same details. This investigation into stability was limited to behaviors captured by line elements, a primary component of this study. As a result, scenarios where local and distortional effects controlled the behavior were not evaluated with the various analysis methods.

3. Portal Frame

3.1. Portal Frame Description

The first example was of an experimental series of single bay, single channel portal frames tested by Baigent and Hancock [22]. The channel portal frames allowed for an investigation into the deformation of channels under combined loading. The combined loading response was of interest as previous investigations with lipped channels indicated that combined interactions required non-symmetric modeling to accurately capture the complete behavior [17].

The typical portal frame is described in [22] with more detailed information provided in [23]. Fig. 1 shows the left-hand side of the frame geometry which would be mirrored about the centerline to obtain the full frame. The frame was subjected to three loading combinations illustrated in Fig. 2 representing vertical only loading (Case 1), transverse wind loading (Case 2), and longitudinal wind loading (Case 3) with one of two lateral support conditions. The first condition provided support at the external lateral bracing locations only, while the second condition provided support at the external and internal lateral bracing locations. The external lateral support was applied at the locations marked by a • in Fig. 1 to simulate purlins and girts. The addition of the interior supports at the locations marked with an 'x' simulated fly-bracing by introducing a torsional restraint to the channels due the second lateral support. The loading shown in Fig. 2 was applied at the same location as the external lateral support using suspended lead weights. The frame was constructed with lipped channels as the main members and custom bracket connections with the cross-section dimensions shown in Fig. 3 [23]. The modulus of elasticity was taken as 203 GPa with a Poisson's ratio of 0.3.

3.2. Portal Frame Modeling Details

As part of their investigation, Baigent and Hancock [22] presented good agreement between the experiments and their models. As such, the models built in this study were constructed to best replicate major modeling features which primarily focused on the connections at the eave and apex. Baigent and Hancock treated the connection brackets as rigid links due to the significantly thicker and larger sections used which was similarly used in this study. The connection brackets were only bolted to the channel web which was modeled as a fixed connection

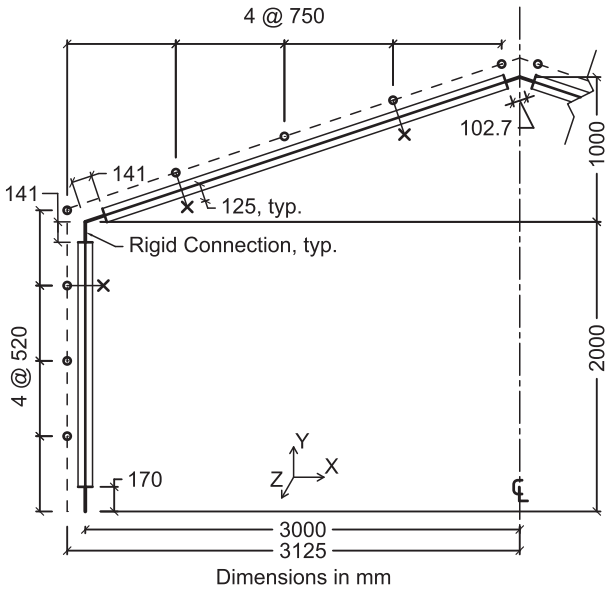

Fig. 1. Single channel portal frame geometry. Dimensions shown are symmetric.

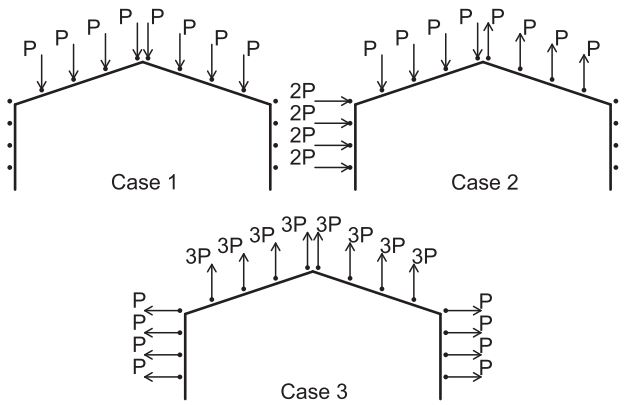

Fig. 2. Three loading scenarios applied to portal frame.

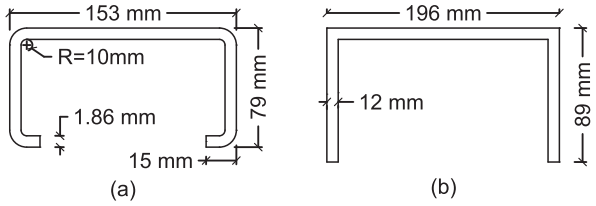

Fig. 3. Cross-sectional dimensions of (a) lipped channel and (b) bracket.

allowing for the transfer of moments and forces with the warping unrestrained in the connection or channel. Lastly, the original model accounted for the connection behavior at the middle of the channel web which was implemented in the various models.

Following the geometry indicated in Fig. 1, the channel portal frame models were created with the channel members between rigid connections. The channel members were assumed to extend between the center of the bolt group on each end. The base of each column was modeled as a hinge only free to rotate about the z-axis. In the physical experiment, brackets were attached to the flanges of the main channels and connection brackets to allow for the attachment of lateral supports and to apply the vertical loading. As a result, the support nodes were centered on the flange of the channel, 125 mm from the strong axis of the section. This node was then pinned in the z-direction.

The line element models were readily created based on the above features. The necessary offsets were obtained using rigid links. Each model was meshed uniformly between critical dimensions with a reference size of 50 mm based on the mesh study completed as part of an earlier phase in this study [17].

The shell element models were created to replicate the same modeling assumptions as the line element models. The fixed but free to warp connection constraint at the ends of channels was created by a rigid tie along the web of the channel. The rigid tie on the web was extended along the length of the member as illustrated in Fig. 4 to ensure weak axis moment connection. The 60 mm extension of the rigid ties were aligned with the bolt position to approximate the internal cover plate at the eave and apex. The rigid tie at the web was readily integrated into a rigid assembly that included the supports at the column base and eave connections. Due to modeling constraints and the need to include two lateral supports at the apex connection, a shell element model of the apex was included as a deformable body. To approximate rigid deformation in this connection, this larger channel bracket was defined with a modulus of elasticity 10 times the standard value and a full depth stiffener at the lateral support locations. The remaining lateral supports and loading offsets were obtained using a 12 mm thick tab directly attached to the flat of the channel flange with the increased modulus of elasticity. The shell element model was meshed with a seed size of 2 mm.

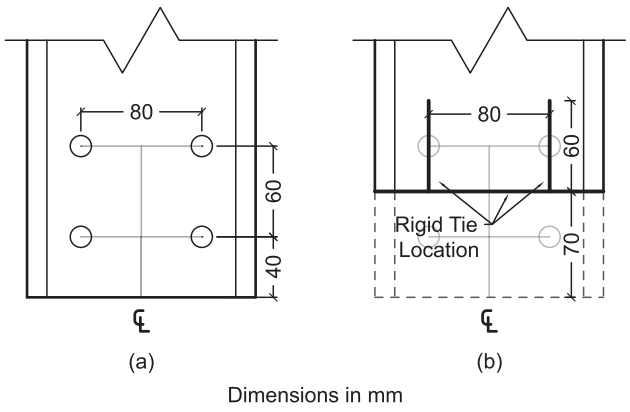

Fig. 4. Dimensions of channel (a) end bolted connection and (b) rigid tie model.

The loading was applied to all models as point loads on the appropriate nodes. This study was completed using an undeformed model because no initial imperfections was noted in the prior model evaluation [22] and the offset of the applied loading would introduce out-of-plane effects without additional imperfections. This decision was reinforced by the two sets of experimental results available for Case 1 with lateral supports exhibiting similar elastic responses prior to local failure of the channels with different imperfections. Since the actual failure mode of frames was local buckling in the channel members, no stability analysis was considered for this frame as the limiting behavior would not be captured by the line element analyses.

This study considered the same loading procedure as the physical experiment with a preload step and then the full load incrementally applied. The initial preload was included as it applied loading to the frame in a slightly different distribution compared to the full load increments while still being a significant fraction of the total vertical load applied. The undeformed model was initially loaded with 175 N in the vertical direction and 10 N in the horizontal direction at each node corresponding to the loading directions shown in Fig. 2. After this initial step, the loading was increased at each node corresponding to the loading distribution indicated in Fig. 2.

3.3. Portal Frame Results

The available experimental data in [23] provided the in-plane deformation for most of the test configurations. As shown in Fig. 5, the shell analysis model was capable of reasonably modeling the main behavior of the frames while most line element models were stiffer. In this example where the frame is only laterally supported, the non-symmetric line element analyses captured a softer displacement response compared to the doubly symmetric evaluation. This different response between the doubly symmetric and non-symmetric evaluations could be observed in other load cases as well as shown for Case 3 for the lateral displacement, Fig. 6, and the vertical displacement, Fig. 7, of the rafter. The variation between the methods decreased as the channel members where more restrained with the addition of the internal lateral support. Similar results from Case 1 are highlighted in Table 2 which summarizes some results with absolute error to the shell model results provided in parentheses after the numeric value. Another significant change to the system shown in Table 2 was the out-of-plane behavior. With only the external restraint, the non-symmetric analyses displayed 60% larger out-of-place displacement than the doubly symmetric behavior in Case 1. However once the internal restraint was added, minimal variation was observed in the different line element methods.

The non-symmetric structural analysis procedures were reviewed since the results from this study were found to be stiffer than those from the modeling results plotted by [24]. The primary difference noted between these methods was the transfer of forces at the connections, particularly bimoment. Both methods in this study and the previous work by Baigent and Hancock allow for the end of an element to be defined as continuous, fixed, or free for warping. The difference is the effects of bimoment due to changes in the cross section and orientation. The work by Baigent and Hancock included bimoment variations due to the offset shear center and bending moment and the compatibility with the adjacent connection bracket. This additional bimoment would introduce additional twist to the system which would cause additional weak-axis bending of the section due to the rotation of the section and thus an overall softer response. While not fully explored in this study, the free to warp (zero bimoment) condition at the end of the connection brackets resulted in a bimoment distribution within the channel per [24] that could not be reproduced within either of the non-symmetric line

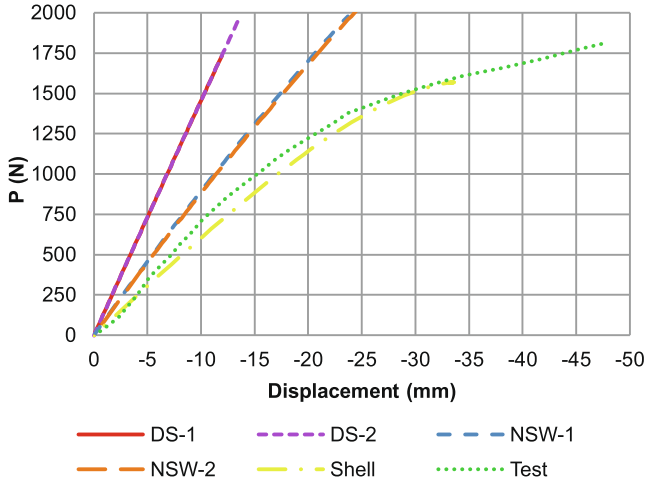

Fig. 5. Vertical displacement at midspan of left rafter for Load Case 1 with external lateral support.

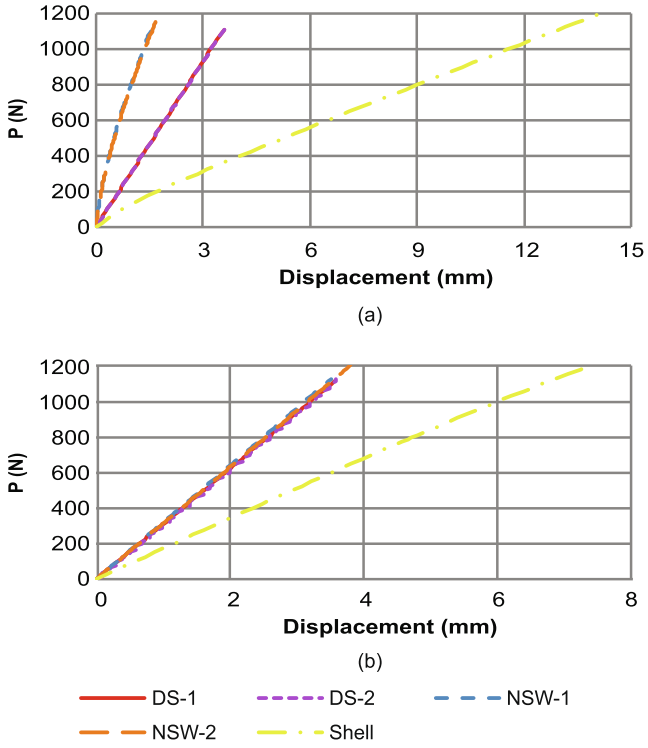

Fig. 6. Lateral displacement at midspan of left rafter for Load Case 3 with (a) external lateral support and (b) internal and external lateral support.

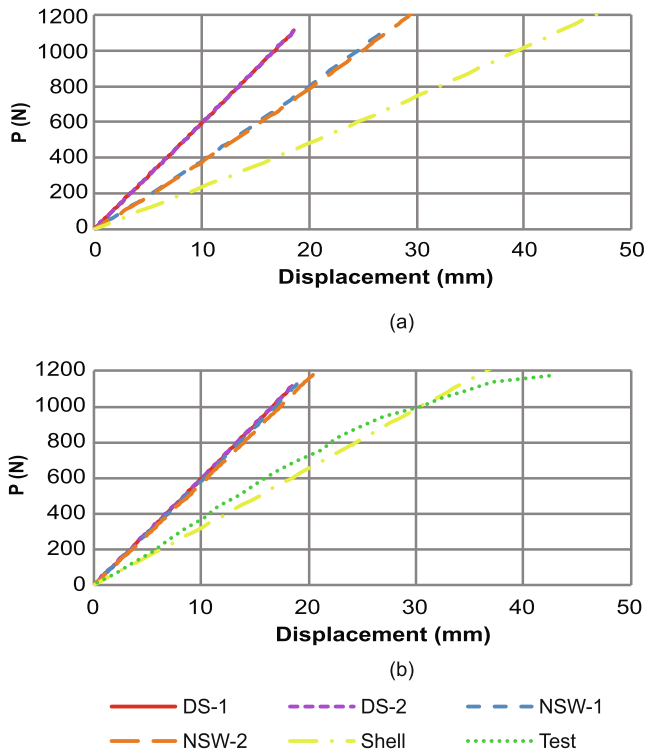

Fig. 7. Vertical displacement at midspan of left rafter for Load Case 3 with (a) external lateral support and (b) internal and external lateral support.

Table 2
Analysis results for single channel portal frames at P = 500 N.

Load Case 1 with Exterior Lateral Supports						
Results	DS-1	DS-2	NSW-1	NSW-2	Shell	Test
Ux-2 (mm)	-1.83 (41.9%)	-1.82 (42.2%)	-2.01 (36.2%)	-2.04 (35.2%)	-3.15	-2.78
Uy-3 (mm)	-3.45 (58.6%)	-3.44 (58.8%)	-5.53 (33.7%)	-5.63 (33.7%)	-8.34	-7.29
My-1 (N-m)	27.2 (172%)	27.2 (172%)	-33.9 (9.8%)	-34.7 (9.8%)	-37.6	-
Uz-3 (mm)	-1.88 (77.9%)	-1.88 (77.9%)	-5.43 (36.3%)	-5.43 (36.3%)	-8.52	-
Load Case 1 with Exterior and Interior Lateral Supports						
Results	DS-1	DS-2	NSW-1	NSW-2	Shell	Test
Ux-2 (mm)	-1.78 (45.2%)	-1.80 (44.6%)	-1.79 (44.9%)	-1.82 (44.0%)	-3.25	-2.61
Uy-3 (mm)	-3.45 (46.1%)	-3.40 (46.9%)	-3.50 (45.3%)	-3.58 (44.1%)	-6.40	-4.66
My-1 (N-m)	27.1 (171%)	27.1 (171%)	-39.7 (4.2%)	-40.2 (5.5%)	-38.1	-
Uz-3 (mm)	-0.02 (98.7%)	-0.03 (98.1%)	-0.09 (94.3%)	-0.09 (94.3%)	-1.59	-
Load Case 2 with Exterior Lateral Supports						
Results	DS-1	DS-2	NSW-1	NSW-2	Shells	Test
Uy-3 (mm)	-3.75 (54.8%)	-3.72 (55.2%)	-4.11 (50.5%)	-4.12 (50.4%)	-8.30	-8.14
Fy-4 (N)	-251 (1.2%)	-251 (1.2%)	-252 (1.6%)	-249 (0.4%)	-248	-

Position Number: 1 = Left Column Base Connection, 2 = Left Eave, 3 = Midspan of Left Rafter, & 4 = Right Column Base Connection.

elements in this study. The selected elements do not have an ability to relate applied forces at the end of the member to internal bimoments. The internal bimoment can only develop at a continuous or fixed warping condition.

4. Roof System with Z-Section Purlins

4.1. Roof System Description

When assessing a structural design, an engineer will often utilize a general understanding of how the structure will behave to simplify the necessary evaluations. For example, an engineer may evaluate a roof purlin as an individual element and separately design the supporting beams and bracing. However, this process requires an assumption of the underlying response. In a roof system, the consideration of an unrestrained bending response with non-symmetric sections introduces additional biaxial bending and twisting effects which may not be considered in a simplified component analysis. To study the combined response of the entire system, the single slope roof shown in Fig. 8 was considered which included non-symmetric roof members supported by rolled I-beams. The cross-section designations that follow are listed by the equivalent metric size followed by the standard American section size.

The four inclined W310x38.7 (W12x26) I-beams carry continuous Z-section purlins, 305Z76-254 M (1200Z300-100). As the design assumed no bracing from the roof deck, the purlins were considered discretely braced by channels, 203S70-144 M (800S275-57). A single channel brace at midspan was used based on work by Sputo et al. [25] that a single brace could provide adequate restraint. Fig. 9 depicts the stacked configuration of the purlin and I-beams as well as the angle, L51x51x3.2 (L2x2x1/8), fly bracing included at the •'s in Fig. 8(a) which braced the I-beam bottom flanges. The I-beam and angle members were modeled with a modulus of elasticity of 200 GPa and the Z-section and channel members were modeled with a modulus of elasticity of 203 GPa. All members were modeled with a Poisson's ratio of 0.3.

The roof system was evaluated for the application of a downward vertical load simulating dead/live loading and an upward load perpendicular to the roof slope to simulate wind loading. This loading was applied as a uniform distributed load at the purlin centroid. The roof system was evaluated for two cases. Case 1 considered a finite 1.5 kN/m load to establish a baseline comparison point. Case 2 considered the elastic stability limits to identify the analysis behavior at high loading levels.

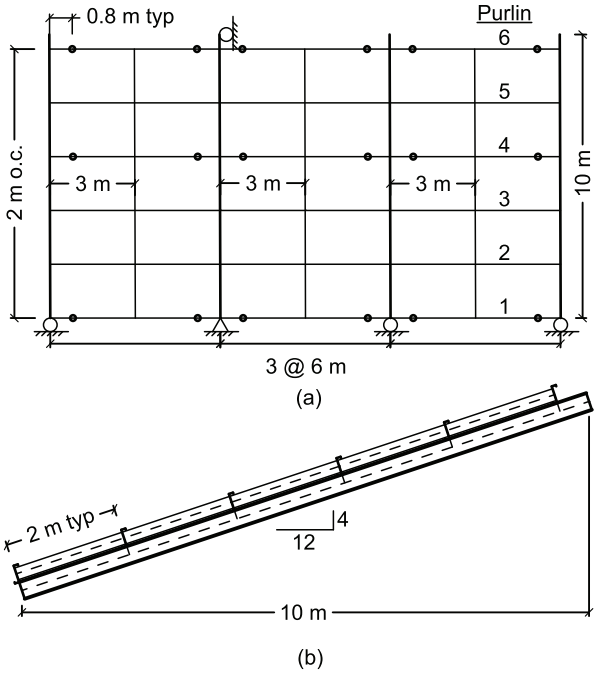

Fig. 8. Roof layout (a) Plan view (b) Section view.

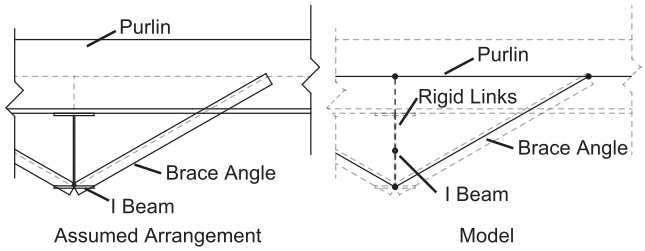

Fig. 9. Kicker brace positioning.

4.2. Roof System Modeling Details

Support reactions were only applied at the I-beams. All beam ends were supported in the vertical direction and lateral restraints were applied as shown in Fig. 8. The longitudinal reactions at the bottom of the I-beams allowed each beam line to resist wind pressure. Minimal reactions were applied in the transverse direction to provide stability. The ends of the I-beams were free to warp and torsional restraint was provided by the fly-bracing.

The purlins were modeled as continuous members across the I-beams. Each support connection allowed for the transfer of shear, axial load, and torsion out of each purlin. The ends of the purlins were free to warp. The midspan channel bracing was treated as a torsional brace through a web only connection. This configuration only precluded the transfer of weak axis moment at the connection and allowed the ends of the channel to be free to warp.

The continuous purlins were modeled in a prismatic condition with a constant cross section. Epstein et al. [26] investigated the design of purlins with continuous top flange bracing so that full cross section yield could be achieved for positive moment. A nonprismatic condition accounting for the lap length with increased stiffness was found to give conservative and more accurate results. The increased stiffness resulted in larger negative moments at the supports which was led to more critical conditions at the common limiting locations, either the end of the lap or at the support. A consequence of the nonprismatic modeling approach was that the maximum positive moment decreased as well. In this study, the long unbraced length of the purlin would preclude reaching full yield of the section in actual design. As a result, the maximum positive moment at midspan was considered a critical value and could be best obtained using a prismatic evaluation.

The section properties of the cold-formed members were based on a thin-walled model with sharp corners. While common bend radii are available, the exact radius used by the reference manufacturer was not indicated. Variability was also found in the bend angle of the Z-section flange. As a result, this study opted for a simplified geometry to aid repeatability.

The line element models were meshed with a seed of 200 mm for all members. The stacked geometry and offset connection shown in Fig. 9 were obtained using rigid links. The distributed loading mentioned above was applied along the length of each element.

The shell element model was meshed with a seed of 5 mm for all members. The I-beam restraints were applied to a rigid tie across the height of the web. Similarly, the purlin to I-beam connections included a rigid tie over the height of the purlin web to transfer shear forces along the full height of the member. These rigid ties were then connected to the top flange of the I-beam using a MPC constraint that allowed for the transfer of torsion but no other moments. The distributed load was applied as point loads at the centroid of the purlin based on the tributary length of the element.

The evaluation of elastic stability needed as part of Case 2 was completed using a nonlinear static analysis in all analysis programs and an eigenbuckling analysis where possible. The nonlinear analyses were determined to have reached a maximum loading when an instability was observed. The onset of instability was identified by a significant change in deformations or if the model would fail to converge due to the instability. In either instance, the results were verified to have a similar loading and deformation response as the eigenbuckling analysis or to have indicated a negative or zero stiffness near failure. As the selected doubly symmetric structural analysis programs could not complete an eigenbuckling evaluation considering moments, conventional doubly symmetric elements ignoring warping were evaluated in MASTAN2 and Abaqus to confirm the underlying behavior.

4.3. Roof System Results

For this study, the primary results of interest are the forces and displacements of the various members. Based on the magnitude of loading alone though, it is difficult to have an understanding of how heavily loaded the structure is. To provide context, a demand capacity ratio for purlins based on the interaction of strong and weak axis moment was provided. While not detailed in this paper, the capacity limits of the purlin relative to the AISI Specification [1] were considered including combined effects from shear, web crippling, and torsion. A preliminary investigation considering these effects found that the moment demand capacity ratio was the limiting relationship and provided a useful metric for how much additional loading could be expected to be supported by the roof. The values provided in Table 3 were determined using the Direct Strength Method with a 3 m unbraced length considering the principal orientation [27].

The results of the finite 1.5 kN/m loading were similar among all the analysis methods when comparing the maximum vertical deflections, the moment along the supporting I-beams, and the demand capacity ratio for the purlins considering major and minor axis bending at midspan. A sampling of the results are shown in Table 3 with absolute error relative to the shell solution. An interesting result across all analysis methods was the change in moment at the supports. The largest moments at the interior supports could be observed in the first purlin, which is labeled on the right side of Fig. 8(a), due to no differential displacements of the support beams. These interior support moments were found to decrease as the differential deflection of the I-beams increased as one moved away from the supports. This change resulted in larger positive moments at midspan which aligned with the prismatic model decision discussed earlier.

The point symmetric geometry of the Z-section means that two different orientations, geometric or principal, can be considered for the section. Either orientation may be appropriate for moment comparison depending on the design approach taken with the geometric orientation

Table 3
Analysis results for roof system with 1.5 kN/m distributed load.

Downward Loading					
Results	DS-1	DS-2	NSW-1	NSW-2	Shells
Beam Mx (N-m)	59551 (2.1%)	59600 (2.0%)	59526 (2.1%)	59197 (2.7%)	60810
Beam Uy (mm)	38.3 (2.0%)	38.0 (2.8%)	37.9 (3.1%)	38.0 (2.8%)	39.1
Purlin Uy (mm)	41.0 (5.7%)	40.6 (6.7%)	40.7 (6.4%)	40.9 (6.0%)	43.5
Purlin 1 Ratio	37.6%	35.9%	32.8%	33.0%	37.5%
Purlin 4 Ratio	33.0%	28.7%	22.6%	23.1%	21.4%
Uplift Loading					
Results	DS-1	DS-2	NSW-1	NSW-2	Shells
Beam Mx (N-m)	63297 (1.7%)	63331 (1.7%)	63193 (1.9%)	62935 (2.3%)	64420
Beam Uy (mm)	40.9 (1.9%)	40.5 (2.9%)	40.3 (3.4%)	40.4 (3.1%)	41.7
Purlin Uy (mm)	43.2 (2.9%)	42.8 (3.8%)	42.9 (3.6%)	43.1 (3.1%)	44.5
Purlin 1 Ratio	36.2%	36.6%	35.1%	35.9%	34.2%
Purlin 4 Ratio	45.5%	44.5%	43.1%	43.4%	44.4%

associated with the Effective Width Method and the principal orientation with the Direct Strength Method. Therefore, the variation of moment in both orientations was evaluated with the results along the fourth purlin discussed as an example. The strong axis moment for both loading scenarios, in either orientation, were still in good agreement. However, variations existed in the weak axis moment distributions in both the geometric orientation, Fig. 10, and the principal orientation, Fig. 11, for the vertical loading. In either orientation, there was a consistent overestimate of the weak axis moment between the end of the member and the first brace in the doubly symmetric analyses. While vertical loading introduced an increased demand prior to the brace, a more complex variation in the weak axis moment was observed in the uplift load case as shown in Fig. 12 and Fig. 13. As the applied loading was aligned with the geometric orientation, Fig. 12 provides a helpful means to understand the response. The weak axis moment distribution is a combined response due to the torsional support reactions from braces and the I-beams and second-order twisting effects dues to the applied loading and lateral displacements. In the non-symmetric analyses, the increased torsional stiffness from including warping meant that minimal second-order twisting effects were included in the response. In contrast, the softer torsional stiffness of the doubly symmetric analyses allowed for significant second-order effects. This variation was amplified in the uplift case as the loading was oriented 7° further from the principal orientation than the vertical loading resulting in more initial lateral displacement to cause a larger second-order response.

When evaluating the roof systems for elastic stability, the different analysis methods indicated significant variations in the controlling response as summarized in Table 4 for the nonlinear static analysis. The observed failure of the system in more sophisticated analyses methods was the full roof system buckling laterally for the vertical loading and the interior beams buckling under uplift as depicted in Fig. 14(a) and (b), respectively. The shell element model nonlinear analysis was in good agreement with the eigenbuckling evaluation which found limiting loads of 3.7 kN/m downwards and 3.3 kN/m in uplift. While identifying the same failure mode, the non-symmetric line element nonlinear analyses found stability limits at slightly lower values in the downward loading scenario and slightly larger values in uplift which followed with the eigenbuckling results, 3.5 kN/m downwards and 3.8 kN/m in uplift. The doubly symmetric analyses introduced a different failure mode where the central channel braces were buckling due to the applied moment. In the eigenbuckling evaluation, the first channels were observed to buckle at loads of 1.3 kN/m downwards and 1.6 kN/m in uplift. In the nonlinear analysis, the system was able to accommodate multiple braces reaching the elastic limit as depicted by the eigenbuckling shown in Fig. 15. However, after the failure of three braces the purlins were not able to support additional loading to reach the stability limit of the full system.

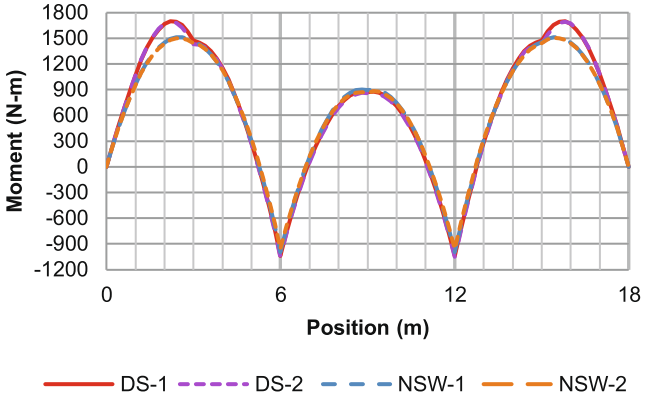

Fig. 10. Geometric weak axis moment from vertical loading along 4th purlin. Position = 0 is the left side of Fig. 8a.

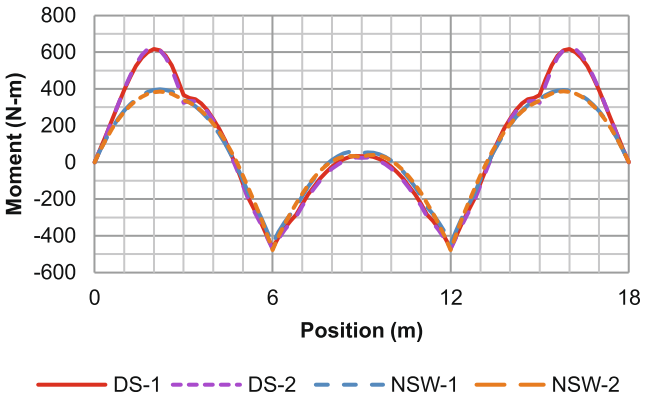

Fig. 11. Principal weak axis moment from vertical loading along 4th purlin. Position = 0 is the left side of Fig. 8a.

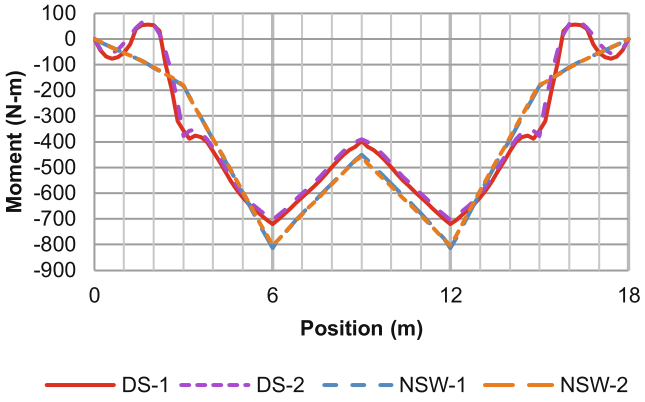

Fig. 12. Geometric weak axis moment from uplift loading along 4th purlin. Position = 0 is the left side of Fig. 8a.

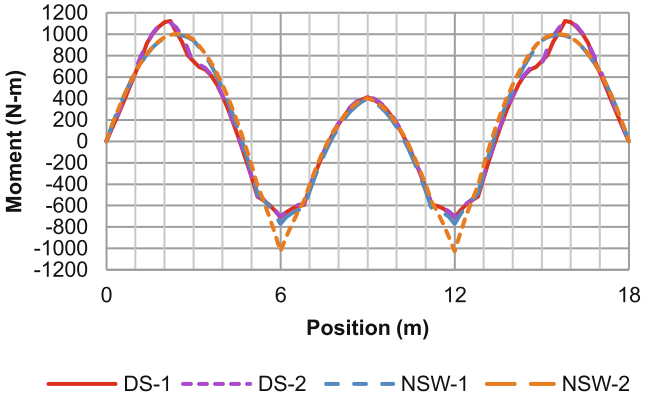

Fig. 13. Principal weak axis moment from uplift loading along 4th purlin. Position = 0 is the left side of Fig. 8a.

Table 4
Maximum distributed load applied [kN/m].

Case	DS-1	DS-2	NSW-1	NSW-2	Shells
Down	1.67	1.80	3.63	3.58	3.78
Uplift	1.80	1.92	3.99	4.03	3.42

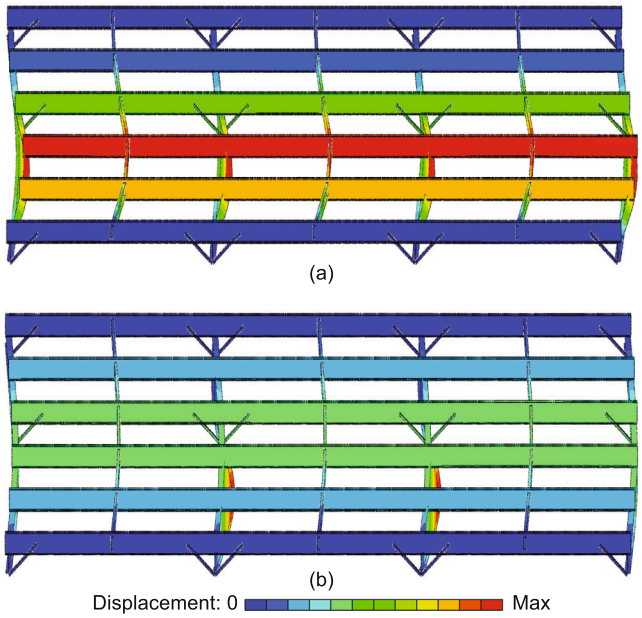

Fig. 14. Roof system with Z-Section purlins buckling (a) due to downward vertical load and (b) due to uplift.

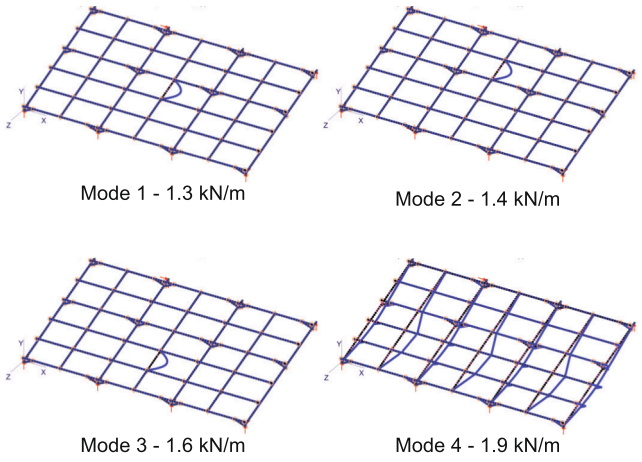

Fig. 15. First 4 buckling modes using doubly symmetric analysis for roof system with Z-Section purlins due to downward vertical load.

5. Roof System with Channel Purlins

5.1. Roof System Overview

The investigation into the roof system thus far has shown the importance of the appropriate evaluation of member stiffness to obtain accurate results. Prior results from an early part of this study [17] indicated that point symmetric Z-section variations could largely be attributed to warping stiffness effects. As such, it was desired to further investigate this system with channels to account for non-symmetric section properties related to a non-coincident shear center and centroid. As such, the single slope roof from the previous section was evaluated again with lipped channel purlins, 305Z51-300 M (1200C200-118), replacing the original Z-section purlins.

The updated roof system was evaluated for the application of a downward vertical load simulating dead/live loading and an upward load perpendicular to the roof slope to simulate wind loading. This loading was applied as a set of discrete point loads at the locations shown in Fig. 16 with an 'x'. The point loads were applied at the centroid

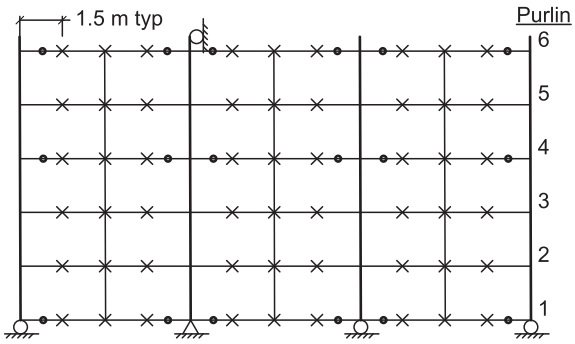

Fig. 16. Roof Point Load Location.

of the channel for two different loading cases. Case 1 considered a finite 1.5 kN load to establish a working load comparison point. Case 2 again considered the elastic stability limits of the consistent loading configuration.

5.2. Roof System Modeling Details

The updated roof system was modeled in line with the description in Section 4.2 with updates for the new purlin section and load distribution. The updated channel purlins were similarly modeled as prismatic and continuous members across the support beams with discrete bracing supports. The centroid of the purlin was assumed to remain constant despite the change in cross section.

In addition to the alterations described above, the other main modification to the line element models was to the NSW-2 model. An additional rigid link was defined to connect the origin of the section to the centroid where the point loads could be defined.

The shell element model was constructed similarly with the purlin to beam connections still located at the web. The first major update was to shift the channel and angle braces down the slope of the roof to align with the new web location. The other addition was a rigid tie over the height of the web at each point load location. Each tie was connected to the centroid where the point load could then be applied and distributed across the shell model.

5.3. Roof System Results

The primary results of interest are the same as for the roof with Z-purlins: the internal forces and displacements of members. To provide similar context on the level of loading, a demand capacity ratio is provided for the interaction of strong and weak axis moment. The necessary moment capacities were determined using the Direct Strength Method with a 3 m unbraced length.

The 1.5 kN point load case for channel purlins presented consistent results among the different structural analysis methods. Table 5 summarizes a sampling of the maximum vertical deflection of the beams, the vertical deflection at the centroid of the purlin, the moment applied to the supporting beams, and the demand capacity ratio for the purlins considering strong and weak axis bending. Overall, the new roof was exhibiting greater variability in the deflection of the purlins. The variation in the channel deformation between the doubly symmetric and more sophisticated analyses was attributed primarily to the introduction of different amounts of torsion in the different analyses. The more sophisticated analyses were able to capture the initial loading eccentricity resulting from the difference between the shear center and centroid that was absent in the doubly symmetric analyses.

Taking a closer look at the purlin, the moment diagrams again show variation between the different analysis methods. The strong axis moment was quite similar along the length of the purlin, but the doubly symmetric underestimated the maximum midspan moments as shown in Fig. 17. Similar to the Z-section, the more interesting behavior was

Table 5
Analysis Results for Roof System with 1.5 kN Point Loads.

Downward Loading					
Results	DS-1	DS-2	NSW-1	NSW-2	Shells
Beam Mx (N-m)	31214 (0.3%)	31239 (0.2%)	30821 (1.6%)	30545 (2.5%)	31315
Beam Uy (mm)	7.4 (7.5%)	7.4 (7.5%)	7.6 (5.0%)	7.7 (3.8%)	8.0
Purlin Uy (mm)	25.7 (7.5%)	25.6 (7.1%)	22.3 (6.7%)	28.9 (21%)	23.9
Purlin 1 Ratio	69.5%	68.6%	67.8%	75.8%	64.9%
Purlin 4 Ratio	69.4%	69.0%	67.7%	68.1%	70.5%
Uplift Loading					
Results	DS-1	DS-2	NSW-1	NSW-2	Shells
Beam Mx (N-m)	12667 (2.1%)	12660 (2.1%)	12666 (2.1%)	12690 (1.9%)	12934
Beam Uy (mm)	20.9 (2.3%)	20.7 (3.3%)	20.7 (3.3%)	20.7 (3.3%)	21.4
Purlin Uy (mm)	13.5 (4.9%)	13.4 (5.6%)	13.7 (3.5%)	17.5 (23%)	14.2
Purlin 1 Ratio	31.4%	31.3%	31.3%	32.8%	29.9%
Purlin 4 Ratio	33.8%	33.8%	33.9%	33.9%	35%

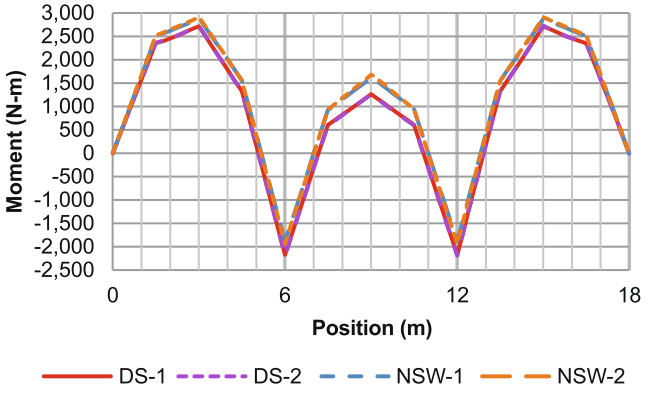

Fig. 17. Strong axis moment from vertical loading along the 5th purlin. Position = 0 is the left side of Fig. 16.

observed in the weak axis moment direction depicted for vertical loading in Fig. 18 and uplift in Fig. 19. Once again, the softer torsional stiffness in the doubly symmetric analyses are resulting in larger twisting of the cross section which causes larger second-order effects. In the fourth purlin, the doubly symmetric analyses was actually unconservative and completed missed a negative moment that developed near the applied load, shown in Fig. 20. Overall, the largest variations in the moments in the purlin were observed in the outer section between the

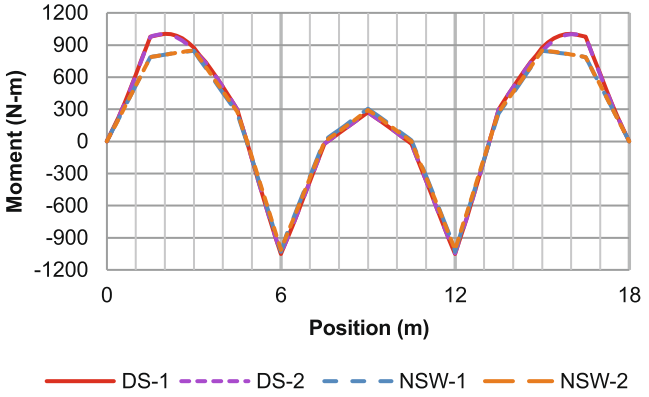

Fig. 18. Weak axis moment from vertical loading along 5th purlin. Position = 0 is the left side of Fig. 16.

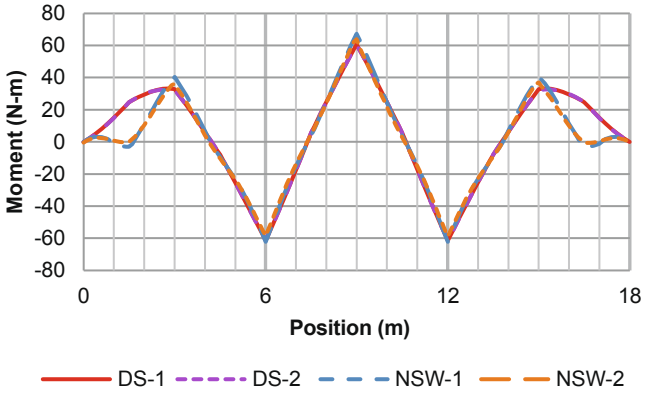

Fig. 19. Weak axis moment from uplift loading along 5th purlin. Position = 0 is the left side of Fig. 16.

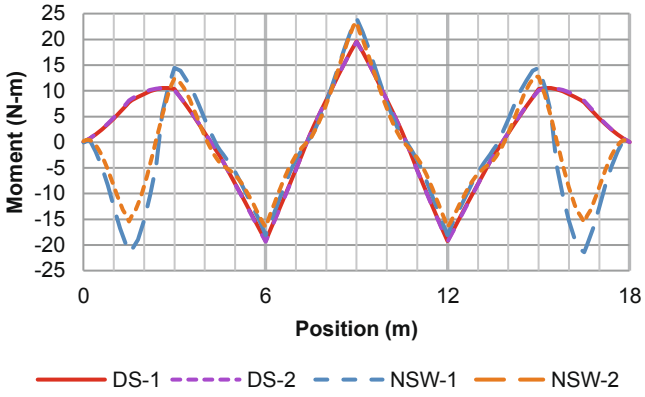

Fig. 20. Weak axis moment from uplift loading along 4th purlin. Position = 0 is the left side of Fig. 16.

last brace and the final support, especially in the weak axis.

When evaluating the roof system for elastic stability, the channel purlins are susceptible to lateral torsional buckling failures under

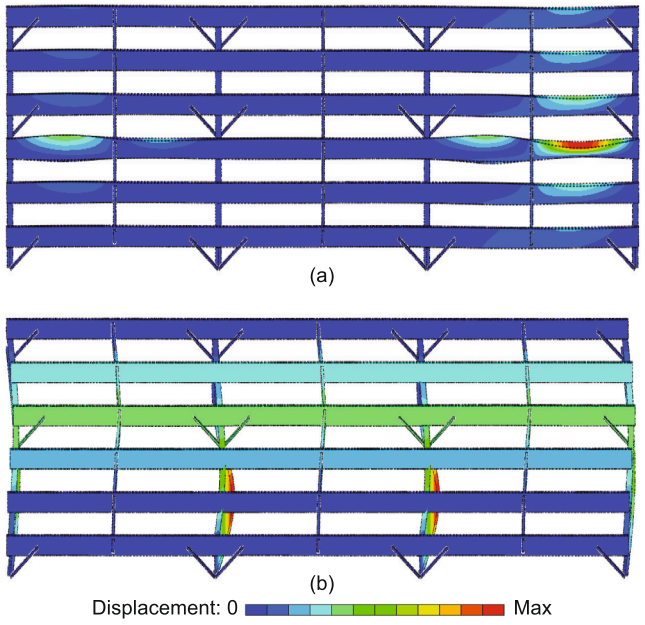

Fig. 21. Roof system with channel purlins buckling (a) due to downward vertical load and (b) due to uplift.

vertical loading first while the uplift case is still controlled by the support beam as depicted in Fig. 21. Once again, the different analysis methods indicated significant variations in the controlling response as summarized in Table 6 for the nonlinear static analysis. While completing the nonlinear evaluation of NSW-1 and NSW-2, both methods captured nonlinearly increasing deflections prior to the controlling failure of the roof system which was a global lateral response similar to the example in Section 4. A closer look comparing the displacement with the eigenbuckling behavior provided content for the apparent disagreement in buckling response noted in Fig. 21(a). The eigenbuckling evaluation using NSW-1 indicated 10 different purlin buckling modes between 6.1 kN and 7 kN where a system buckling response was observed. These buckling modes represented various deflection patterns in the purlins that canceled and amplified each other. Approaching this lower limit, localized large changes to the deflection pattern occurred; however, additional load could still be readily applied to the system. Only upon reaching the lateral beam buckling mode did the system fail.

The numerous purlin buckling modes caused difficulties in determining a stability limit for the nonlinear shell element analysis. In the shell evaluation, it was not possible to immediately determine the next stable orientation at the given load due to the purlin behavior, and as such required an arc length evaluation to gradually transition to the next stable orientation. The channels starting to buckle caused the outer support beams to move slightly laterally and a local rotation of a purlin. The nonlinear analysis was able to evaluate this behavior through two regions of brief negative stiffness until a stable configuration was found and the total applied loading increased. During the third iteration of this behavior, the analysis failed due to a near zero stiffness at the transition to a positive stiffness with small time steps resulting in the maximum value shown.

Similar to the previous example in Section 4, the doubly symmetric analyses encountered a premature failure due to buckling of the channel braces. Once the braces began reaching their maximum load, the channel purlins began to deflect more which lead to failure.

6. Discussion

The evaluation of structural systems requires accounting for the appropriate load sharing and deformation of the components. The inclusion of non-symmetric cross sections complicates this evaluation with more complex behavior including significant twisting effects in most applications. As shown in Section 3.3 with the modeling of the portal frame, a different structural response could be observed between the doubly symmetric and non-symmetric analyses when the channels were only laterally supported. With the channels more free to move, different deformations existed not only out-of-plane, but in-plane as well. When the channels were torsionally restrained by the addition of interior lateral supports, the variation in the deflection of the system nearly disappeared. While some torsion was still applied with exterior and interior lateral supports, the available restraints limited the ability of non-symmetric sections to move and helped to constrain the response to a single plane which improved agreement for the doubly symmetric analyses. However as loading and deflection increases, variations will begin to appear as observed in Fig. 13 where the different torsion behaviors caused incorrect secondary weak-axis loading. This variation is at an extreme when considering the higher loading associated with elastic stability in the roof examples. Despite the agreement among the different analysis methods at the lower applied discrete load, eventually the applied load caused the inherent variations in the underlying models to start controlling the overall response resulting in significant differences. The proper consideration of non-symmetric section properties becomes a critical factor under larger loading.

The response of a structural system with non-symmetric behavior could not be readily predicted due to the interaction of competing factors. As a consequence, the results of a doubly symmetric analysis including these sections could not easily be determined to be conservative or unconservative. In the roof system examples, the doubly symmetric analyses were slightly conservative at the lower loading levels. The softer twisting response in these non-symmetric sections resulted in minimal differences at the lower load level. When evaluating the stability of the system, the softer twisting response caused premature elastic failure at half the value of the expected ultimate load. In contrast, the doubly symmetric results of the portal frame captured an unconservative stiffer response than is expected. In this instance, the softer twisting response from ignoring warping did not cause larger rotations as it was accompanied with an underestimation of the additional torsional loading by not considering the shear center position. This localized interaction can often be readily discussed after the fact; however, quantifying how significant each factor is beforehand is challenging. As is, the most consistent ways to predict the response of a non-symmetric section to loading is either to directly account for the non-symmetric behavior or to directly limit the twist of the member to improve doubly symmetric predictions.

Table 6
Maximum point load applied [kN].

Case	DS-1	DS-2	NSW-1	NSW-2	Shells
Down	3.0	3.2	7.1	6.9	6.3
Uplift	2.9	3.2	7.7	7.5	7.5

7. Conclusion

Comparisons are made with finite element analysis programs that use various formulations to model two structural systems with non-symmetric cross sections. As previous work showed the ability of these analysis methods to accurately model minimum structural analysis requirements, this investigation was able to focus on more complex examples including structural systems. Evaluation of these examples highlighted the importance of the interacting twist and non-symmetric properties through the entire structural system. While specific components of the result could occasionally be attributed to the underlying model assumptions, it was difficult to predict the cumulative effect of the excluded behavior. The more freedom an element had to rotate the more critical it was to capture the true behaviour of non-symmetric response. This interaction was amplified when the loading increased causing greater deformations. Torsional restraint of non-symmetric cross sections was identified as a significant factor in achieving an appropriate response with a simplified analysis, but no specific recommendation was developed. As a result, it is recommended that additional guidance be developed and provided to engineers as to when the effects of twisting and non-symmetric section properties should be included in structural analysis.

CRediT Author Statement

Edward J. Sippel: Conceptualization, Methodology, Validation, Formal Analysis, Investigation, Writing - Original Draft, Visualization. **Hannah B. Blum**: Conceptualization, Methodology, Supervision, Writing - Review & Editing.

Data Availability Statement

The data that supports the findings of this study are available from the corresponding author upon reasonable request.

Funding Statement

Support for this research was provided by the University of Wisconsin - Madison Office of the Vice Chancellor for Research and Graduate Education with funding from the Wisconsin Alumni Research

Foundation.

Declaration of Competing Interest

The authors declare that they have no known competing financial interests or personal relationships that could have appeared to influence the work reported in this paper.

Acknowledgements

The authors would like to thank Professor Ronald Ziemian at Bucknell University and Dr. Siwei Liu and his research team at the Hong Kong Polytechnic University for their assistance with the updated MASTAN2 program.

References

[1] AISI. S100–16, North American Specification for the Design of Cold-Formed Steel Structural Members. Washington, DC, U.S.A: AISI; 2016.
[2] Ziemian RD, Batista Abreu JC, Denavit MD, Denavit T-JL. Three-Dimensional Benchmark Problems for Design by Advanced Analysis: Impact of Twist. J. Struct. Eng. 2018;144:04018220. https://doi.org/10.1061/(asce)st.1943-541x.0002224.
[3] AISC. Specification for Structural Steel Buildings ANSI/AISC 360–16. Chicago, IL: American Institute of Steel Construction; 2016.
[4] Bernuzzi C, Gabbianelli G, Gobetti A, Rosti A. Beam design for steel storage racks. J. Constr. Steel Res. 2016;116:156–72. https://doi.org/10.1016/j.jcsr.2015.09.007.
[5] Kim N-I, Kim M-Y. Exact dynamic/static stiffness matrices of non-symmetric thin-walled beams considering coupled shear deformation effects. Thin-Walled Structures 2005;43:701–34. https://doi.org/10.1016/j.tws.2005.01.004.
[6] Bernuzzi C, Pieri A, Squadrito V. Warping influence on the static design of unbraced steel storage pallet racks. Thin-Walled Struct. 2014;79:71–82. https://doi.org/10.1016/j.tws.2014.01.024.
[7] Rinchen, G.J. Hancock, K.J. Rasmussen, Formulation and Implementation of General Thin-Walled Open- Section Beam-Column Elements in Opensees Research Report, Technical Report, The University of Sydney, Sydney, Australia, 2016.
[8] Liu S-W, Ziemian RD, Chen L, Chan S-L. Bifurcation and large-deflection analyses of thin-walled beam-columns with non-symmetric open-sections. Thin-Walled Struct. 2018;132:287–301. https://doi.org/10.1016/j.tws.2018.07.044.
[9] Liu S-W, Gao WL, Ziemian RD. Improved line-element formulations for the stability analysis of arbitrarily-shaped open-section beam-columns. Thin-Walled Struct. 2019;144:106290. https://doi.org/10.1016/j.tws.2019.106290.
[10] R.D. Ziemian, W. McGuire, S.-W. Liu, MASTAN2 v5.0.2, 2019.
[11] Trahair NS. Flexural-Torsional Buckling of Structures. 1st ed.,. London; New York: Spon; 1993. https://doi.org/10.1201/9781482271218.
[12] Shayan S, Rasmussen KJ. A model for warping transmission through joints of steel frames. Thin-Walled Struct. 2014;82:1–12. https://doi.org/10.1016/j.tws.2014.03.017.
[13] Sapountzakis EJ, Dikaros IC. Advanced 3-D beam element including warping and distortional effects for the analysis of spatial framed structures. Eng. Struct. 2019;188:147–64. https://doi.org/10.1016/j.engstruct.2019.03.006.
[14] Hansen AB, Jönsson J. Modelling of steel frames using advanced beam and joint elements with interfaces governed by beam modes. Thin-Walled Struct. 2019;145. https://doi.org/10.1016/j.tws.2019.106430.
[15] G.J. Hancock, Portal Frames Composed of Cold-Formed Channel- and Z-Sections, in: R. Narayanan (Ed.), Steel Fram. Structrues - Stab. Strength, 1 ed., CRC Press, 1990, pp. 241–276.
[16] Rinchen KJ, Rasmussen H. Zhang, Design of cold-formed steel single C-section portal frames. J. Constr. Steel Res. 2019;162:105722. https://doi.org/10.1016/j.jcsr.2019.105722.
[17] Sippel EJ, Ziemian RD, Blum HB. Analysis of non-symmetric cross-sections relative to the provisions of AISC 360-10. Struct Stab Res Counc 2020 Annu Stab Conf 2020;1:1–28.
[18] CSI America, SAP2000 v. 20.1.0, Computers & Structures Inc, Berkeley, CA, 2018.
[19] Dlubal, RFEM v. 5.19, Dlubal Software GmbH, 2012.
[20] Dassault Systems, Abaqus/CAE vol 6.16, Dassault Systems, Johnston, RI, 2015a.
[21] Dassault Systems, Abaqus 2016 Documentation, 2015b. http://130.149.89.49:2080/v2016/index.html.
[22] Baigent AH, Hancock GJ. Structural analysis of assemblages of thin-walled members. Eng. Struct. 1982;4:207–16. https://doi.org/10.1016/0141-0296(82)90010-4.
[23] Baigent AH. Thin-Walled Structural Systems. Ph.D. thesis. The University of Sydney; 1980.
[24] Baigent AH, Hancock GJ. The Stiffness and Strength of Portal Frames Composed of Cold-Formed Members. Civ. Eng. Trans. 1982;24:278–83.
[25] Sputo T, Haynes J, Ellifritt DS. Flexural Capacity of Discretely Braced C's and Z's, 11th Int. Spec. Conf. Cold-Formed Steel Struct. 1992;2:109–29. https://scholarsmine.mst.edu/isccss/11iccfss/11iccfss-session3/2.
[26] Epstein HI, Murtha-Smith E, Mitchell JD. Analysis and design assumptions for continuous cold-formed purlins. Pract. Period. Struct. Des. Constr. 1998;3:60–7. https://doi.org/10.1061/(ASCE)1084-0680(1998)3:2(60).
[27] S. Wang, R.S. Glauz, B.W. Schafer, Inelastic Lateral-Torsional Buckling Strength Validation for Non-Principal Axis Bending Using Numerical Methods, Technical Report, 2020.

Engineering Structures 259 (2022) 114126

Contents lists available at ScienceDirect

Engineering Structures

journal homepage: www.elsevier.com/locate/engstruct

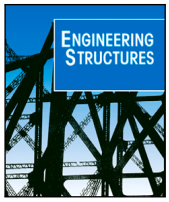

Machine learning-based sensitivity of steel frames with highly imbalanced and high-dimensional data

Hyeyoung Koh, Hannah B. Blum *

Department of Civil and Environmental Engineering, University of Wisconsin - Madison, WI, United States

ARTICLE INFO

Keywords:
Machine learning
Feature importance
Imbalanced classification
High-dimensional data
Sensitivity analysis
Steel structures

ABSTRACT

The machine learning-based feature selection approach is presented to estimate the effect of uncertainties and identify failure modes of structures that incorporate a low failure probability and high-dimensional uncertainties. As structures are designed to have few failures, a dataset classified based on the failure status becomes imbalanced, which poses a challenge for the predictive modeling of machine learning classifiers. Moreover, in order to improve the accuracy and efficiency of the model performance, it is necessary to determine the critical factors and redundant factors, especially for a large feature set. This study benchmarks the novel method for sensitivity analysis by using datasets that exacerbate the problems involved in class imbalance and large number of input features. This study investigates two planar steel frames with spatially uncorrelated properties between structural members. Geometric and material properties are considered as uncertainties, such as material yield stress, Young's modulus, frame sway, and residual stress. Six feature importance techniques including ANOVA, mRMR, Spearman's rank, impurity-based, permutation, and SHAP are employed to measure the feature importance and identify parameters germane to the prediction of structural failures. Logistic regression and decision tree models are trained on the important feature set, and the predictive performance is evaluated. The use of the feature importance approach for structures with a low probability of failure and a large number of uncertain parameters is validated by showing identical results with the reliability-based sensitivity study and appropriate predictive accuracy.

1. Introduction

Structures have numerous variations and uncertainty in their properties, which may affect the load carrying capacity. A reliability-based sensitivity analysis estimates how uncertainty in the input parameters affects system performance by analyzing the dependence of the failure probability on the inputs, which requires repeated evaluation of the performance function, resulting in significant computational cost and time. This challenge is exacerbated for large-scale engineering problems which often carry a large quantity of uncertain parameters, which for machine learning is referred to as a large dimension in a dataset. Researchers have made efforts to improve the computational efficiency of sensitivity analysis. For example, Wu [1] proposed the adaptive importance sampling approach, which improves computational efficiency by minimizing oversampling in the safe region of the limit-state surface. The score function approach proposed by Rubinstein and Kroese [2] estimates all sensitivities by the gradient and derivative of parameters. The score function method does not require additional simulations for reliability sensitivity analysis. Torii et al. [3] applied polynomial expansions to the performance function and its derivatives for the probability of failure sensitivity analysis. Proppe [4] introduced the local reliability sensitivity analysis using the moving particles method, which estimates the failure probability based on the new locations of the moved data points in the design space.

For high-dimensional data, it is difficult to make a right decision on which features should be selected because of the curse of dimensionality [5], which refers to the phenomenon arising from too many feature variables that increase sparsity in data, storage space, and computational costs. The principal component analysis (PCA) [6,7] is commonly used to mitigate high-dimensionality. However, PCA reduces the dimension by utilizing the correlation structure of random variables, thus it does not perform well for independent variables. Feature selection is one of the most crucial techniques in machine learning especially for high-dimensional datasets [8] because it can filter out redundant or irrelevant features. The success of feature selection techniques, which enables meaningful predictors to be obtained and derives results faster, has been proven by many researchers in various fields of study [9–12]. However, the high-dimensional problems often accompany

* Corresponding author.
E-mail addresses: hyeyoung.koh@wisc.edu (H. Koh), hannah.blum@wisc.edu (H.B. Blum).

https://doi.org/10.1016/j.engstruct.2022.114126
Received 2 September 2021; Received in revised form 2 March 2022; Accepted 8 March 2022
Available online 30 March 2022

other issues emerging from the nature of data, such as imbalanced classification [13,14]. Class imbalance refers to a problem in machine learning classification where each class accounts for an unequal portion of the data, which may lead to poor predictive performance. If a classifier is applied on an imbalanced dataset, the classifier is biased towards the majority class [15] and a trivial classifier learns the majority class only and attributes the label to all instances, thereby no instance for predicted minority class occurs [16]. As the failure probability of structures can be estimated by the number of failures (minority class) out of the total number of simulations including failure and safe structures (majority class), datasets for structural design problems become extremely imbalanced. When a structure is designed to have little load redistribution, the target reliability index β_T is 2.7 [17], which corresponds to the failure probability P_f of 3.5×10^{-3}, derived from $\beta = -\Phi^{-1}(P_f)$, where Φ^{-1} = inverse standard normal cumulative density function. Moreover, ASCE 7 [18] suggests using a target reliability index between 3.0 and 4.0 for structural components subjected to dead, live, and other loads except earthquake loads, depending on the risk category from I through IV where category I represents the lowest level of risk to human life. Likewise, a classification dataset for structural design problems will be severely imbalanced, which is indicated from the values of β_T and P_f. As structural design problems often include an imbalanced dataset, it is challenging to select an adequate statistical metric that provides informative and truthful results. This emphasizes that the use of feature selection techniques on structural engineering data with high-dimensionality and class imbalance should be explored, in which there are rather limited studies.

In recent years, the interest in artificial intelligence has been growing in the field of structural engineering because it provides efficient solutions to the problems in this field relative to traditional computational techniques. The use of artificial intelligence in steel structural design has been focused on artificial neural networks for design of steel members or connections such as compression members [19], steel panels [20], steel connections [21,22], and cold-formed steel channels [23]. For reinforced concrete (RC) members or systems, machine learning techniques are implemented to predict structural responses such as the shear capacity of fiber RC beams [24], structural response of RC deep beams [25], RC slabs [26], and RC columns under fire resistance [27]. Data-driven machine learning approaches were used for fragility, risk, and vulnerability assessment of a special steel moment resisting frame building [28,29] and RC building frames [30]. Also, machine learning approaches were used to identify failure modes and rank the significant factors affecting the failure mode of RC members [31], RC frames [32], and steel frames [33]. Data-driven design approaches for structural design have recently been developed, but it is desirable to determine if the approaches are viable before they are implemented in practice. To that end, this study benchmarks feature selection techniques on the structural analysis data that incorporate a high imbalanced ratio, a larger set of uncertainties, and more data points. The importance of benchmark studies has been emphasized in the machine learning community [34,35]. Machines carry out tasks based on learning from a given dataset, therefore the best algorithm will not be the same for all the datasets [36]. Therefore, benchmarking of the feature importance approach must be accomplished to draw conclusions for the use of the approach in a wide range of structural systems.

Koh and Blum [33] introduced the machine learning-based feature selection framework for structural sensitivity analysis. This framework measures the feature importance of all parameters and ranks them to determine the important or redundant parameters for the prediction of system failure. Two planar steel frames were investigated with the consideration of uncertainties that affect steel frame behaviors, such as yield stress, Young's modulus, frame sway, and residual stress. The frames have different failure modes and the ultimate frame strength obtained from finite element analysis was used as the response variable. The feature rankings derived by four feature importance techniques showed identical order of factors resulting in the largest failure probability, which matched those obtained from the conventional sensitivity analyses. It was demonstrated that the general procedure of the proposed feature importance method can be used for sensitivity analysis. The approach is efficient because all feature importances are estimated from a single training. Moreover, variable space can be reduced by removing irrelevant parameters to improve both computational efficiency and accuracy.

The steel frames investigated in this study have the same layout as for Koh and Blum [33] but have a different spatial correlation scenario. Unlike the correlated scenario where all columns (or beams) have the same properties, this study applies the uncorrelated scenario where all structural members have different properties. Sensitivity studies on structural systems with uncorrelated properties inform which specific structural member largely influences the frame failure. However, the increased number of uncertainties poses additional challenges in performing reliability sensitivity studies, which require repeated evaluations of the performance function. Regarding the feature importance approach, a large set of uncertainties would make it difficult for the feature importance method to derive consistent rankings between various techniques. In general, the uncorrelated scenario contains a fewer number of failures than the correlated scenario [37], therefore the class-imbalanced ratio increases for the uncorrelated scenario. This study aims to examine how the feature importance approach performs for a structural sensitivity analysis when fitting high-dimensional and extremely class-imbalanced data, which presents challenges in model training for structural engineering problems.

This study implemented six existing feature importance methods to measure the importance score. There are typically two categories in feature importance methods: (i) data analysis techniques that directly analyze the data without model fitting to measure the feature importance and (ii) model analysis techniques that identify important features based on predictions from trained models [38]. (1) ANOVA (Analysis of variance), (2) mRMR (minimal-redundancy–maximal-relevance) [39], and (3) Spearman's rank correlation coefficient [40] are utilized as data analysis techniques. This study used a decision tree classifier [41] to measure the feature importance by using model analysis techniques. Model analysis techniques include two feature importance methods, which are (4) impurity-based importance and (5) permutation importance, and (6) SHAP (SHapley Additive exPlanations) [42]. Based on the measured feature importance, logistic regression [43] and decision tree [41] models are fitted to predict whether a steel frame fails. The predictive performance is evaluated by specificity, recall, and the Matthews correlation coefficient [44]. The results are compared with the reliability-based sensitivity analysis results to validate the feature importance framework. Finally, the best feature importance technique depending on the failure modes is discussed.

2. Machine learning techniques for the feature importance approach

The primary task of this study is to estimate the effect of uncertainties on failure modes of steel frames using the machine learning-based feature importance approach. In a high-dimensional dataset, it is important to determine the relevant features and remove the redundant features in an effort to prevent overfitting of a model and reduce training time, thereby improving the model performance and computational efficiency. This study measures the feature importance and compares the critical features between the feature selection methods. Once the feature rankings are derived from the feature importance techniques, a classification model is employed to predict the failure status of a structure by increasing the size of the feature set used for training. The model accuracy of each feature importance method is measured to determine how many features are informative or irrelevant for identifying structural failures. The feature ranking as well as the model performance are considered when evaluating the feature importance techniques for structural sensitivity analysis.

2.1. Feature importance techniques

Feature selection involves reducing the number of feature variables to mitigate the curse of dimensionality. Feature selection improves the computational efficiency of the machine learning model and reduces the volume of feature space, which is a significant issue in a large dataset. Moreover, the prediction performance can be improved by removing redundant features that have a negative or no effect on prediction. There is a large number of feature selection techniques that estimate a feature importance score and provide the feature ranking based on the score of all features. This study implemented four existing feature importance methods to identify the most and least important features in steel structures.

2.1.1. ANOVA

The ANOVA test compares the relationship between features and response variables based on the value of F-statistic. The feature importance score J_{ANOVA} is equal to the value of F-statistic. The score can be calculated by Eq. (1):

$$J_{ANOVA}(x_i) = \frac{\sum_{m=1}^{M} N_m(\bar{x}_m^{(i)} - \bar{\bar{x}}^{(i)})/(M-1)}{\sum_{m=1}^{M}(N_m - 1)s_m^2/(N-1)} \tag{1}$$

where N_m = the number of instances that $y = m$, $\bar{x}_m^{(i)}$ = the sample mean of feature x_i for class m, s_m^2 = the sample variance of feature x_i for class m, $\bar{\bar{x}}^{(i)}$ = the grand mean of feature x_i, M = the number of classes, $M = 2$ in a binary dataset, N = the total number of instances. The importance score is the ratio of between-group variance to within-group variance, thus this technique assesses the difference between the mean values of the corresponding feature x_i between the classes. A higher value of the F-statistic indicates a larger difference between the mean values among the classes, thus the feature has a significant effect on the classes. Note that ANOVA is always positive because it is based on variance, which is always positive.

2.1.2. mRMR

The mRMR technique [39] ranks features by mutual information, which considers both relevance and redundancy of features. The feature relevance indicates a correlation with the response variable, and the feature redundancy represents the information duplicated between features. As the dataset is discrete not continuous, the mutual information difference (MID) is used as the mRMR criterion, which can be estimated by Eq. (2):

$$J_{mRMR}(x_i) = I(x_i, y) - \frac{1}{|S|}\sum_{x_j \in S} I(x_i, x_j) \tag{2}$$

where $|S|$ = the feature set size (number of features), S = a feature set, x_j = a feature not selected in the set S, and I = the mutual information. The first term represents the relevance of the feature x_i about the response variable y. The relevance is determined from the outcome variable prediction. The second term estimates the redundancy, which is measured within the selected features x_i and x_j. By intuition, a feature with a negative J_{mRMR} value has a small relevance and large redundancy, therefore, including it in model training would decrease the predictive performance of the model.

2.1.3. Spearman's rank

The Spearman's rank correlation coefficient [40] measures a monotonic nonlinear relationship between two variables, a feature x_i and the response variables y. The measured coefficient varies between −1 as the perfect negative correlation and +1 as the perfect positive correlation. A feature with the largest absolute value is considered the most important.

2.1.4. Impurity-based importance

Impurity-based importance considers the node impurity in a tree to estimate the importance. A node containing instances of one class only is pure while a node with greater than or equal to two classes is impure. The impurity-based feature importance can be computed by Eq. (3) [45], which measures the impurities at a node j before and after splitting and then averages the impurity decrease by $N^{(i)}$, which is the number of nodes in a tree split based on x_i. A negative feature importance value ($J_{impurity}$) indicates that including it in model training would decrease the predictive performance of the model.

$$J_{impurity}(x_i) = \frac{\sum_{i \in N^{(i)}}(\text{Impurity before node } k - \text{Impurity after node } k)}{|N^{(i)}|} \tag{3}$$

2.1.5. Permutation importance

Permutation importance measures the importance by removing a single feature column in a dataset. First, a tree-based algorithm is fitted to obtain the baseline model performance. After training the model, a single feature column is randomly shuffled to remove the association between the feature and the response variable. The performance of the permuted model is evaluated and compared with the baseline model performance. The difference in accuracy is considered to be the importance score as shown in Eq. (4). The feature that results in the largest Mean Decrease in Accuracy (MDA) is the most important. The permutation method provides a negative score when a feature has no effect and shuffled data are shown to be more accurate.

$$\begin{aligned} J_{permutation}(x_i) = {} & \text{accuracy for dataset without permutation} \\ & - \text{accuracy for permuted dataset of } x_i \end{aligned} \tag{4}$$

2.1.6. SHAP

The SHAP algorithm [42] identifies how much each feature contributes to the response variable based on the predictions for linear models trained on all feature subsets. The difference of the predictions from the model $f_{S\cup\{i\}}$ trained on a feature subset S including a feature x_i and another model f_S excluding x_i is interpreted as the effect of x_i. The SHAP importance score is a weighted average of all possible differences, as shown in Eq. (5):

$$J_{SHAP}(x_i) = \sum_{S \subseteq F \setminus i} \frac{|S|!(|F| - |S| - 1)!}{|F|!}[f_{S\cup\{i\}}(x_{S\cup\{i\}}) - f_S(x_S)] \tag{5}$$

where F = the set of all features, and S = all feature subsets without x_i. Since all possible subsets are used to measure the SHAP score, the computation time of the SHAP algorithm is expensive because the model is repeatedly trained on all possible feature subsets. SHAP measures the influence of features in terms of the prediction of either positive (minority class) or negative (majority class) outcomes.

2.2. Classification-based techniques

Two classification models from different classification model families were used to evaluate the performance. The selected models are logistic regression [43] from the regression-based classifier family and a decision tree [41] from the tree-based classifier family. Decision tree and logistic regression classifiers are fast and use a small amount of memory for training and prediction [46], indicating that they are appropriate for high-dimensional data and easy to use and interpret [47].

2.2.1. Logistic regression

Logistic regression [43] is trained using the top-k features obtained from the feature importance methods, where k = the number of important features. Logistic regression is used for the classification problems, which uses the logistic sigmoid function and transforms the output into a probability value between 0 and 1 as follows in Eq. (6):

$$P(Y = m) = \frac{1}{1 + \exp(-(w_0 + \sum_{i \in n} w_i x_i))} \tag{6}$$

where $P(Y = m)$ is the probability of presence of Class m; Class 0 represents no failure and Class 1 represents failure in this study, w_i = regression coefficients, x_i = input features, and n = the number of input features.

A linear function is embedded in the logistic regression model, which is given as the natural logarithm of the ratio of $P(Y = 1)$ to $P(Y = 0)$. Logistic regression estimates the regression coefficients by minimizing the value of the ratio shown in Eq. (7).

$$\log\left(\frac{P(Y=1)}{1-P(Y=1)}\right) = \log\left(\frac{P(Y=1)}{P(Y=0)}\right) = w_0 + \sum_{i\in n} w_i x_i \tag{7}$$

Feature scaling was performed on the datasets used for training a logistic regression classifier, which is sensitive to the location of data points. A decision tree is scale-invariant because it trains the model based on decision rules. Therefore, the datasets for the logistic regression algorithm are transformed to a standardized scale, which has a mean value = 0 and standard deviation = 1.

2.2.2. Decision tree

A tree-based classifier, decision tree [41], is used to measure the performance in addition to estimate the feature importance score of the model analysis techniques including impurity-based, permutation, and SHAP. Decision tree continuously splits the data according to a certain parameter such as impurity or entropy. Decision rules for splitting and the leaf nodes are the final outcomes of the decision tree. The decision tree algorithm used in this study splits the nodes based on entropy (Eq. (8)) until all leaves are pure:

$$H(S) = -\sum_{m=1}^{M} p_m \log_2 p_m \tag{8}$$

where M = the number of classes and p_m = the probability of Class m occurring in the data.

2.3. Evaluation metric

After training a model with a training set, the model performance is evaluated by using a test set, which was not involved in training. A confusion matrix provides a visualization of the model performance and it is used as a performance measurement for a machine learning classification problem. The confusion matrix for binary classification consists of the four different cases as shown in Eq. (9):

$$M = \begin{pmatrix} TP & FN \\ FP & TN \end{pmatrix} \tag{9}$$

where True Positive (TP) = the number of actual positives that are correctly predicted positives, True Negative (TN) = the number of actual negatives that are correctly predicted negatives, False Negative (FN) = the number of actual positives that are incorrectly predicted negatives, and False Positive (FP) = the number of actual negatives that are incorrectly predicted positives.

Several statistical rates can be computed based upon the values given in the confusion matrix. For example, Accuracy is defined as the ratio of the correctly predicted instances to all the instances, $(TP + TN)/(TP + TN + FP + FN)$. F1-score represents the harmonic mean of precision and recall, where precision is $TP/(TP + FP)$ and recall is $TP/(TP + FN)$. Accuracy and F1-score are the most popular metrics, but they lead to the overoptimistic inflated measures especially on imbalanced datasets [48] because several classifiers learn towards the majority class [15,16]. For instance, when a dataset has 0.01% minority class and a model predicts all minority classes incorrectly, i.e., all data points are classified as the majority class, the model accuracy is 99.99%, which is nearly perfect. In structural engineering practice, however, it is critical to identify structural failures (the minority class) rather than safe structures (the majority class), thereby necessitating using the right metric that can correctly predict both classes in a binary classification.

This study employed three statistical measures to evaluate the performance including specificity, recall, and the Matthews correlation coefficients (MCC) [44]. For imbalanced class distributions, the majority class is typically referred to as the negative outcome and the minority class is assigned to the positive outcome. Therefore, structural failure is the positive outcome and no failure is the negative outcome. Specificity is the probability that an actual negative will test negative and is calculated by $TN/(TN + FP)$, which is the true negative rate. Specificity refers to how well a model identifies the frames which have no failure. Recall, also called the true positive rate, is the ratio of correct positive predictions to the total positive examples and is computed by $TP/(TP + FN)$. Recall informs how many positive predictions are missed from the prediction. The MCC is a reliable measure for imbalanced classification problems because it takes into account the ratio between positive and negative outcomes, which are not considered in both specificity and recall. The MCC is independent of the class imbalance, thus can reduce misleading results on imbalanced datasets [16]. The value of MCC varies between −1 and 1, similar to other correlation coefficients. The score is high only when all four categories in the confusion matrix are generated correctly. The MCC is computed by:

$$MCC = \frac{TP \cdot TN - FP \cdot FN}{\sqrt{(TP + FP) \cdot (TP + FN) \cdot (TN + FP) \cdot (TN + FN)}} \tag{10}$$

3. Reliability-based sensitivity analysis

Existing steel design specifications [49–52] provide guidance for inelastic analysis, also referred to as advanced analysis and GMNIA, which directly considers geometric and material nonlinearities and includes uncertainty in system, member, and connection strength and stiffness. Estimating structural performance with certainty is challenging because of the inherent uncertainty in a structural system which affects system performance. Reliability-based sensitivity analysis estimates the effect of an input variable by evaluating the structural performance with the variable under consideration as random while all other variables are at their nominal values. After repeated simulations for each property under consideration, the probability of failure P_f is estimated by n/N [53] where n = number of simulations which resulted in failure and N = total number of simulations. The system reliability index β is computed based on P_f. Unlike a reliability analysis which takes into account multiple random variables simultaneously, a sensitivity analysis considers only one random variable per simulation set to examine how the random variable affects the system behavior, therefore the strength distribution might have a smaller COV compared to that from a reliability analysis. The normal probability plot [54] is used to estimate P_f and β when no failure cases occur.

Researchers have investigated the system reliability of various steel structures estimated by considering uncertainties in the systems. Buonopane [55] conducted a reliability sensitivity study on two steel frames by considering uncertainties in yield strength, elastic modulus, residual stress, and sway and bow imperfections. Szyniszewski [56] investigated the effect of random geometric imperfections on progressive collapse propagation by analyzing 3-D steel framed buildings with uncorrelated geometric imperfections between structural members. Shayan et al. [57] presented a probabilistic study regarding modeling random geometric imperfections on regular and irregular sway and braced planar steel frames. Thai et al. [58] evaluated the system reliability of steel frames with semi-rigid connections. Uncertainties in gravity loads, material properties, cross-sectional properties, and connection properties were included in the reliability analysis. Zhang et al. [59] examined the system reliability of five steel structures including a beam, a portal frame, and three low-rise frames. Randomness considered in the analysis includes gravity loads, material properties, cross-sectional properties, and sway imperfection. Cardoso et al. [60] calibrated the system reliability of cold-formed steel portal frames with uncertain parameters in material properties, cross-section thickness, joint properties, and geometric imperfections.

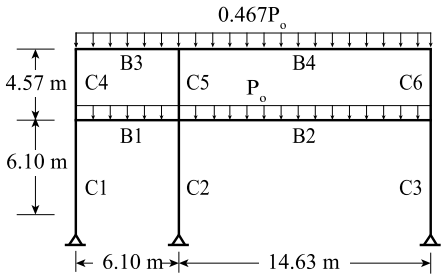

Fig. 1. Frame layout.

Table 1
Member sizes and applied loads.

Element	Frame 1	Frame 2
C1	W6 × 20	W12 × 14
C2	W14 × 82	W14 × 99
C3	W14 × 68	W14 × 82
C4	W6 × 8.5	W10 × 12
C5	W14 × 145	W14 × 109
C6	W14 × 145	W14 × 109
B1	W30 × 132	W27 × 84
B2	W36 × 182	W36 × 135
B3	W24 × 55	W18 × 40
B4	W30 × 116	W27 × 94
Loads (P_o)	111.86 kN/m	109.45 kN/m

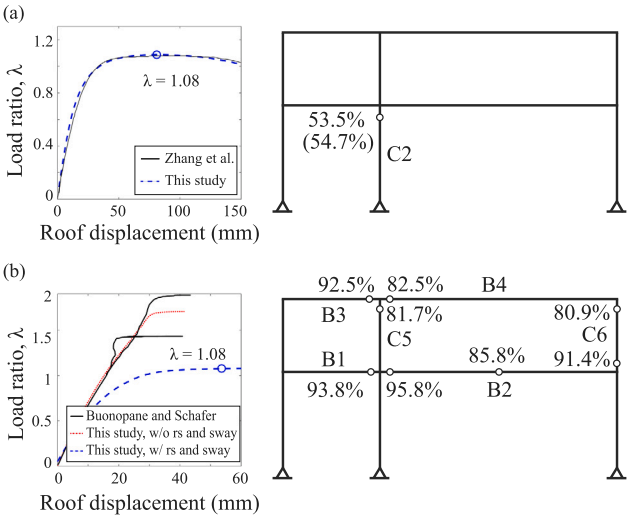

Fig. 2. Load–deformation curves and location of highly yielded zones: (a) Frame 1 (b) Frame 2. (For interpretation of the references to color in this figure legend, the reader is referred to the web version of this article.)

4. Data collection

4.1. Structural system

Two example steel frames designed according to AISC 360 [50] were analyzed in this study, which have the same layout but different member sizes and loads, adopted from [61]. Studies of these frames have been published in Zhang et al. [59] for Frame 1 and Buonopane and Schafer [62] for Frame 2. Fig. 1 and Table 1 summarize the details of the example frames including geometry and applied loads. The frames were modeled in OpenSees [63] with displacement-based and fiber-type elements, which were subdivided into 16 elements per member. Connections were assumed to be fully-rigid, thereby disregarding any potential flexibility in the connections. All cross-sections contained the residual stress with the Galambos and Ketter pattern [64] and the fiber distribution as shown in Fig. 3. The nominal peak compressive residual stress value was $0.3F_{yn}$, where F_{yn} = nominal material yield strength of 248 MPa (36 ksi). Initial sway imperfection of $h/500$ was given to all columns in the frame, where h is the story height.

Second-order inelastic push-down analyses were performed, in which the applied load ratio is increased until the frame collapses. The finite element (FE) analyses were first conducted with all nominal properties to determine the nominal ultimate load ratio λ, which is the ratio of ultimate to factored design loads. Fig. 2 illustrates the load–deformation curves and the location of highly yielded zones (≥ 75% of cross-sectional area yielded). The numbers represent the ratio of yielded cross-sectional area. The ultimate load ratios λ obtained from the analyses are 1.08 for both frames, which indicated that they have a limited capacity for load redistribution. Frame 1 failed by the instability (global inelastic buckling) of the slender ground floor column C2. Member C2 was partially yielded (53.5%) at the collapse limit, while the other members were within their elastic limits at failure, which matched the results presented in [59]. Frame 2 failed from a gradual sequence of yielding, whereby multiple members had highly yielded zones along the member length, which were B1, B2, B3, B4, C5, and C6.

To verify the accuracy of the FE models, the analysis output with nominal properties was compared to that from the previous studies [59, 62]. Load–deformation curves and yield ratios from Zhang et al. [59] and the model in this study (Frame 1) were well matched to each other as shown in Fig. 2a, where the number in parentheses indicates the yield ratio recorded from Zhang et al. [59]. Next, a reliability analysis considering the effect of uncertainties in geometric and material properties in addition to applied loads was also performed. The variations of the loads are provided in Ellingwood et al. [65]. The resulting β value was 2.79, which had an error of 1.4% with the β results from the previous study [59], thereby validating the model for Frame 1.

As for Frame 2, it was confirmed that the Frame 2 model can capture the load–displacement curve when it follows the model description provided in Buonopane and Schafer [62], where residual stresses and sway imperfections were not included. As shown in Fig. 2b, the model without consideration of residual stress (rs) and sway imperfections (red line) had a load ratio of 1.70, which is within the range between the maximum and the minimum load ratios of the Buonopane and Schafer results (black line). This validates the modeling approach for Frame 2 with the previously published results [62]. After validating the model with nominal properties, residual stresses and sway imperfections were added into the model for Frame 2 and the resulting load ratio was 1.08 (blue line). This indicates that residual stresses and sway imperfections influence the capacity of Frame 2.

4.2. Uncertainty

The Monte Carlo sampling method is used to generate samples of the uncertainties in material yield strength F_y, modulus of elasticity E, sway imperfection, and residual stress. Table 2 summarizes the statistical information of the uncertainties with referenced literature. Yield strength and elastic modulus are modeled following the distributions published in Bartlett et al. [66]. Nominal yield strength F_{yn} of 248 MPa and nominal elastic modulus E_n of 200 GPa are utilized to determine the mean value of yield strength and elastic modulus, respectively. The distribution of sway imperfection followed the distribution of Lindner and Gietzelt [67]. The scale factor of maximum compressive residual stress X is modeled as a normal distribution provided in Shayan et al. [68]. The random scale factor X was multiplied by $0.3F_{yn}$ to consider the uncertainty of residual stress magnitudes in compression.

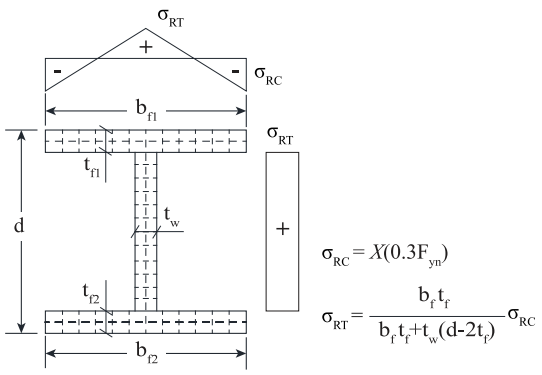

Fig. 3. Residual stress pattern and fiber distribution.

Table 2
Description of feature variables.

Variable	Mean	COV	Distribution	References
F_y	$1.1F_{yn}$	0.06	Lognormal	Bartlett et al. [66]
E	E_n	0.04	Lognormal	Bartlett et al. [66]
Sway imperfection	1/770	0.875	Lognormal	Lindner and Gietzelt [67]
X	1.064	0.27	Normal	Shayan et al. [68]

The peak tensile residual stress (σ_{RT}) within a cross section was determined by the geometry and the peak compressive residual stress (σ_{RC}), as shown in (Fig. 3). σ_{RT} includes X indirectly because it is calculated based on equilibrium. Once σ_{RC} and σ_{RT} are determined, the rest of the residual stresses in the cross section were set based on the residual stress pattern. The residual stress condition is constant along the length of a member. To account for the maximum number of uncertainties and to investigate the effect of each parameter on structural failure, the frames are assumed as spatially uncorrelated, i.e., all structural members have different random properties.

Cross-sectional imperfections, including web and flanges widths and thicknesses, were considered as random variables in preliminary studies using statistical information provided in Melcher et al. [69]. However, there were no observations of failure until 10^6 simulations were performed. An extremely small COV for the strength distributions occurred, likely due to the small COVs of the distributions of cross-section dimensions. This indicates a negligible effect of randomness in cross-sectional dimensions on the studied planar frames.

4.3. Dataset

As the structural members are uncorrelated, each individual member had a different realization of the random properties. In other words, there were no identical random values of the input variables shared between all beams or all columns. Input feature variables consist of thirty-three different parameters including ten different values each of yield strength, elastic modulus, and residual stress and three sway imperfections assigned to the three column locations — left, center, and right. The response variable is the binary outputs based on the ultimate load ratio λ obtained from the FE analysis containing random realizations of the input parameters. As the frame is designed according to the inelastic method provided in AISC 360 [50], this study applied the probability-based limit state design criteria $\lambda = 1.0$ as the classification criteria of the dataset. If the ultimate load ratio is less than 1.0, the frame experiences a structural failure and the observation is assigned to Class 1. An ultimate load ratio greater than or equal to 1.0 indicates that the frame is safe and the sample set is assigned to Class 0, which means no failure. A total of 500,000 simulations were run for Frame 1 and 1,000,000 simulations for Frame 2. A small percent of simulations had convergence issues and were excluded from the datasets. In total, Frame 1 had 309 failures (Class 1) out of 498,050 labeled data points. Frame 2 had 127 failures, which is less than that of Frame 1, out of the total number of simulations, 903,272.

As discussed previously, a classification dataset for structural design problems will be severely imbalanced, based on the selection of β_T and the corresponding P_f. A no-information rate, which describes how much the dataset is imbalanced, is calculated by $\max(n_{Class\,0}, n_{Class\,1}) / (n_{Class\,0} + n_{Class\,1})$, where $n_{Class\,0}$ is the number of Class 0 examples and $n_{Class\,1}$ is the number of Class 1 examples. Therefore, the no-information rates of Frame 1 and Frame 2 are 99.94% and 99.99%, respectively, approximately equal to 100%.

The data points for each frame were randomly assigned into equal training and test sets, for a 50%–50% split between training and testing datasets for each frame. As a general rule of thumb, a train-test split for evaluating machine learning algorithms is 80%–20% or 70%–30%, which has been utilized in previous studies [23–32]. However, due to a small sample size of the minority class used in this study, there could be cases of no observations for the minority in a test set when a large training set is employed with conventional train-test split. Therefore, this study increased the testing set size to 50% of the dataset to observe both classes in the testing set and therefore evaluate the model performance for both classes.

Imbalanced classification data leads to biased prediction toward the majority class. Several sampling techniques have been developed to address class imbalance problems such as undersampling and oversampling. Undersampling deletes examples from the majority class in the training set, but it can pass over important information during removal. Oversampling simply duplicates examples from the minority class and certain examples can be dense at a specific location in the sample space, thereby leading to overfitting due to the repetitively used samples. This study employed one of the improved oversampling methods, Synthetic Minority Over-sampling Technique (SMOTE) proposed by Chawla et al. [70], which is the most popular and perhaps most successful oversampling technique [71,72] that creates new synthetic data from the minority class rather than simply duplicating the data. The minority class is oversampled to have the same number of samples as the majority class. For example, Frame 2 had 7111 times greater number of the majority class than the minority class. The new minority class examples are generated 7111 times in a training set to equal the number of majority class examples. The oversampled minority class are not duplicates of the existing samples, but are derived using k-nearest neighbors and interpolation parameters. Many studies [73–76] have proven that the SMOTE approach is simple and computationally efficient while providing superior performance.

5. Comparison of sensitivity analysis results

This section compares the sensitivity analysis results obtained by the feature importance approach and the reliability sensitivity analysis. For the reliability-based sensitivity study, 40,000 simulations for each uncertainty under consideration were conducted. The feature name consists of the structural member name following the property name. Residual stress and sway imperfection are shortened to ‘rs’ and ‘sway’, respectively. For example, E-B2 represents the elastic modulus of B2 and rs-C1 indicates the residual stress of C1. Sway imperfections at the column locations – left, center, and right – are labeled as sway-C1, sway-C2, and sway-C3, respectively.

Table 3 summarizes the reliability-based sensitivity analysis results including statistics of strength, probability of failure, and reliability index. Frame 1 has larger COVs than Frame 2, with a larger difference for random elastic modulus and sway imperfection, which indicates that Frame 1 is more sensitive to these factors. Although the nominal ultimate strength was equal to 1.08 for both frames, Frame 1 has smaller values of β compared to those of Frame 2 due to the larger COVs of Frame 1 resulting in a lower boundary of the strength distributions.

Table 3
Reliability-based sensitivity results for Frames 1 and 2.

	Frame 1				Frame 2			
	Strength		Reliability		Strength		Reliability	
Random variable	Mean	COV	β	P_f	Mean	COV	β	P_f
Yield strength	1.13	0.034	3.41	3.3×10^{-4}	1.16	0.031	3.79	7.5×10^{-5}
Elastic modulus	1.07	0.007	9.01	≈ 0	1.07	0.004	16.8	≈ 0
Sway imperfection	1.01	0.030	2.65	4.0×10^{-3}	1.08	0.011	3.51	2.3×10^{-4}
Residual stress	1.07	0.003	27.7	≈ 0	1.07	0.002	37.2	≈ 0

5.1. Frame 1: instability of a single column

The results of the feature importance method are shown in Fig. 4. The top row (Fig. 4a–c) shows the top ten feature rankings of Frame 1 derived from the data analysis methods including ANOVA, mRMR, and Spearman's rank. The feature orders obtained from the model analysis techniques including impurity-based, permutation, and SHAP are shown in the bottom row (Fig. 4d–f). As previously discussed in Section 2, the feature importance techniques can derive either positive or negative values or both. As the feature rankings show only ten highly-ranked features, the negative scores are not included in the figure except for Spearman's rank (Fig. 4c), which rated the features based on their feature importance value magnitude. Sway-C2 and F_y-C2 are top-ranked from all the feature importance methods. Sway-C3 or E-C3 is third-ranked but has a negligible importance score in comparison to the top two features. Although the order of the remainder of the features is different between the various techniques, only the two highly-ranked features have significant scores. In other words, only the first two features are significant to the prediction of failure for Frame 1. Most methods result in scores approximately equal to zero for the least important features. Frame 1 fails by the inelastic instability of C2, and this is reflected in the importance score results as the features related to C2 are the most highly ranked.

From the results of Table 3, random sway imperfection resulted in the lowest β in Frame 1, followed by yield strength, elastic modulus, and residual stress. A small elastic modulus and large sway imperfection increase lateral deflections, thereby increasing second-order bending moments. As Frame 1 fails by the instability of C2, the frame capacity is most influenced by the factors resulting in increased bending moments.

Fig. 5 illustrates the scatter plots of input random properties versus the frame strength based on the reliability-based sensitivity studies. As shown in Fig. 5a, the yield strength of C2 and the frame strength have a nearly perfect correlation, which indicates that the strength of Frame 1 is controlled by C2. The yield strength of the other members showed no correlation with frame strength. Fig. 5b and c show that the frame strength has a weak correlation with the elastic modulus of C3 and the residual stress of C2. The sway imperfection at the center column (C2) has the most significant impact on the strength among the three column positions – left (C1), center, and right (C3) – by showing a strong positive correlation.

The highly-ranked features determined from the feature importance methods are identical with the factors that resulted in a lower β from the reliability-based sensitivity analysis. The feature rankings determined by the feature importance framework showed that sway-C2 and F_y-C2 are the most important features among the thirty-three random properties. The third-ranked feature is either sway-C3 or E-C3, which showed a positive correlation with the frame strength, but less significant than sway-C2 and F_y-C2. Overall, the random properties that have significant impacts on Frame 1's capacity determined by the reliability-based and machine learning-based sensitivity analyses are in agreement.

5.2. Frame 2: progressive yielding

Fig. 6 shows the top ten feature rankings of Frame 2 derived by the feature importance approach. As shown in Fig. 6a–c, the top-ranked feature is either F_y-C6 or sway-C2, and the remaining order varies for each data analysis technique, which identifies important features without model fitting. However, the model analysis techniques, which require model training to measure feature importance, derived the same top four features including sway-C2, F_y-C6, F_y-B2, and sway-C3 in descending order (Fig. 6d–f). The features ranked fourth through tenth are similar between the model analysis methods. At least four yield strengths are highly-ranked across all the methods, which indicates that yield strength is an influential factor in the failure of Frame 2 and the failure mode is progressive yielding. As previously shown in Fig. 2b, Frame 2 has six members that have critical impacts on the system failure, including four beams and two columns. In particular, B2 and C6 have two highly yielded zones each, and the yield strengths of these members are top-ranked among all the yield strengths. The feature importance results show the significant members in the system in addition to the influential properties. Due to the complex failure mode of Frame 2, the feature orders are not as straightforward as Frame 1, however the results indicate that the feature importance approach is accurate for steel frames with various failure modes.

The reliability-based sensitivity study investigated the effects of random properties on the frame strength. As shown in Fig. 7, the properties that have a significant effect are identical with the features that are highly ranked by the feature importance methods. Fig. 7a and b show dents on the upper left side, and they occur when the value of the B2 yield strength is the maximum or the minimum among all members, respectively. Fig. 7c and d indicate that Frame 2's strength has positive correlations with elastic moduli of C2 and B2. As X of C2 increases, the frame strength decreases (Fig. 7e) because the presence of residual stresses leads to the onset of yielding at a lower applied load [55]. Random elastic modulus and residual stress of C2 and B2 are correlated with the frame strength but showed small COVs, which represents less significant influence. The effects of random sway imperfection are shown in Fig. 7f–h. The center columns sway have the most significant impact on the frame strength than the sway of other columns. This example illustrates that not all factors influence the system behavior, and it is therefore unnecessary to assess the effects of each factor individually, as is done in a reliability-based sensitivity analysis. On the other hand, the feature importance approach analyzes all the factors at once to estimate the effects on system behavior.

Overall, Frame 2 has smaller magnitudes of the importance scores than for Frame 1. Moreover, Frame 1 has a large difference between the two top-ranked features and the remainder of the features, while the score difference between the features in Frame 2 is smaller. In other words, the importance score of Frame 2 decreases smoothly from the top to the bottom of the rankings. When a structural system fails by a single member (Frame 1), the properties of that member has a critical impact on the entire system. On the other hand, when various members lead to a system failure, such as progressive yielding (Frame 2), the properties of multiple members have a significant impact on the entire system. A comparison of the importance values between Frame 1 and Frame 2 indicates that the number of structural members involved in system failure influences the magnitude of importance as well as the number of features considered to be important.

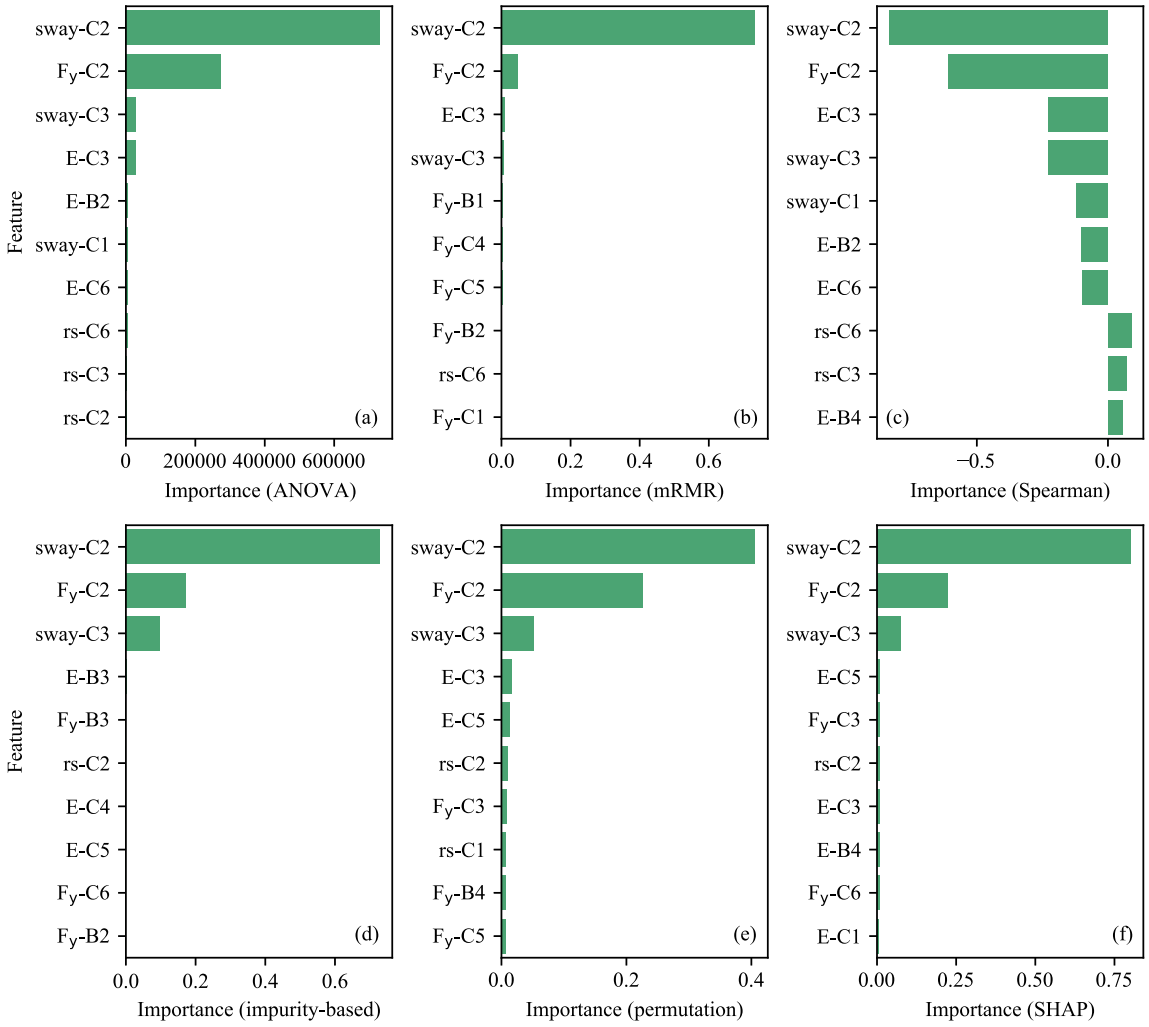

Fig. 4. Importance ranking of the top ten features of Frame 1 derived by data analysis methods (top row) and model analysis methods (bottom row).

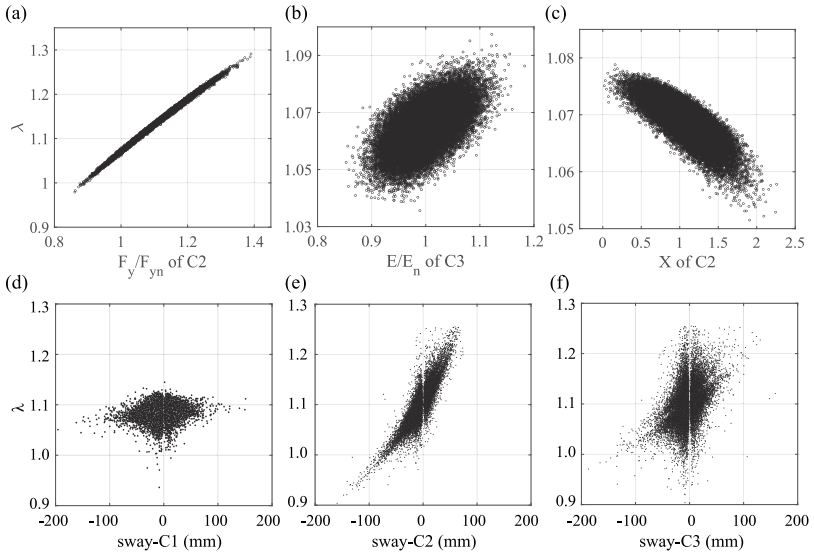

Fig. 5. Scatter plots of Frame 1 strength versus random (a) F_y of C2 (b) E of C3 (c) X of C2 (d) sway imperfection of C1 (e) C2 (f) C3.

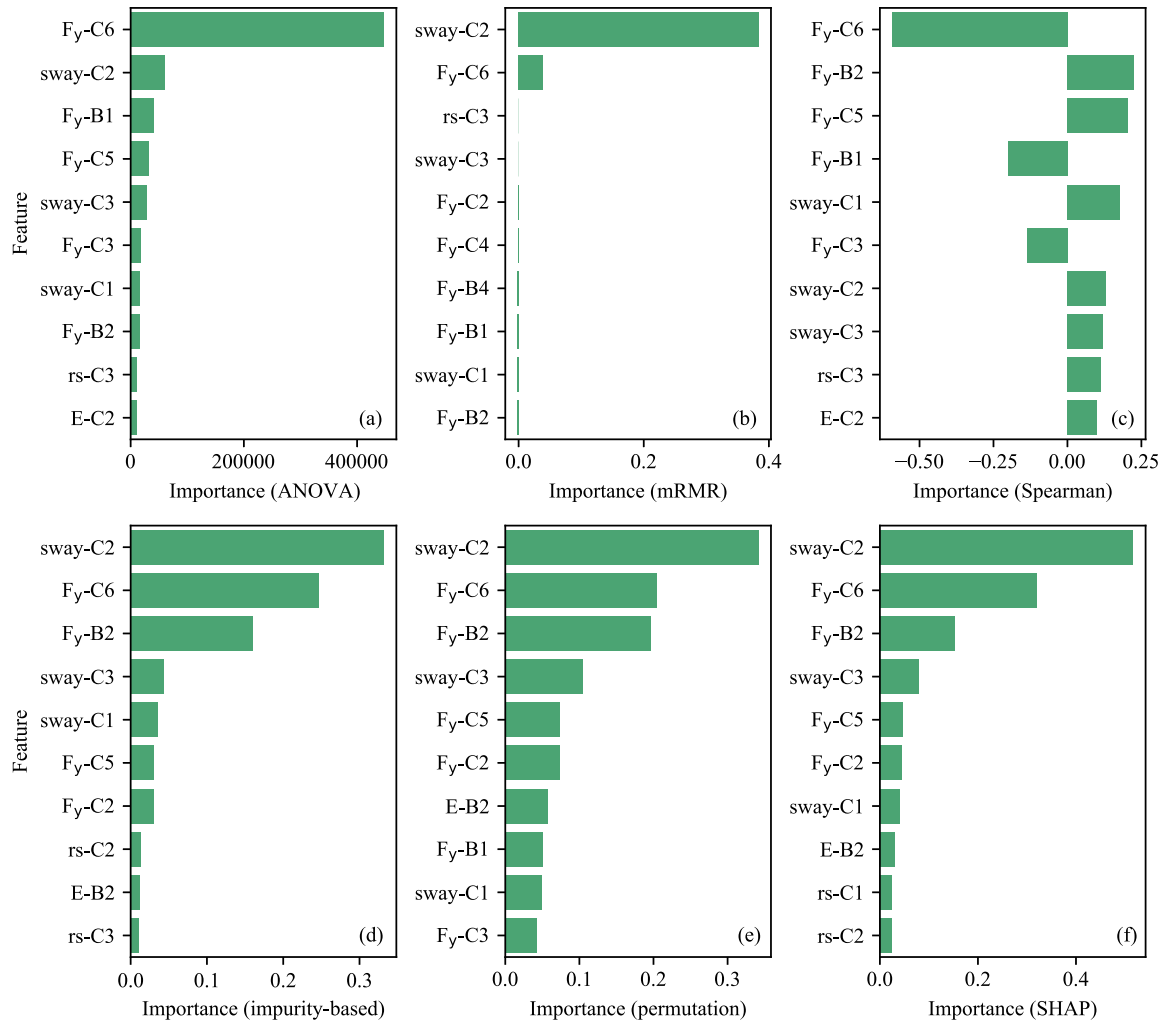

Fig. 6. Importance ranking of the top 10 features of Frame 2 derived by data analysis methods (top row) and model analysis methods (bottom row).

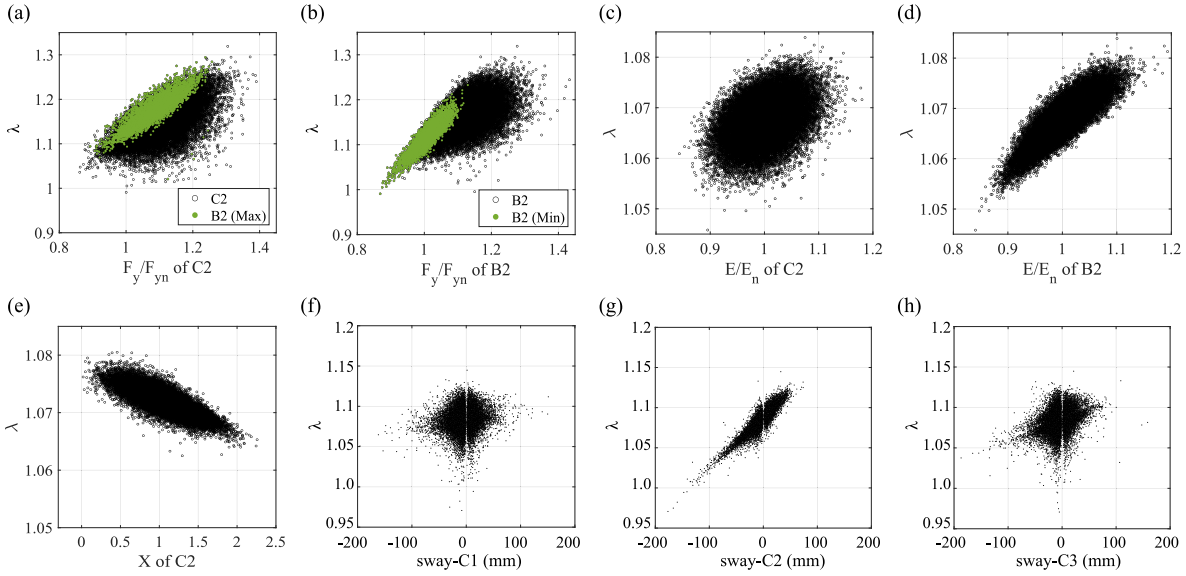

Fig. 7. Scatter plots of Frame 2 strength versus random (a) F_y of C2 (b) F_y of B2 (c) E of C2 (d) E of B2 (e) X of C2 (f) sway imperfection of C1 (g) C2 (h) C3.

6. Performance evaluation

The test set, which accounts for 50% of the dataset, is employed to evaluate the models fitted on the training set. The accuracy metrics include specificity and recall to measure the correct prediction of Class 0 (no failure) and Class 1 (failure), respectively. In addition, the Matthews correlation coefficient (MCC) is used, which is a suitable metric for the imbalanced dataset.

The predictive performance of the machine learning models for Frame 1 is shown in Fig. 8. The specificity curves for both logistic regression and decision tree algorithms (Fig. 8a and b) show that the specificity score reaches the nearly perfect value of approximately 1.0, even with only a few features. In this study, specificity represents the proportion of safe structures that are correctly predicted. The Frame 1 dataset is severely imbalanced with the no-information rate of 99.94%, therefore the model performance measured by specificity shows inflated results due to the biased classification towards the majority class. Recall is computed to evaluate how good a model is at detecting a structural failure, which is the positive class. As it is critical to identify system failure rather than safe structures in structural design practice, recall is a more crucial measure than specificity in this study. Fig. 8c shows the recall curve obtained from the logistic regression model. When the feature set contains the top three features of the model analysis techniques and ANOVA, which are sway-C2, F_y-C2, and sway-C3, the recall score rapidly increases up to 0.77. Spearman and mRMR ranked the sway imperfection of C3 at fourth and therefore the score abruptly rises when the feature set increases to four. The recall curve of the decision tree (Fig. 8d) shows the highest value when only two or three features are selected. The outcome recall scores converge to a lower score of 0.72 after reaching the peak point. This indicates that bottom-ranked features could be removed to reduce the computational effort without compromising model predictive performance to improve the computational efficiency Fig. 8e and f show the outcome MCC scores for the logistic regression and decision tree models, respectively. The MCC curves have a similar shape as the recall curves; the logistic regression model performance improves as the feature set increases, and the decision tree model reaches the peak point when the feature set is small. This indicates an overfitting issue which occurs when the model is trained on a large feature set. Feature selection based on the feature importance score can improve the overfitting by excluding the redundant features from training. The least important features, which are ranked after the fifteenth, could be removed to obtain a better performance.

The model performance of Frame 2 measured by specificity is shown in Fig. 9a and b. The specificity generates overoptimistic results due to the high imbalanced ratio of 99.99%. When the yield strength of C6 is ranked as the most important feature by ANOVA or Spearman, the decision tree model shows the nearly-perfect score even though the dataset includes only one feature (Fig. 9b). The lowest score of specificity is 0.92, indicating that both logistic regression and decision tree models can identify safe structures with high accuracy. The recall curves of Frame 2 are shown in Fig. 9c and d. The logistic regression model can correctly predict the failure only when the sway imperfection of C2 is included in the feature set. For example, the recall curve of Spearman's rank shows zeros until the feature set size is seven because the feature ranking rated the sway imperfection of C2 at seventh. The recall curve of the decision tree model (Fig. 9d) shows a large variation between the data analysis methods because they had completely different feature rankings. However, each curve merges to about 0.32 as the number of features increases. The MCC curve of the logistic regression model (Fig. 9e) shows a similar shape as the recall curve because the specificity scores had a single value, which is close to 1, regardless of the feature set size. The MCC values of the decision tree model merge to 0.15, which is the score of the entire feature set (Fig. 9f). When a high-dimensional dataset is used, the class imbalance leads to additional challenges in misclassification of the minority class [15]. As previously discussed in Section 4.3, Frame 2 consisted of a larger sample space and a fewer number of failures than for Frame 1. Moreover, the feature orders of Frame 2 were inconsistent between the feature importance techniques, as multiple features were significant to the prediction of system failure. The higher imbalanced ratio and the complex failure mode of Frame 2 result in a low performance measured by recall as well as the MCC. The extremely imbalanced classification of Frame 2 led to a lower performance for predicting structural failure because the machine learning classifiers had only a few minority class examples to oversample in the training set as well as to test the model prediction. The model performance, which measures the prediction of minority class, can be improved by obtaining more number of failures in a dataset or reducing the class imbalanced ratio.

The six feature importance techniques showed similar performance of Frame 1 measured by the MCC. The performance was improved after containing the three top-ranked features (Fig. 8e and f). In Frame 2, however, the model analysis methods showed more accurate results than the data analysis methods. In particular, the permutation and SHAP methods showed the best performance until the feature set size increases to seven (Fig. 9f) because they ranked F_y-C5 and F_y-C2 at fifth and sixth, respectively, whereas the impurity-based method ranked F_y-C2 at seventh, and F_y-C5 and F_y-C2 have a significant influence on the system failure of Frame 2. In summary, based on the feature rankings and the model performance results of both frames, SHAP and permutation methods are the best techniques for estimating the importance of features.

7. Discussion of future work

Future research is recommended to fully validate and expand the application of the methodology presented herein to other structural systems.

(i) Additional machine learning models should be evaluated. Logistic regression and a decision tree, which are one of representative regression-based and tree-based classifiers, were examined and they showed different performance curves as different metrics were employed. Benchmark studies on the feature importance approach with multiple machine learning methods might be a potential way to generalize the presented sensitivity analysis approach.

(ii) Machine learning models need to achieve a better prediction for the minority class. This is highlighted for a frame with a complex failure mode, which was progressive yielding for Frame 2 in this study. The frame had both a larger imbalanced ratio and dimension space than for Frame 1 with a simple failure mode, instability of a single column. Future research may include training a deep learning model to achieve high accuracy for high-dimensional data. In addition, dimension reduction techniques such as generalized sliced inverse regression using active learning [77] or feature selection techniques using deep learning [78] can be utilized.

(iii) Studies on the correlations between the imbalanced ratio, data space, and the degree of complexity in failure modes would help enhance the presented approach. For a frame with a complicated failure mode, which had a high imbalanced ratio, the number of observations was increased to obtain more samples of the minority class in a dataset, therefore increasing the data complexity and computational cost. Model development using data for structures with various failure modes, which would have different imbalanced ratios and data space, would provide suggestions for future implementation of machine learning-based structural analysis.

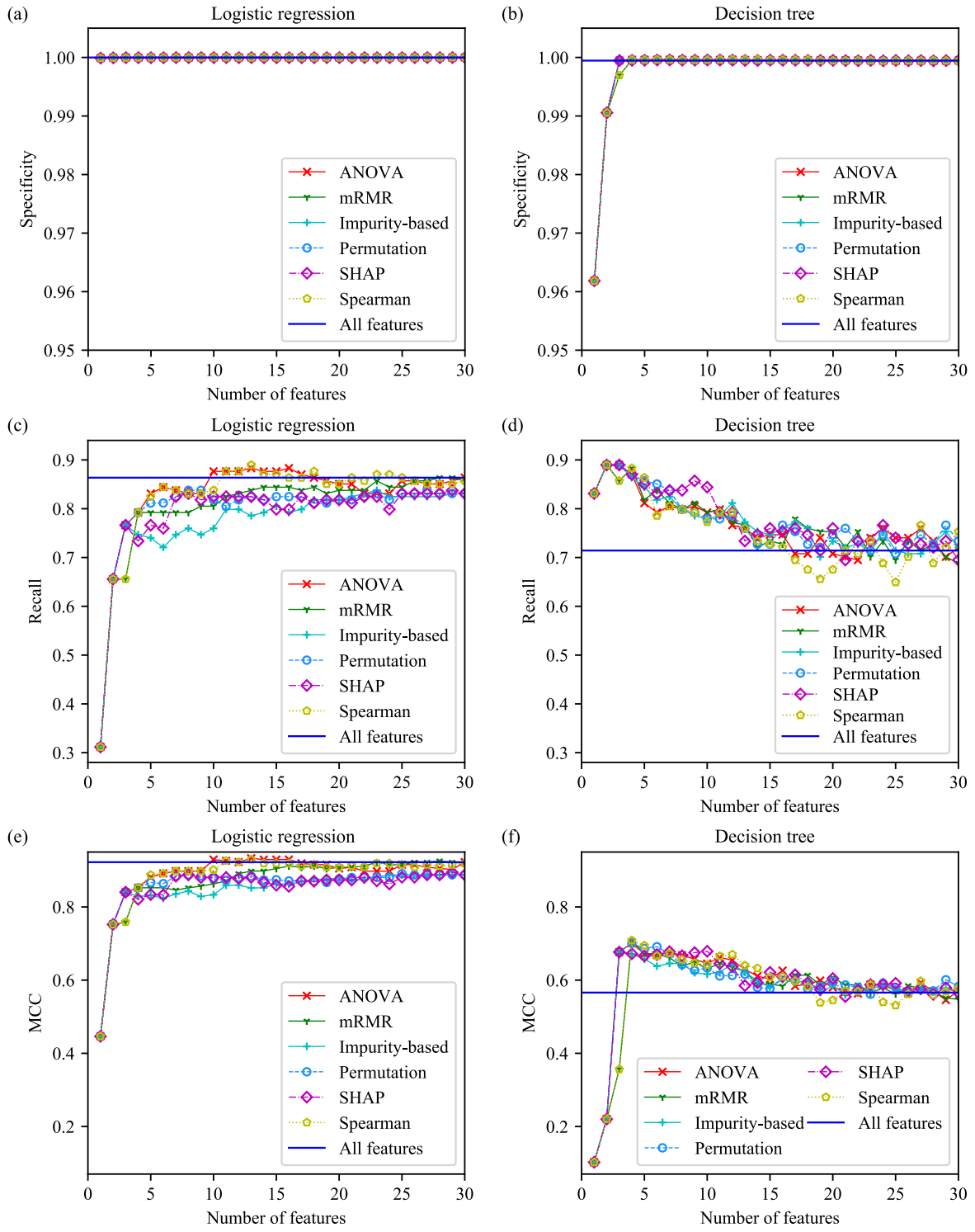

Fig. 8. Frame 1 specificity, recall, and MCC for logistic regression (left column) and decision tree (right column).

8. Conclusions

This study examined the feature importance approach using datasets with a large number of uncertainties and severely imbalanced classification. Two designs of a non-symmetric planar steel frame were investigated with uncertainties in material yield strength, Young's modulus, sway imperfection, and residual stress. The dataset information consisted of thirty-three uncorrelated uncertainties and the ultimate load ratios obtained from the finite element analyses. A scarce number of failures occurred, as is common in structural engineering design, thus the datasets were extremely class-imbalanced with the two classes being safe and fail. To observe the minority class in a test set split from the severely imbalanced data, a 50%–50% split for training and test sets were employed instead of the conventional train-test split ratio. Feature importance techniques including ANOVA, mRMR, Spearman's rank, impurity-based, permutation, and SHAP were trained on the high-dimensional and severely class-imbalanced datasets to identify the important features. The important features identified using the machine learning based feature importance approach were compared with the results of a conventional reliability-based sensitivity study

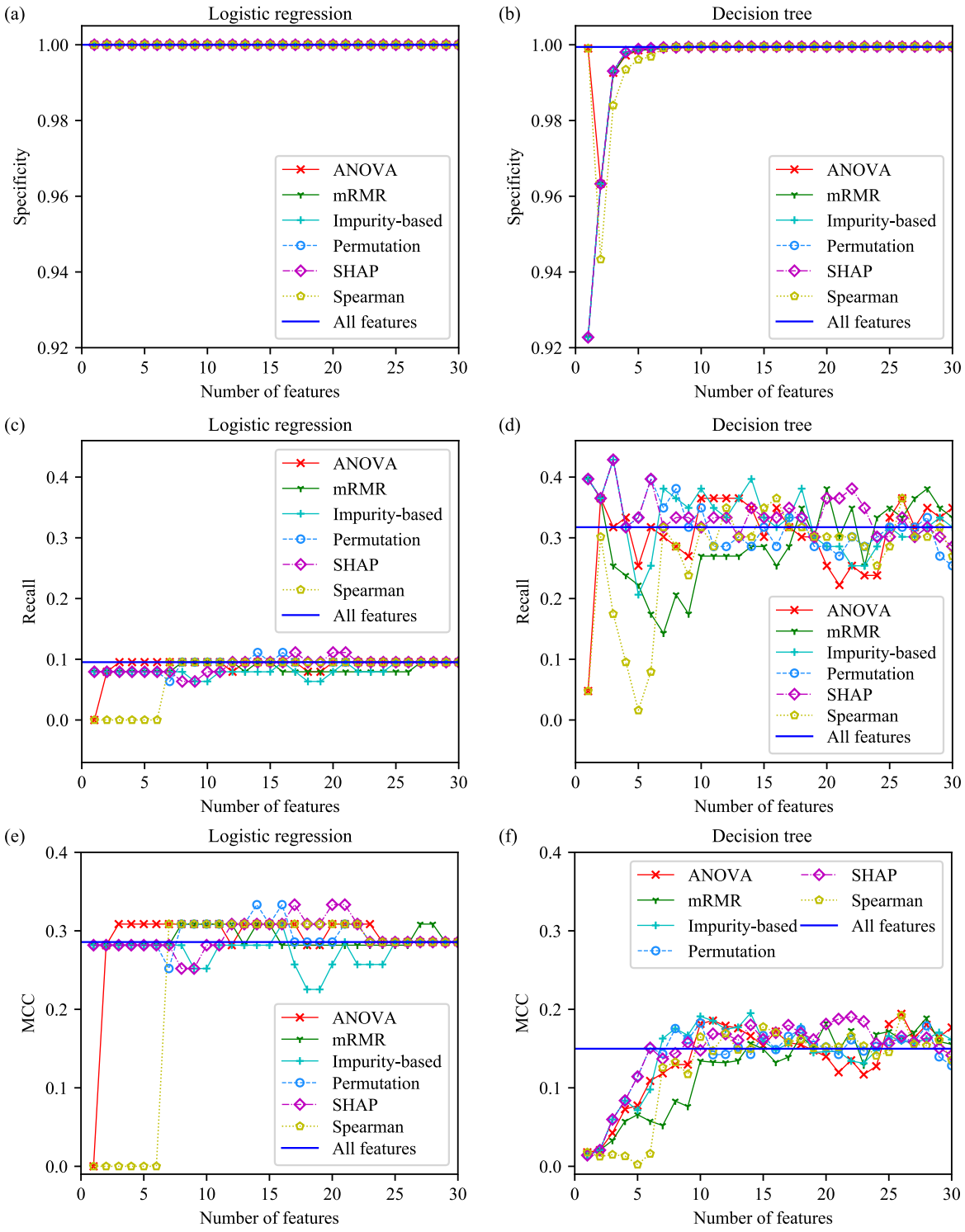

Fig. 9. Frame 2 specificity, recall, and MCC for logistic regression (left column) and decision tree (right column).

to identify factors which result in a lower system reliability index. The SHAP and permutation methods showed the best performance by ranking the same significant factors from the reliability-based sensitivity results at the top of the features. The feature importance method was not only shown to be straightforward in selecting the significant features by comparing their importance scores, but also in determining which structural members (e.g. specific columns and beams) have large impacts on structural failure without additional evaluation of performance. Overall, both methods identified the same factors which reflected the system failure modes, thus validating that machine learning techniques can be utilized in lieu of conventional reliability-based sensitivity studies.

After rating the features according to the importance score, the logistic regression and decision tree algorithms were trained to predict the classes using the feature set containing the top-ranked features. The overall performance showed that low-ranked features do not improve or even deteriorate the prediction accuracy, which indicates that they could be removed from the feature set to improve the computational efficiency. The model performance evaluated by specificity showed nearly-perfect performance for both frames because most examples

were assigned to the majority class, safe structure. As for the failure prediction, Frame 1, which failed by the global buckling of a single column, showed good performance even with the highly imbalanced classification. This study determined that the machine learning-based sensitivity analysis can identify the influential features affecting system failure even when there are high-dimensional uncertain parameters and a highly imbalanced dataset, for a relatively simple failure mode. However, for Frame 2 which had a complex failure mode of progressive yielding in addition to an extremely low failure probability, it was challenging to obtain the accurate prediction of the minority class. As class-imbalanced data is inevitable in structural engineering, it is necessary to be cautious in assessing the predictive accuracy of structures with a complex failure mode and a failure probability approximately equal to zero.

CRediT authorship contribution statement

Hyeyoung Koh: Conceptualization, Methodology, Validation, Formal analysis, Visualization, Investigation, Writing – original draft. **Hannah B. Blum:** Conceptualization, Resources, Supervision, Writing – review & editing.

Declaration of competing interest

The authors declare that they have no known competing financial interests or personal relationships that could have appeared to influence the work reported in this paper.

References

[1] Wu Y-T. Computational methods for efficient structural reliability and reliability sensitivity analysis. AIAA J 1994;32(8):1717–23. http://dx.doi.org/10.2514/3.12164.

[2] Rubinstein RY, Kroese DP. Simulation and the Monte Carlo Method. Vol. 10. John Wiley & Sons; 2016, http://dx.doi.org/10.1002/9781118631980.

[3] Torii AJ, Lopez RH, Miguel LFF. Probability of failure sensitivity analysis using polynomial expansion. Probabilistic Eng Mech 2017;48:76–84. http://dx.doi.org/10.1016/j.probengmech.2017.06.001.

[4] Proppe C. Local reliability based sensitivity analysis with the moving particles method. Reliab Eng Syst Saf 2021;207:107269. http://dx.doi.org/10.1016/j.ress.2020.107269.

[5] Bellman RE. Adaptive control processes: A guided tour. Princeton University Press; 1961, http://dx.doi.org/10.1515/9781400874668.

[6] Dunteman GH. Principal components analysis, no. 69. Sage; 1989.

[7] Hawchar L, El Soueidy C-P, Schoefs F. Principal component analysis and polynomial chaos expansion for time-variant reliability problems. Reliab Eng Syst Saf 2017;167:406–16. http://dx.doi.org/10.1016/j.ress.2017.06.024.

[8] Bommert A, Sun X, Bischl B, Rahnenführer J, Lang M. Benchmark for filter methods for feature selection in high-dimensional classification data. Comput Stat Data Anal 2020;143:106839.

[9] Saeys Y, Inza I, Larranaga P. A review of feature selection techniques in bioinformatics. Bioinform 2007;23(19):2507–17. http://dx.doi.org/10.1093/bioinformatics/btm344.

[10] Khalid S, Khalil T, Nasreen S. A survey of feature selection and feature extraction techniques in machine learning. In: 2014 science and information conference. IEEE; 2014, p. 372–8. http://dx.doi.org/10.1109/SAI.2014.6918213.

[11] Tadist K, Najah S, Nikolov NS, Mrabti F, Zahi A. Feature selection methods and genomic big data: A systematic review. J Big Data 2019;6(1):1–24. http://dx.doi.org/10.1186/s40537-019-0241-0.

[12] Hambali MA, Oladele TO, Adewole KS. Microarray cancer feature selection: Review, challenges and research directions. Int J Cogn Comput Eng 2020;1:78–97. http://dx.doi.org/10.1016/j.ijcce.2020.11.001.

[13] Branco P, Torgo L, Ribeiro RP. A survey of predictive modeling on imbalanced domains. ACM Comput Surv 2016;49(2):1–50. http://dx.doi.org/10.1145/2907070.

[14] Fernández A, García S, Galar M, Prati RC, Krawczyk B, Herrera F. Learning from imbalanced data sets. vol. 10, Springer; 2018.

[15] Blagus R, Lusa L. Class prediction for high-dimensional class-imbalanced data. BMC Bioinformatics 2010;11(1):1–17. http://dx.doi.org/10.1186/1471-2105-11-523.

[16] Chicco D, Jurman G. The advantages of the matthews correlation coefficient (MCC) over F1 score and accuracy in binary classification evaluation. BMC Genomics 2020;21(1):1–13. http://dx.doi.org/10.1186/s12864-019-6413-7.

[17] Ellingwood B. Probability-based codified design: Past accomplishments and future challenges. J Struct Saf 1994;13(3):159–76. http://dx.doi.org/10.1016/0167-4730(94)90024-8.

[18] ASCE, Reston, VA, Minimum design loads for buildings and other structures, 2016.

[19] Sheidaii MR, Bahraminejad R. Evaluation of compression member buckling and post-buckling behavior using artificial neural network. J Constr Steel Res 2012;70:71–7. http://dx.doi.org/10.1016/j.jcsr.2011.10.020.

[20] Pu Y, Mesbahi E. Application of artificial neural networks to evaluation of ultimate strength of steel panels. Eng Struct 2006;28(8):1190–6. http://dx.doi.org/10.1016/j.engstruct.2005.12.009.

[21] Chiew SP, Gupta A, Wu NW. Neural network-based estimation of stress concentration factors for steel multiplanar tubular XT-joints. J Constr Steel Res 2001;57(2):97–112. http://dx.doi.org/10.1016/S0143-974X(00)00016-X.

[22] Dabiri M, Ghafouri M, Raftar HRR, Björk T. Utilizing artificial neural networks for stress concentration factor calculation in butt welds. J Constr Steel Res 2017;138:488–98. http://dx.doi.org/10.1016/j.jcsr.2017.08.009.

[23] Degtyarev VV. Neural networks for predicting shear strength of CFS channels with slotted webs. J Constr Steel Res 2021;177:106443. http://dx.doi.org/10.1016/j.jcsr.2020.106443.

[24] Rahman J, Ahmed KS, Khan NI, Islam K, Mangalathu S. Data-driven shear strength prediction of steel fiber reinforced concrete beams using machine learning approach. Eng Struct 2021;233:111743. http://dx.doi.org/10.1016/j.engstruct.2020.111743.

[25] Feng D-C, Wang W-J, Mangalathu S, Hu G, Wu T. Implementing ensemble learning methods to predict the shear strength of RC deep beams with/without web reinforcements. Eng Struct 2021;235:111979. http://dx.doi.org/10.1016/j.engstruct.2021.111979.

[26] Almustafa MK, Nehdi ML. Machine learning model for predicting structural response of RC slabs exposed to blast loading. Eng Struct 2020;221:111109. http://dx.doi.org/10.1016/j.engstruct.2020.111109.

[27] Naser MZ, Kodur VK. Explainable machine learning using real, synthetic and augmented fire tests to predict fire resistance and spalling of RC columns. Eng Struct 2022;253:113824. http://dx.doi.org/10.1016/j.engstruct.2021.113824.

[28] Kiani J, Camp C, Pezeshk S. On the application of machine learning techniques to derive seismic fragility curves. Comput Struct 2019;218:108–22. http://dx.doi.org/10.1016/j.compstruc.2019.03.004.

[29] Nguyen HD, LaFave JM, Lee Y-J, Shin M. Rapid seismic damage-state assessment of steel moment frames using machine learning. Eng Struct 2022;252:113737. http://dx.doi.org/10.1016/j.engstruct.2021.113737.

[30] Hwang S-H, Mangalathu S, Shin J, Jeon J-S. Machine learning-based approaches for seismic demand and collapse of ductile reinforced concrete building frames. J Build Eng 2021;34:101905. http://dx.doi.org/10.1016/j.jobe.2020.101905.

[31] Mangalathu S, Jang H, Hwang S-H, Jeon J-S. Data-driven machine-learning-based seismic failure mode identification of reinforced concrete shear walls. Eng Struct 2020;208:110331. http://dx.doi.org/10.1016/j.engstruct.2020.110331.

[32] Huang H, Burton HV. Classification of in-plane failure modes for reinforced concrete frames with infills using machine learning. J Build Eng 2019;25:100767. http://dx.doi.org/10.1016/j.jobe.2019.100767.

[33] Koh H, Blum HB. Machine learning-based feature importance approach for sensitivity analysis of steel frames. EngrXiv 2021. http://dx.doi.org/10.31224/osf.io/mvkf3.

[34] Fernández-Delgado M, Cernadas E, Barro S, Amorim D. Do we need hundreds of classifiers to solve real world classification problems? J Mach Learn Res 2014;15(1):3133–81. http://dx.doi.org/10.5555/2627435.2697065.

[35] Orzechowski P, La Cava W, Moore JH. Where are we now? A large benchmark study of recent symbolic regression methods. In: Proceedings of the genetic and evolutionary computation conference. 2018, p. 1183–90. http://dx.doi.org/10.1145/3205455.3205539.

[36] Wolpert DH. The lack of a priori distinctions between learning algorithms. Neural Comput 1996;8(7):1341–90. http://dx.doi.org/10.1162/neco.1996.8.7.1341.

[37] Nowak AS, Collins KR. Reliability of structures. CRC Press; 2012.

[38] Parr T, Wilson JD, Hamrick J. Nonparametric feature impact and importance. 2020, arXiv preprint arXiv:2006.04750.

[39] Peng H, Long F, Ding C. Feature selection based on mutual information criteria of max-dependency, max-relevance, and min-redundancy. IEEE Trans Pattern Anal Mach Intell 2005;27(8):1226–38. http://dx.doi.org/10.1109/TPAMI.2005.159.

[40] Spearman C. The proof and measurement of association between two things. Am J Psychol 1904;15(1):72–101. http://dx.doi.org/10.2307/1422689.

[41] Breiman L. Random forests. Mach Learn 2001;45(1):5–32. http://dx.doi.org/10.1023/A:1010933404324.

[42] Lundberg S, Lee S-I. A unified approach to interpreting model predictions. 2017, arXiv preprint arXiv:1705.07874.

[43] Hosmer Jr DW, Lemeshow S, Sturdivant RX. Applied logistic regression. John Wiley & Sons; 2013.

[44] Matthews BW. Comparison of the predicted and observed secondary structure of T4 phage lysozyme. Biochim Biophys Acta, Protein Struct 1975;405(2):442–51. http://dx.doi.org/10.1016/0005-2795(75)90109-9.

[45] Izenman AJ. Modern multivariate statistical techniques: Regression, classification and manifold learning. New York City, NY: Springer; 2013.

[46] Fu F. Fire induced progressive collapse potential assessment of steel framed buildings using machine learning. J Constr Steel Res 2020;166:105918. http://dx.doi.org/10.1016/j.jcsr.2019.105918.
[47] Sun H, Burton HV, Huang H. Machine learning applications for building structural design and performance assessment: State-of-the-art review. J Build Eng 2021;33:101816. http://dx.doi.org/10.1016/j.jobe.2020.101816.
[48] Sokolova M, Japkowicz N, Szpakowicz S. Beyond accuracy, F-score and ROC: A family of discriminant measures for performance evaluation. In: Australasian joint conference on artificial intelligence. 2006, p. 1015–21. http://dx.doi.org/10.1007/11941439_114.
[49] E N1993-1-1. Eurocode 3: Design of steel structures - Part 1-1: General rules and rules for buildings. European Committee for Standardisation; 2005.
[50] ANSI/AISC, Chicago, IL, Specification for Structural Steel Buildings, 2016.
[51] AS 4100. Steel structures. Standards Australia; 1998.
[52] CSA S16:19. Design of steel structures. Canadian Standards Association; 2019.
[53] Melchers RE, Beck AT. Structural reliability analysis and prediction. 3rd ed.. Hoboken, NJ: John Wiley & Sons Ltd; 2018.
[54] Chambers JM. Graphical methods for data analysis. CRC Press; 1983, http://dx.doi.org/10.1201/9781351072304.
[55] Buonopane SG. Strength and reliability of steel frames with random properties. J Struct Eng 2008;134(2):337–44. http://dx.doi.org/10.1061/(ASCE)0733-9445(2008)134:2(337).
[56] Szyniszewski S. Effects of random imperfections on progressive collapse propagation. In: Structures congress 2010. 2010, p. 3572–7. http://dx.doi.org/10.1061/41130(369)322.
[57] Shayan S, Rasmussen KJR, Zhang H. On the modelling of initial geometric imperfections of steel frames in advanced analysis. J Constr Steel Res 2014;98:167–77. http://dx.doi.org/10.1016/j.jcsr.2014.02.016.
[58] Thai H-T, Uy B, Kang W-H, Hicks S. System reliability evaluation of steel frames with semi-rigid connections. J Constr Steel Res 2016;121:29–39. http://dx.doi.org/10.1016/j.jcsr.2016.01.009.
[59] Zhang H, Liu H, Ellingwood BR, Rasmussen KJ. System reliabilities of planar gravity steel frames designed by the inelastic method in AISC 360-10. J Struct Eng 2018;144(3):04018011. http://dx.doi.org/10.1061/(ASCE)ST.1943-541X.0001991.
[60] Cardoso FS, Zhang H, Rasmussen KJ, Yan S. Reliability calibrations for the design of cold-formed steel portal frames by advanced analysis. Eng Struct 2019;182:164–71. http://dx.doi.org/10.1016/j.engstruct.2018.12.054.
[61] Ziemian RD. Advanced methods of inelastic analysis in the limit states design of steel structures [Ph.D. thesis], Ithaca, NY: Cornell University; 1990.
[62] Buonopane SG, Schafer BW. Reliability of steel frames designed with advanced analysis. J Struct Eng 2006;132(2):267–76. http://dx.doi.org/10.1061/(ASCE)0733-9445(2006)132:2(267).
[63] Mazzoni S, McKenna F, Scott MH, Fenves GL, et al. OpenSees command language manual. Berkeley: University of California; 2006, URL http://opensees.berkeley.edu/manuals/usermanual.
[64] Galambos TV, Ketter RL. Columns under combined bending and thrust. J Eng Mech Div 1959;85(2):1–30. http://dx.doi.org/10.1061/JMCEA3.0000084.
[65] Ellingwood B, MacGregor JG, Galambos TV, Cornell CA. Probability based load criteria: Load factors and load combinations. J Struct Div 1982;108(5):978–97.
[66] Bartlett FM, Dexter RJ, Graeser MD, Jelinek JJ, Schmidt BJ, Galambos TV. Updating standard shape material properties database for design and reliability. Eng J AISC 2003;40(1):2–14.
[67] Lindner J, Gietzelt R. Imperfektionsannahmen für stützenschiefstellungen. Der Stahlbau 1984;52(4):97–101.
[68] Shayan S, Rasmussen KJR, Zhang H. Probabilistic modelling of residual stress in advanced analysis of steel structures. J Constr Steel Res 2014;101:407–14. http://dx.doi.org/10.1016/j.jcsr.2014.05.028.
[69] Melcher J, Kala Z, Holicky M, Fajkus M, Rozlivka L. Design characteristics of structural steels based on statistical analysis of metallurgical products. J Constr Steel Res 2004;60:795–808. http://dx.doi.org/10.1016/S0143-974X(03)00144-5.
[70] Chawla NV, Bowyer KW, Hall LO, Kegelmeyer WP. SMOTE: Synthetic minority over-sampling technique. J Artif Intell Res 2002;16:321–57. http://dx.doi.org/10.1613/jair.953.
[71] Hajibabaee P, Pourkamali-Anaraki F, Hariri-Ardebili MA. An empirical evaluation of the t-SNE algorithm for data visualization in structural engineering. In: 2021 20th IEEE international conference on machine learning and applications. 2021, p. 1674–80. http://dx.doi.org/10.1109/ICMLA52953.2021.00267.
[72] Brownlee J. Imbalanced classification with python: Better Metrics, Balance Skewed Classes, Cost-Sensitive Learning. Machine Learning Mastery; 2020.
[73] He H, Garcia EA. Learning from imbalanced data. IEEE Trans Knowl Data Eng 2009;21(9):1263–84. http://dx.doi.org/10.1109/TKDE.2008.239.
[74] Sun Y, Wong AKC, Kamel MS. Classification of imbalanced data: A review. Int J Pattern Recognit Artif Intell 2009;23(04):687–719. http://dx.doi.org/10.1142/S0218001409007326.
[75] Chawla NV, Japkowicz N, Kotcz A. Special issue on learning from imbalanced data sets. ACM SIGKDD Explor Newsl 2004;6(1):1–6. http://dx.doi.org/10.1145/1007730.1007733.
[76] Maldonado S, López J, Vairetti C. An alternative SMOTE oversampling strategy for high-dimensional datasets. Appl Soft Comput 2019;76:380–9. http://dx.doi.org/10.1016/j.asoc.2018.12.024.
[77] Yin J, Du X. Active learning with generalized sliced inverse regression for high-dimensional reliability analysis. Struct Saf 2022;94:102151. http://dx.doi.org/10.1016/j.strusafe.2021.102151.
[78] Li Y, Chen C-Y, Wasserman WW. Deep feature selection: Theory and application to identify enhancers and promoters. J Comput Biol 2016;23(5):322–36. http://dx.doi.org/10.1089/cmb.2015.0189.